LBNL-51843

# ERNEST ORLANDO LAWRENCE BERKELEY NATIONAL LABORATORY

# Two Dimensional Electron Solvation by Alcohol Molecules on the Ag(111) Surface

Simon H. Liu

**Chemical Sciences Division**

December 2002

Ph.D. Thesis

REFERENCE COPY
Does Not
Circulate

Library Annex Reference
Lawrence Berkeley National Laboratory

LBNL-51843
Copy 1

## DISCLAIMER

This document was prepared as an account of work sponsored by the United States Government. While this document is believed to contain correct information, neither the United States Government nor any agency thereof, nor the Regents of the University of California, nor any of their employees, makes any warranty, express or implied, or assumes any legal responsibility for the accuracy, completeness, or usefulness of any information, apparatus, product, or process disclosed, or represents that its use would not infringe privately owned rights. Reference herein to any specific commercial product, process, or service by its trade name, trademark, manufacturer, or otherwise, does not necessarily constitute or imply its endorsement, recommendation, or favoring by the United States Government or any agency thereof, or the Regents of the University of California. The views and opinions of authors expressed herein do not necessarily state or reflect those of the United States Government or any agency thereof or the Regents of the University of California.

LBNL-51843

# Two Dimensional Electron Solvation by Alcohol Molecules on the Ag(111) Surface

Simon Hsiang Liu
Ph.D. Thesis

Department of Chemistry
University of California, Berkeley

and

Chemical Sciences Division
Ernest Orlando Lawrence Berkeley National Laboratory
University of California
Berkeley, CA 94720

December 2002

This work was supported by the Director, Office of Science, Office of Basic Energy Sciences, Chemical Sciences Division, of the U.S. Department of Energy under Contract No. DE-AC03-76SF00098

# Two Dimensional Electron Solvation by Alcohol Molecules on the Ag(111) Surface

by

Simon Hsiang Liu

B.S. (University of California, Los Angeles) 1996

A dissertation submitted in partial satisfaction of the
requirements for the degree of
Doctor of Philosophy

in

Chemistry

in the

GRADUATE DIVISION
of the
UNIVERSITY of CALIFORNIA at BERKELEY

Committee in charge:

Professor Charles B. Harris, Chair
Professor Herbert L. Strauss
Professor Zi Q. Qiu

2002

# Two Dimensional Electron Solvation by Alcohol Molecules on the Ag(111) Surface

Copyright © 2002

by

Simon Hsiang Liu

The U.S. Department of Energy has the right to use this document
for any purpose whatsoever including the right to reproduce
all or any part thereof.

## Abstract

Two Dimensional Electron Solvation by Alcohol Molecules on the Ag(111) Surface

by

Simon Hsiang Liu

Doctor of Philosophy in Chemistry

University of California at Berkeley

Professor Charles B. Harris, Chair

Time and angle-resolved two photon photoemission spectroscopy is used to investigate the electron dynamics at the polar adsorbate/Ag(111) interfaces. Ultrafast photo injection of electrons into alcohol molecules/Ag(111) interfaces results in strong electrostatic interactions between the electron and surface adsorbates. A series of straight chain alcohol molecules is used for the experiment. Strong electron-dipole interactions manifested in electron-induced adsorbate reorganization solvate the electron by means of rotation of the dipole on the alcohol molecules. Rotation of the molecular dipoles cause dynamical relaxation of the observed photoelectron kinetic energy as a function of time delay between excitation and photoemission. Dynamics of electron localization by solvent motion have been investigated with angle-resolved two photon photoemission. The majority of the image state electrons are dynamically localized with the formation of the electron trap site by dipole rotation. Examination of early dynamics shows that some of the image state

electrons are localized by pre-existing defect sites in the layer.

A disk dipole model has been proposed to estimate the changes in the electrostatic potential caused by an image potential state electron induced molecular dipole rotation. Positive and negative ends of the dipoles are combined into two oppositely charged disks. Charge densities of these disks are related to the dipole moment and adsorbate density on the surface. The rotation of the dipoles to solvate the electron is represented by increasing separation distance between the disks. Potential energy difference at a few Ångstrom away from the surface for different dipole disk separations corresponds to the solvation energies measured with two photon photoemission.

To everyone who have helped me

# Contents

**List of Figures** vi

**List of Tables** viii

**1 Introduction** 1

**2 Background** 6
- 2.1 Image State Electron . . . 7
- 2.2 Multiple Reflection Theory and the Image Potential State Energy . . . 10
- 2.3 Image State Electron Lifetime . . . 13
- 2.4 Two Photon Photoemission . . . 17
- 2.5 Time Resolved Two Photon Photoemission . . . 21
- 2.6 Angle Resolved Two Photon Photoemission . . . 24
- 2.7 Prior Studies of Two Photon Photoemission . . . 27

**3 Experimental** 32
- 3.1 The Laser System . . . 32
- 3.2 Ultrahigh Vacuum System . . . 37
- 3.3 Alcohol Molecules Solvation Experiments . . . 42

**4 Electron at a Polar Adsorbate/Metal Interface** 47
- 4.1 Previous Solvation Experiments . . . 48
- 4.2 Work Function and Local Work Function . . . 55
- 4.3 Experimental Observation of Local Work Function . . . 62
- 4.4 Measurement of Work Function and Local Work Function with TPPE . . . 65
- 4.5 Two-Dimensional Electron Solvation by Alcohol Molecules . . . 66
  - 4.5.1 Static Work Function Change by Alcohol Molecule Adsorption . . . 68
  - 4.5.2 Dynamic TPPE Electron Kinetic Energies . . . 69
  - 4.5.3 Coverage Dependent Dynamics . . . 73
  - 4.5.4 Alcohol Molecule Dependent Kinetic Energies Dynamics . . . 75
  - 4.5.5 Deuterated Alcohol Molecules . . . 83
  - 4.5.6 Temperature Dependent Solvation Dynamics . . . 83

4.5.7 Discussion . . . . . 85
4.6 Dynamical Electron Localization . . . . . 94
4.7 Electron Solvation by Nitrile . . . . . 99
4.8 Disk Dipole Model . . . . . 101

**5 Conclusions** **111**

**Bibliography** **115**

# List of Figures


1.1 Schematic representation of two photon photoemission measurements of solvation dynamics . . . . . 4

2.1 Image charge and image state electron . . . . . 8
2.2 Image state electron potential and image state electron wavefunction . . . . 11
2.3 Image states electron density and oscillation . . . . . 15
2.4 Schematic description of two photon photoemission . . . . . 19
2.5 Description of photoemission process from different states . . . . . 22
2.6 Time resolved two photon photoemission . . . . . 23
2.7 Angle resolved two photon photoemission . . . . . 25
2.8 Spatially delocalize and localized electron as a function of photoemission angles 28

3.1 Experimental apparatus . . . . . 33
3.2 Autocorrelation of the laser pulse . . . . . 36
3.3 Sample manipulator . . . . . 38
3.4 Clean Ag(111) TPPE and Auger spectra . . . . . 40
3.5 Evaporation doser . . . . . 41
3.6 Methanol/Ag(111) coverage dependent TPPE spectrum . . . . . 43
3.7 Clean Ag(111) and different alcohol/Ag(111) LEED patterns . . . . . 46

4.1 Potential energy diagram of work function . . . . . 57
4.2 Electron density distribution at a metal surface . . . . . 58
4.3 Local surface potential . . . . . 61
4.4 Energy diagram of TPPE time of flight . . . . . 67
4.5 Two photon photoemission electron dynamics at a metal/butanol interface 71
4.6 Wavelength survey of alcohol molecules adsorbed on Ag(111) surface . . . . 72
4.7 TPPE electron kinetic energies dynamics for two different coverage of deuterated methanol on Ag(111) . . . . . 74
4.8 TPPE population dynamics for two different coverage of deuterated methanol on Ag(111) . . . . . 76
4.9 Electron solvation at monolayer of methanol adsorbed on Ag(111) . . . . . 78
4.10 Electron solvation at monolayer of propanol adsorbed on Ag(111) . . . . . 80

4.11 Electron solvation at monolayer of butanol adsorbed on Ag(111) . . . . . 81
4.12 Electron solvation at monolayer of pentanol adsorbed on Ag(111) . . . . . 82
4.13 Electron solvation at monolayer methanol and deuterated methanol adsorbed on Ag(111) . . . . . 84
4.14 Temperature dependent electron solvation dynamics for butanol adsorbed on Ag(111) . . . . . 86
4.15 $n = 1$ and $n = 2$ Image state temperature dependent solvation dynamics for butanol on Ag(111) . . . . . 87
4.16 Schematic description of local work function and local work function change due to dipole solvation . . . . . 90
4.17 Angle-resolved TPPE of monolayer butanol adsorbed on Ag(111) surface . . 96
4.18 Angle-resolved TPPE at $\Delta t = 0$ of monolayer propanol adsorbed on Ag(111) surface . . . . . 98
4.19 Electron solvation dynamics of monolayer acetonitrile adsorbed on Ag(111) 100
4.20 Electric potential due to a charged disk and an electron. . . . . 103
4.21 Model of alcohol molecular dipoles on a surface . . . . . 106
4.22 Disk dipole potential . . . . . 108

# List of Tables

3.1 Monolayer adsorption temperature and coverage exposure . . . . . 45

4.1 Work function change for alcohol molecules adsorption . . . . . 70
4.2 Alcohol molecules charge density . . . . . 93

## Acknowledgements

I wish to thank my advisor and colleagues for their guidance and assistance in the completion of my doctoral research. Professor Charles Harris provided an environment that fosters intellectual growth and independent pursue of scientific research. His invaluable advice has taught me to focus on the interesting and relevant scientific issues as well as the importance in conceptual understanding of the "big picture".

I am fortunate to work with a group of great colleagues. During the short period of time I spent with Robert Jordan, Robert Lingle, and Nien-Hui Ge, they had made a lasting impact on my research work. Steve Bromberg, Matt Asplund, and Matt Wilkens had provided me with basic understandings of the Liquid Side research. Chung and Haw are like big brothers to me. Chung taught me everything I need to know about the two-photon photoemission. André is not only a great coworker, he is also a supportive friend. Together we had great fun both in the lab and outside. Over-night experiments included coffee at Strada, snack runs to Safeway and Lucky, meal at Jack in the Box, and of course, lots of computer games, loud Simon and Garfunkel, and Pet Shop Boys music. When we were not working, we went skiing, camping, backpacking, and most often, just have dinner and lunch together. Kelly has provided many good ideas, especially regarding to fixing the laser. Paul and Sean have been invaluable to the discussion and continuation of the two-photon photoemission research. Dr. Ilya Bezel has shared many unique views on different aspects of the Harris Group research. I also want to thank the Liquid side, Ken, Preston, Christine, Libby, Jennifer, and Jason for many insightful talks and discussions. It was nice sharing an office with Paul, Christine, Libby, Sean, and Steve. We talked about many things beyond

the realm of academic research. And of course, the group would not function properly without Vijaya dealing with adminstration issues.

I would like to thank my family for their support throughout my education. My parents have encouraged me to follow my dream and to pursue a career goal of my own interest. My sister Julie has always been there to render a helping hand whenever I need it. In my wife Deling, I found a parter for life. I would like to thank her for her support, patience, and understanding. Most of all I would like to thank her for her unreserved love. Mike, Rob, and Emer have also been the most supportive friends anyone can ask.

This work was supported by the Director, Office of Energy Research, Office of Basic Energy Sciences, Chemical Sciences Division of the U.S. Department of Energy, under Contract No. DE-AC03-76SF00098. The authors acknowledge NSF support for specialized equipment used in the experiments described herein.

# Chapter 1

# Introduction

Electron dynamics at surfaces and interfaces are of central importance in many fields of studies. Many technological important processes depend strongly on the energy levels, transport properties, and lifetime of the electron at interface. For example, catalytic reactions on the surface often involve electron transfer between the reactant and the metal substrate [1]. Electron induced desorption results from the electronic coupling between the metal and adsorbate dissociative states [2]. The efficiency of any electronic device depends on the electron transport properties at the interface [3,4]. The dynamics of these processes are further complicated by the presence of an electron because electron can exert strong electrostatic forces on both the surface and adsorbates. Knowledge of the behavior of electrons at these interfaces is critical in order to improve device efficiency and understand chemical processes at interfaces.

Electron photoinjected into a metal/adsorbate interface can be used as a probe of the dynamics at the interface [5]. The energy and lifetime of the electron at the interface

reveal information about the electronic structure at the interface [6]. In addition, excitation of the electron and the analysis can be accomplished with laser pulses that have time scales comparable to the nuclear motions of adsorbates on the surface [7]. The ultrafast spectroscopy of the interface allows real time observation of changes in charge distribution associated with adsorbate motions. One particular system of interest is the excess electron at a metal/polar adsorbate interface with strong charge-dipole interactions. Strong electron-adsorbate interactions can cause an electron induced adsorbate reorganization, which is similar to electron solvation in liquids where electron-solvent interactions induce a solvent reorganization [8–10]. In general, solvation dynamics are known to significantly influence the rates of a wide variety of processes, including vibrational relaxation [11–13], ion transport [14], molecular isomerization [12, 15], protein folding [16], and electron transfer reactions [17–19]. The intrinsically asymmetric environment at an interface provides an area of particular significance, where both reduced dimensionality and hindered solvent motion result in dynamics distinct from those in the isotropic material [20–23].

Interfaces provide the asymmetrical environment that is experienced by the chemical species, whether they are in the form of a solid, or a molecular species as in a gas or liquid, or interface charges made up of electrons or ions. The solvation dynamics of species within an interfacial environment exhibit important aspects of adsorbate-solvent interactions, but the subject has been largely ignored [20]. The asymmetric interfacial environment has the properties that differ from the bulk media in terms of structures, compositions, and polarities. Likewise, the interfacial solvent dynamics can differ from the dynamics in either of the bulk media that defines the interface. Solvation describes the influence of the solvent

on the relative energy of the electronic states of solutes, which in turn affects the electronic absorption and emission spectra. The process of electron solvation is schematically illustrated in Figure 1.1. At the equilibrated ground state, the polar adsorbates are organized to minimize the solvent configuration energy. An ultrafast laser pulse then excites a substrate electron from below the Fermi level to the interface without disturbing the nuclear coordinates of the solvent, consistent with the Franck-Condon principle ($t_0$ in Figure 1.1). Responding to the excitation of the electron, the adsorbate molecules reorganize around the excited electron. This is equivalent to motion along the excited state potential ($t_1 > t_0$ in Figure 1.1) on the solvation coordinate. The time dependent shift in the electronic energy, $\Delta E$, during the solvation process can be observed using two photon photoemission (TPPE).

Two photon photoemission of image state electron provides some unique advantages to study electron solvation at interfaces. The image potential states that reside within a few Ångstroms of the surface can be populated by photo injection of electrons from the bulk. Owing to the proximity of the interfacial states to the interface, the image state electron can be used as a probe of the surface dynamics. With laser pulses on the order of $\sim$ 100 femtoseconds, TPPE is capable of monitoring the fast nuclear motions that take place on the surface. Angle-resolved TPPE is used to determine the extent of the electron wavefunction parallel to the surface. Image state electron wavefunction is strongly affected by the adsorbate motions on the surface.

This dissertation reports the direct observation of electron solvation at polar adsorbate/Ag(111) interfaces. In this case, the alcohol adsorbates rearrange in response to the presence of an electron. Time and angle-resolved two photon photoemission spectroscopy is

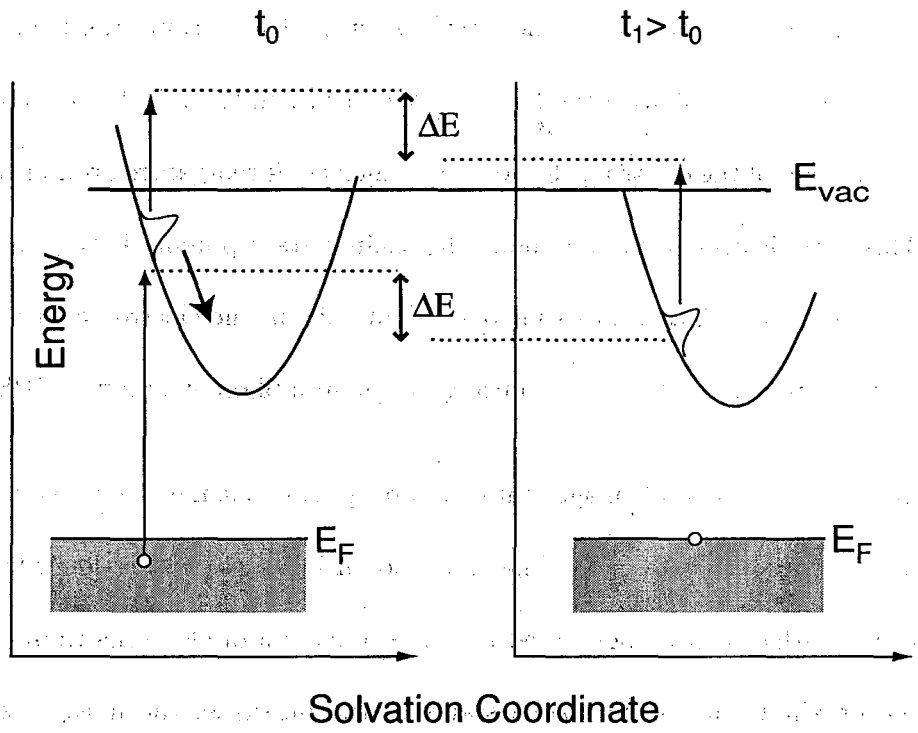


Figure 1.1: Schematic representation of two photon photoemission measurements of solvation dynamics. An ultrafast laser pulse excites a substrate electron from below the Fermi level ($E_f$) to the interface without perturbing the nuclear coordinates of the solvent ($t_0$). Responding to the presence of the electron, adsorbate molecules reorganize around the electron. The reorganization of the solvent lowers the solvent configuration energy by $\Delta E$, which is equivalent to motion along the excited state potential on the solvation coordinate ($t_1 > t_0$). The time dependent shift in the electronic energy during the solvation process can be observed using two photon photoemission

used to measure the change in the electronic energy while the electron is being solvated by the alcohol adsorbates. The relaxation of the image electrons involves the changes in the "local" work function due to the surface adsorbates dipole reorientation, which is similar to dipole rotation observed in electron solvation in liquid. The TPPE investigation of solvation dynamics and solvation energies have been conducted with a series of linear chain alcohol molecules.

# Chapter 2

# Background

The detailed mechanisms of electron dynamics at a surface or interface is of great fundamental importance as well as technological implications. Electron interaction with the surface and interface plays a critical role in the performance of solid state electronic devices since all solid state devices require coupling of electrons to and from external sources. In attempts to study electronic states at a metal surface or at a metal/adsorbate interface, another field has grown around the study of electronic states created by the presence of an electron outside a metal surface and its induced surface polarization which is also known as an image charge. While the image electron resides outside of the metal surface, the electronic structure of the surface greatly affects the energy, effective mass, and lifetime of the electron. In addition, these image state properties can be significantly altered with the adsorption of an adlayer. This result necessitates the inclusion of the electronic structure of the adsorbates to model the essential physics of image states at a metal/adsorbate interface.

Ever since the discovery of the photoelectric effect by Einstein, photoemission has

been an important tool to study the electronic structures of metals [24]. While enormous amount of information has been acquired with various photoemission techniques, lack of time resolution limits the study of electron dynamics. The effort to study electron dynamics at surface and interfaces relies on the ability to time resolve the ultrafast electronic processes at the surface, such as electron scattering, energy transfer or relaxation, and localization. The advent of femtosecond lasers allows direct measurements of electron dynamics at the surface. The technique of two photon photoemission (TPPE) possesses both the required time resolution and energy resolution to study the image potential state dynamics at a metal surface and metal/adsorbate interface.

## 2.1 Image State Electron

When an electron is placed close to a metal surface, the electron induces a charge redistribution in the metal. The electric field from the electron is perpendicular to the surface, at which the field vanishes. Charge polarization due to the electron results in the formation of a fictitious charge in the metal. The schematic diagram of electron and induced image charge is shown in Figure 2.1. An electron at distance $z$ away from the surface induces polarization of the metal. The polarization in the metal is equivalent to the formation of a fictitious image charge located at $z$ inside the metal. Due to the mirror symmetry of the system, the induced charge inside the metal is referred to as an image charge. The resulting image charge has a magnitude of $-\beta e$, where $e$ is the electron charge and $\beta$ is defined as

$$\beta = \frac{\epsilon - 1}{\epsilon + 1} \tag{2.1}$$

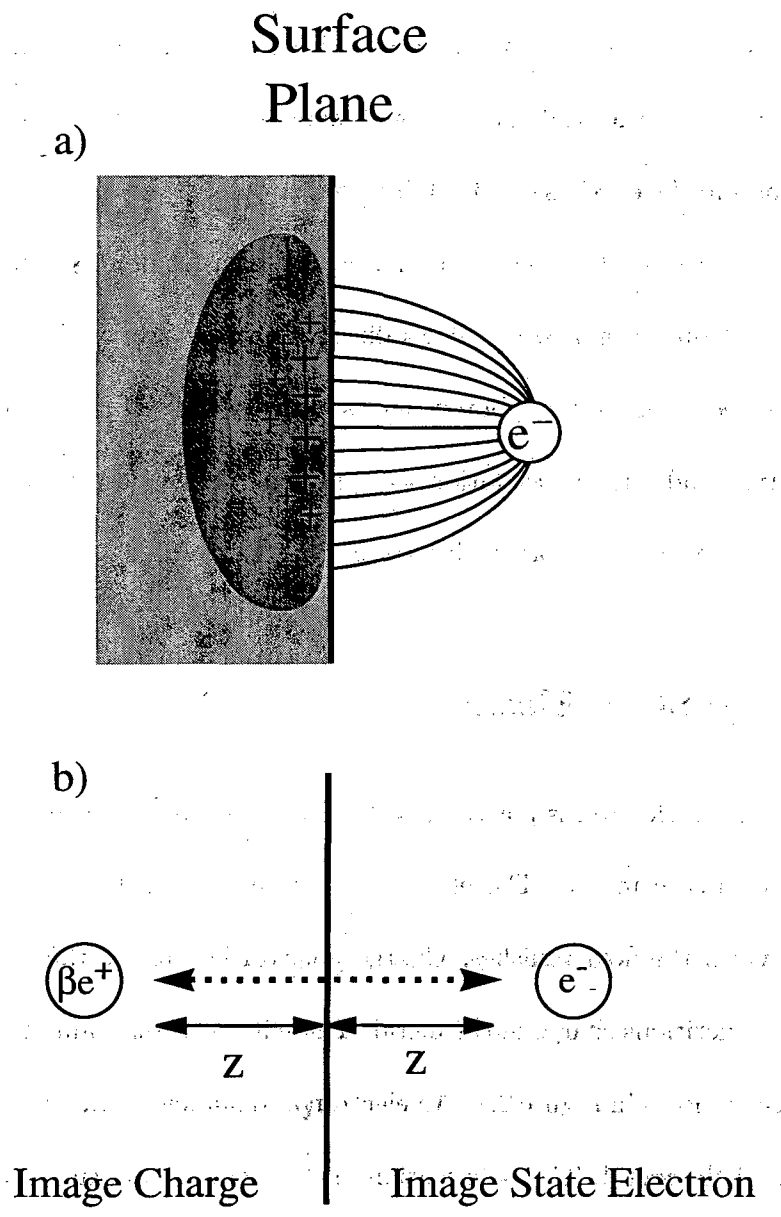


Figure 2.1: (a) Schematic diagram of surface polarization by an electron close to the surface. (b) Induced image charge resides at equal distance from the surface as compared to image state electron. The image charge has the magnitude of $\beta$e. The value of $\beta$ is determined by the dielectric constant of the metal.

The value of $\beta$ is determined by $\epsilon$, the bulk static dielectric constant of the metal. For a perfect conductor, $\epsilon$ is equal to $\infty$, making $\beta = 1$ [25]. Because the induced polarization has an opposite charge from the electron, the image charge is attracted to the electron outside the surface by the Columbic interaction. The image potential can be written as

$$V(z) = E_{vac} - \frac{q^2}{16\pi\epsilon_0 z} \tag{2.2}$$

where $E_{vac}$ is the vacuum energy, $q$ is the charge, and $\epsilon_0$ is the vacuum permittivity. The image potential gives rise to a series of Rydberg-like bound states, i.e. image potential states, which converge to the $E_{vac}$. For a perfect conductor, the image potential equals exactly $\frac{1}{4}$ of the potential experienced by the electron in a hydrogen atom. Half of this reduction in the potential arises because the distance between the electron and its image charge is $2z$ rather then $z$. Also, although the polarization in the surface is considered as a real charge, no electric field exists inside the metal. The electric field exists from 0 to $+\infty$ but not from $-\infty$ to $+\infty$, which accounts for the other half of the factor of 4. Wavefunction perpendicular to the surface can be obtained by using this image potential and solving for the one dimensional Schrodinger's equation perpendicular to the surface. The eigenvalues are

$$E_n = E_{vac} - \frac{m_e e^4}{(16)2n^2\hbar^2} = E_{vac} - \frac{0.85eV}{n^2} \tag{2.3}$$

where $m_e$ is the mass of an electron, $e$ is the elementary charge, and $n$ is the quantum number of the image states [5]. The factor of 4 in the potential leads to a reduction of the energy by a factor of 16, as compared to the hydrogen atom. Energy difference between

$E_{vac}$ and $E_n$ is called the binding energy, $E_b$. The quantum number $n$ assumes values of $1, 2, 3...\infty$. As the quantum number increases, the energy of the image state moves toward the vacuum energy and the image electron probability density moves away from the surface, as illustrated in Figure 2.2. The expectation values for the image state electron density are given by

$$< z >= 3.17n^2 \text{ Å} \tag{2.4}$$

where $n$ is the quantum number. For $n = 1$ and $n = 2$ image states, the expectation values of the electron density are 3.18 Å and 12.70 Å away from the surface, respectively. Image state electrons reside only a few Ångstroms outside of a metal surface, especially for the first few states, making them sensitive to changes in the surface electronic and physical structure. At close proximity to the surface, the image state electrons can also induce electronic or structural changes at the surface. The evolution of these properties can be probed by monitoring the image state electron energies and lifetimes.

## 2.2 Multiple Reflection Theory and the Image Potential State Energy

A more sophisticated treatment of the image state electron takes into account the electron interaction with the metal band structure. In multiple reflection theory, image states are represented as plane waves that oscillate between the inner turning point at the metal surface bandgap and the outer turning point at the image potential [26, 27]. The reflections of electron at both turning points add a phase shift in the plane wave. Stationary

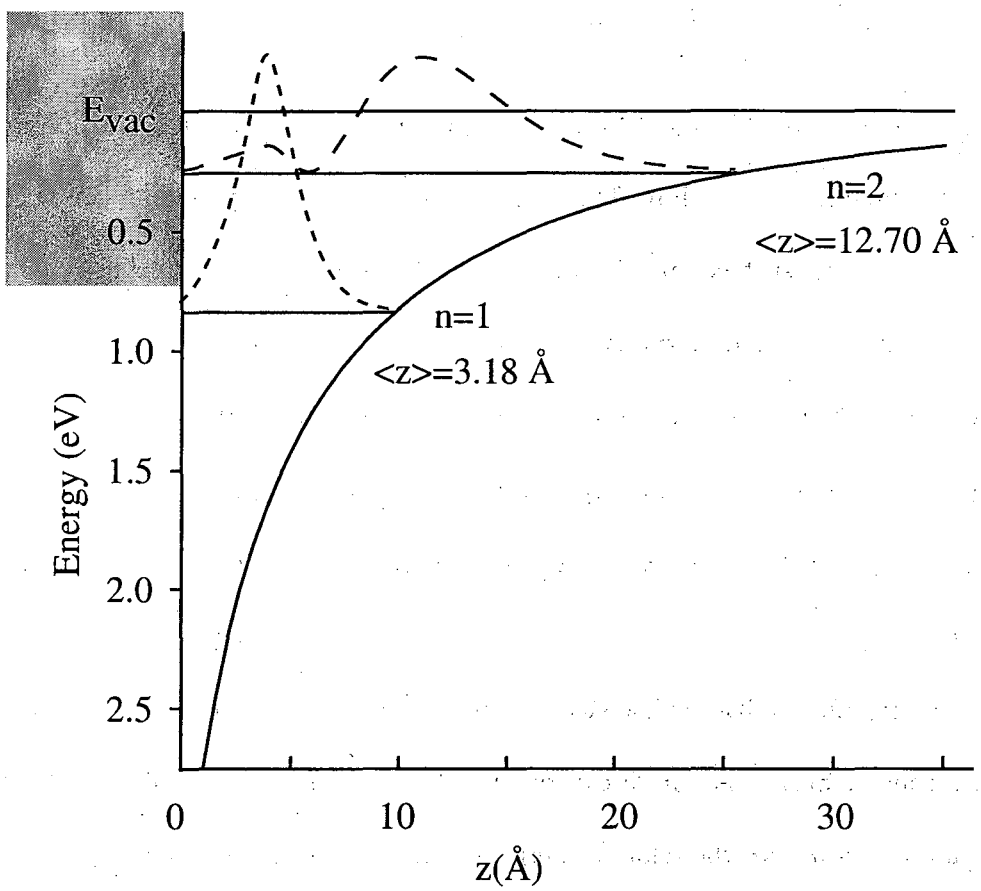


Figure 2.2: Electron induced image state potential leading to a Rydberg-like series of bound states termed image states. The electron probability density of the n=1 and the n=2 image states are plotted in the figure. As the quantum number increases, the energies of image states converge toward the vacuum level while the electron density moves away from the surface.

states exist when the sum of the phase shift equals a multiple of $2\pi$. The effects of the phase shifts lead to a modified expression for the energy of the image states

$$E_n = E_{vac} - \frac{0.85eV}{(n+a)^2} \tag{2.5}$$

This is analogous to Equation 2.3 except for the quantum defect $a$, which takes into account the effects of wave function phase shift [28]. The quantum defect $a$ depends on the phase of the wavefunction at the surface, and its value varies from 0 at the top of the bandgap to 0.5 at the bottom of the band. For a Ag(111) surface, the image potential states reside close to the conduction band edge, thus the quantum defect is close to 0.

Quantum defect can also be used to determine the work function of the metal [29]. Energy separation between two or more image state energies can be used to determine the quantum defect $a$. Consequently the vacuum energy relative to the image state can be determined with equation 2.5. With the knowledge of the Fermi energy from the photoemitted electron kinetic energy, work function $\Phi$ can be obtained from $\Phi = E_{vac} - E_{Fermi}$. Note that the quantum defect $a$ fixes the relative energy separation between the image potential states and the vacuum energy level. As will be shown later, a constant quantum defect $a$ was measured for electron solvation by polar molecule at the metal surface. The electron solvation by the polar molecules caused a dynamical relaxation of image state electron kinetic energies in TPPE. Relaxation of the photoelectron kinetic energy is attributed to the dynamical changes in the local vacuum level that reduces the work function of the image state electron with the binding energy of the electron and the quantum defect of the series remains constant.

## 2.3 Image State Electron Lifetime

The image state electron lifetime reflects the rate of electron-hole pair recombination in the metal. The electron lifetime is determined by two factors: the wavefunction overlap between the image state electron and the bulk metal, and the electronic structure of the surface [6, 30]. Energetic position of the image state relative to the surface band structure determines the wavefunction overlap between the metal and the electron which strongly influences the image state lifetime. The exponential decay of the electron probability density inside the metal occurs fastest at the middle of the bandgap, leading to a small wavefunction overlap and consequently the longest observed lifetime. As the energetic position of the image state moves toward the band edges, the decay of the electron probability density becomes slower and the image state lifetime increases. Image states that are degenerate with the conduction band of the metal have even greater penetration of the electron wavefunction into the metal and leads to a shorter lifetimes (see Figure 2.3(a)) [29, 31, 32]. For example, at the clean Ag(111) surface, the image state lifetime of $n = 1$ is 1.4 times greater than that of the $n = 2$ state. The $n = 1$ image state has a longer lifetime because it resides in the metal bandgap while the $n = 2$ state is degenerate with the conduction band. Alternatively, electron lifetime can be viewed as the classical oscillation period between the surface and the classical turning point in the potential. As shown in Figure 2.3(b), the distance between the surface and the classical turning point is determined by the shape of the image state potential. The oscillation period between the two turning point contributes to the lifetime of the image state electron. The round trip distance increases for higher image states, which results in increased lifetimes. Experimental and theoretical

works have indicated that the lifetime of the image state electron should be proportional to $(n+a)^3$ [33,34]. Measurements of image potential state lifetimes at Ag(111) surfaces show an $(n+a)^3$ dependence for $n = 2$ to $n = 5$ states, which are all degenerate with the silver conduction band. The $n = 1$ state does not follow this trend because it is not degenerate with the silver bandgap [35].

For electrons residing outside of an insulator layer on the dielectric interface, the image state electron can polarize both the insulating layer and the metal. In turn, the polarization in the insulating layer tends to screen the Columbic attraction between the electron and the metal surface. Band structures of both the metal surface and the insulating layer play important roles in determining the binding energy and the lifetime of the electron. Two models have been developed to describe such a system, the dielectric continuum model and the two band nearly free electron (NFE) model. The dielectric continuum model uses the static dielectric constant $\epsilon$ and electron affinity of the layer to account for the effects of polarization in the layer [36]. Potential inside the dielectric layer depends on the electron affinity, dielectric constant, and layer thickness. In the vacuum, the potential is represented by the image state potential outside dielectric layer as in Equation 2.5, and an infinite series of image charges due to successive induced image charges both in the dielectric layer and in the metal. This simple model has been used extensively to study dielectric layer with positive electron affinity and negative electron affinity. An overlayer with negative electron affinity results in repulsion of the electron probability density away from the layer towards the vacuum, effectively decoupling the electron from the metal. As observed in the n-alkane/Ag(111) experiment, presence a dielectric layer with a negative

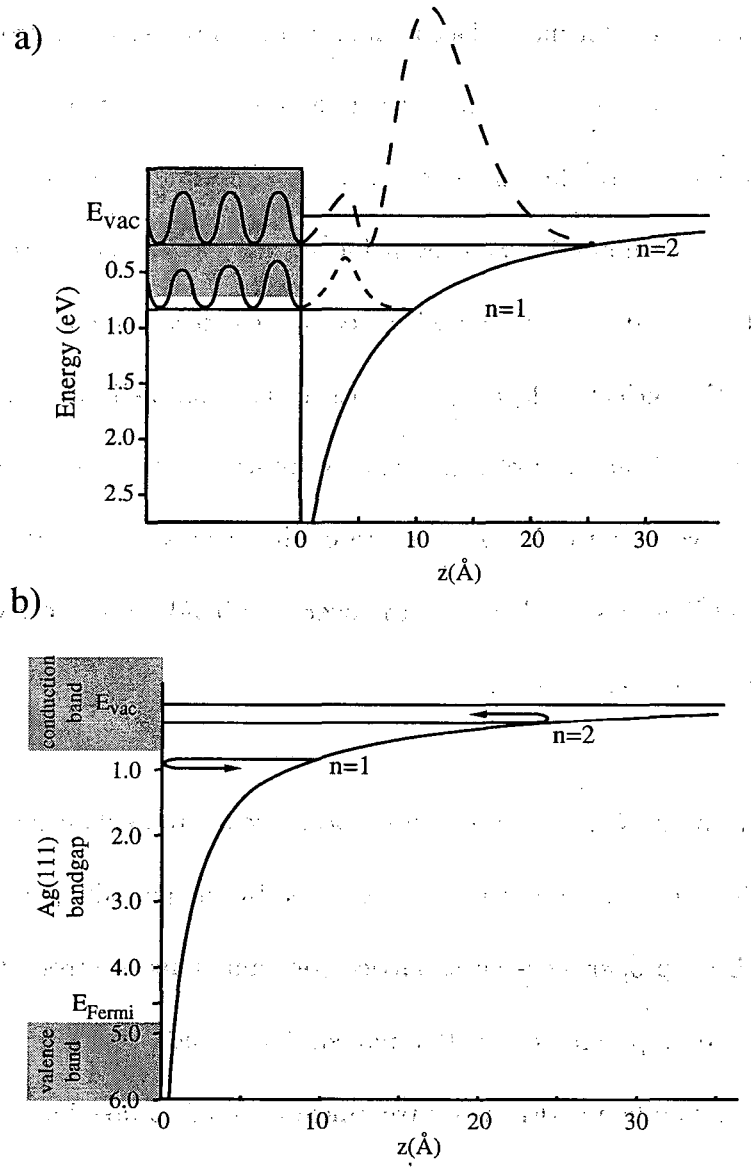


Figure 2.3: Schematic representation of image state electron wavefunction. (a) Image state that is degenerate with the bandgap has a smaller electron wavefunction overlap with the metal. This results in longer image state lifetimes for states that reside in the bandgap compared to the state that are degenerate with the metal conduction band. (b) The round trip distance between the surface and the classical turning point influences the lifetimes of image state electrons. As the quantum number increases, the round trip distance also increases, resulting in increased lifetime. Measurements of image state lifetime shows an $n^3$ dependence.

electron affinity served as a tunnelling barrier for image states. The $n = 1$ lifetime increases exponentially with layer thickness. Decoupling of the image electron from the metal also removes influences of the surface band structure on the image electron lifetime. Image state electrons showed an $(n + a)^3$ lifetime dependence as determined by the intrinsic oscillation time within the image potential well, even for states that are degenerate with the clean surface conduction band. For layers with positive electron affinity, the electron prefers to reside within the dielectric layer and forms a quantum well state as observed in the Xe/Ag(111) system. Since the electron mostly interacts with the adsorbate layer, it is reasonable to believe that the band structure of the layer also strongly affects the image state energies and lifetimes. Inclusion of the overlayer band structure gives rise to a more sophisticated two band NFE model.

The two band NFE model has often been evoked to explain the band structure of a crystal. In this model, the electrons are perturbed by the periodic potential of the lattice ion cores [37]. Bulk properties such as lattice constant, bulk electron effective mass, and band gap, are used as parameters in this model. For an adsorbate on Ag(111), two band NFE adsorbate on two band NFE metal treatments is used to take into account of electron interactions with both the metal and with the adsorbate layer. The electron wavefunction is obtained by solving the one dimensional time-independent Schrodinger equation for all three regions: inside the metal, in the adsorbate layer, and in the vacuum region. Several boundary conditions must be satisfied to obtain a valid solution; the electron wavefunction must vanish at infinity, and both the slope and the amplitude of the wavefunction must match at both the metal/adsorbate and the adsorbate/vacuum interface. The lifetime of the

image state can be estimated from the calculated electron probability density in the metal. The two band nearly free electron model has been applied in the study of Xe/Ag(111) and aromatic molecules/Ag(111) [29, 31, 38].

## 2.4 Two Photon Photoemission

The technique of photoemission has long been used to study the electronic states in solids and at solid surfaces [39]. A photon with energy larger than the work function $\Phi = E_{vac} - E_{Fermi}$ can photoemit electrons from the surface. By measuring the photoelectron kinetic energy, the work function of the metal, the energy of the initial state of the electron with respect to the vacuum energy, and the Fermi level can be determined with known photon energy used [24]. Single photon photoemission limits the initial state to be below the Fermi level and the final state above the vacuum level. The desire to study unoccupied states between the Fermi level and the vacuum level prompts the development of other photoemission techniques. Inverse photoemission was the first technique developed to study the unoccupied states [40]. In inverse photoemission, an electron with known kinetic energy and incident angle impinges on the metal surface and emits a photon. The photon energy equals the energy difference between the initial state and the final state, which in this case the final state is the image potential state. Image state energy can be determined if the work function of the surface is known. Image potential states at the Cu(111), Cu(110), Ag(111), Au(111), and Au(100) metal surface has been thoroughly studied with inverse photoemission by Straub and Himpsel [41,42]. The energy resolution of the inverse photoemission is limited by the incoming electron energy distribution, which is about several hundred meV. In TPPE,

the energy resolution is limited by the electron energy analyzer, which typically possesses the resolution of a few hundredth of an eV. Two photon photoemission has become the ideal technique to study image states, because it possesses both the capability of studying unoccupied intermediate states and a higher energy resolution.

In the TPPE, the first "pump" photon excites an electron from the initial state, from below the Fermi level to an intermediate state from which a second "probe" photon brings the electron to the final state above the vacuum energy. The measured kinetic energy of the photoemitted electron reveals information regarding the intermediate state and the initial state. The arrival of the probe pulse can be time delayed with respect to the pump pulse in order to measure the excited state lifetime. A schematic description of TPPE is illustrated in Figure 2.4. Two color TPPE employs photons with different energies for the excitation and the photoemission processes. Typically the visible light is frequency doubled to get the UV photon, which serves as the excitation pulse, $h\nu_1$. The subsequent electron photoemission uses the remnant visible light, $h\nu_2$. Photon energy less than the work function is used in TPPE to avoid single photon photoemission which will obscure the TPPE signal. This limitation also places constraints on electrons that can be accessed with TPPE. For example, states located at more than the work function energy below the Fermi level or at more than the work function above the vacuum level, can not be probed by TPPE.

The results of TPPE are represented by series of peaks with different energy distribution. Intensity of the peaks represents the number of electrons as a function of the kinetic energy. Photoemitted electron can origin from initial, intermediate, or final states. Fig-

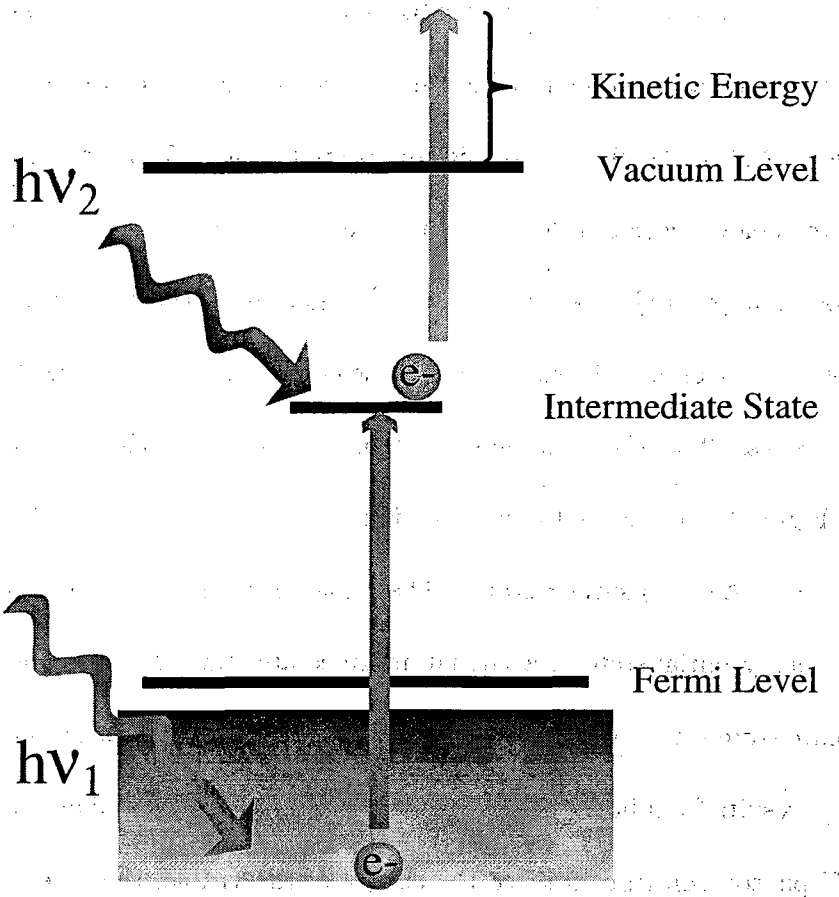


Figure 2.4: Schematic of two photon photoemission. The first photon excites an electron into the intermediate state. The probe photon $h\nu_2$ photo ejects the electron into the vacuum

ure 2.5 represents different photoemission schemes with TPPE. Due to their different photoemission steps, different states can be distinguished by varying the photon energy while observing changes in photoemitted electron kinetic energy. In our TPPE experiments, the UV pump pulse is generated by frequency doubling the visible probe pulse generated by the laser. The energy of the UV pulse is exactly twice the visible pulse, $h\nu_1=2h\nu_2$. Photoemission of electron from an initially unoccupied intermediate state (such as an image potential state) is represented in Figure 2.5(a). An electron is initially excited by an UV pulse from the continuum of bulk states below the Fermi level. As the excitation pulse increases in energy, the same state is being populated by electrons further below the Fermi level from the bulk. Increase in the photoelectron kinetic energy equals the changes in the wavelength used in the photoemission process. Therefore, the photoelectron kinetic energy changes by $h\Delta\nu_2$ of the photon used. Figure 2.5(b) shows the photoemission process from an initially occupied state (such as the clean Ag(111) surface state). The initial excitation pulse brings an electron from the fixed energy initial state to a virtual intermediate state. In this case, the energy of the intermediate state is not constant since it is a virtual state. Increase in the photoelectron kinetic energy results from both the changes in the pump pulse as well as the probe pulse. Since the UV photon contributes twice the energy of the visible, the kinetic energy varies as $3h\Delta\nu_2$ for TPPE from an initial state of constant energy. Single photon photoemission by the UV photon is shown in Figure 2.5(c). Since the visible photon only have half of the UV photon energy, the visible pulse does not play a role in single photon photoemission. The photoelectron kinetic energy form a single photon photoemission process varies with the energy used for photoemission, which is the UV pulse. Therefore the

final kinetic energy varies with $\Delta h\nu_1 = 2\Delta h\nu_2$. Final state photoelectron kinetic energy does not changes with the photon energy. For a clean Ag(111) surface, an occupied surface state was observed. Image potential states were considered as unoccupied intermediate states.

## 2.5 Time Resolved Two Photon Photoemission

The width of the peaks in TPPE has been used in determining the lifetime of the corresponding state, provided the peak only reflects a single state. The Lorentzian width of the TPPE peaks represents the lifetime broadening of the state. The measured linewidth $\Gamma$ is related to the lifetime $\tau$ by $\Gamma \cdot \tau = \hbar = 660$ meV $\cdot$ fs [5]. Although this method has been widely used to measure the lifetime of image state electrons, the measured lifetime is somewhat ambiguous because TPPE is a two steps process. The linewidth reflects the dephasing times for both the state transition and system inhomogeneity.

The lifetime of an intermediate state can also be measured by time resolved spectroscopy. Figure 2.6 shows the schematics of the time resolved TPPE. The probe pulse, $h\nu_2$, is time delayed with respect to the pump pulse, $h\nu_1$, which populates the intermediate states. The changes in the peak intensity as a function of time delay is a direct measure of the intermediate state lifetime. As mentioned in the previous section, the interfacial electron lifetime reflects the electronic structure of the interface. The time resolution of this technique is limited by the width of the laser pulse; the pulse width must be comparable or shorter than the lifetime. A different lifetime profile of image state signifies different mechanism in electron excitation and relaxation. It has been determined that the coherent effect contributes to the observed rise time in the time resolved TPPE [34, 43–45]. The intraband

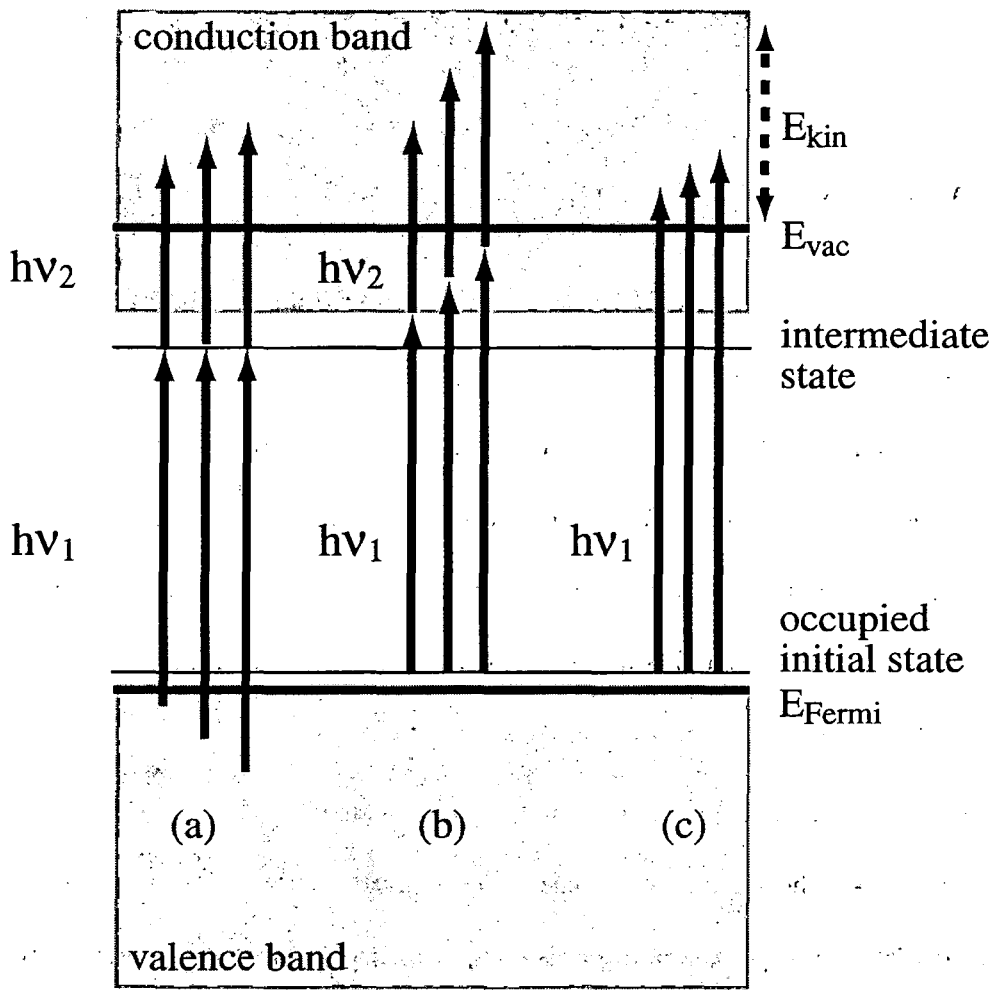


Figure 2.5: Schematic of two photon photoemission from different initial states and intermediate states, where $h\nu_1$ is the UV pump pulse, $h\nu_2$ is the visible probe pulse, and $h\nu_1$=$2h\nu_2$. $E_{kin}$ is the measured electron kinetic energy. In case (a), the intermediate state is excited from the valence band by $h\nu_1$ and photoemitted by $h\nu_2$. Varying wavelength results in $\triangle E_{kin} = \triangle h\nu_2$. In case (b), photoemission from the occupied initial state occurs through a two photon process. Varying wavelength results in $\triangle E_{kin} = 3\triangle h\nu_2$. In case (c), the occupied initial state is photoemitted by a single UV photon, $h\nu_1$, resulting in $\triangle E_{kin} = 2\triangle h\nu_2$

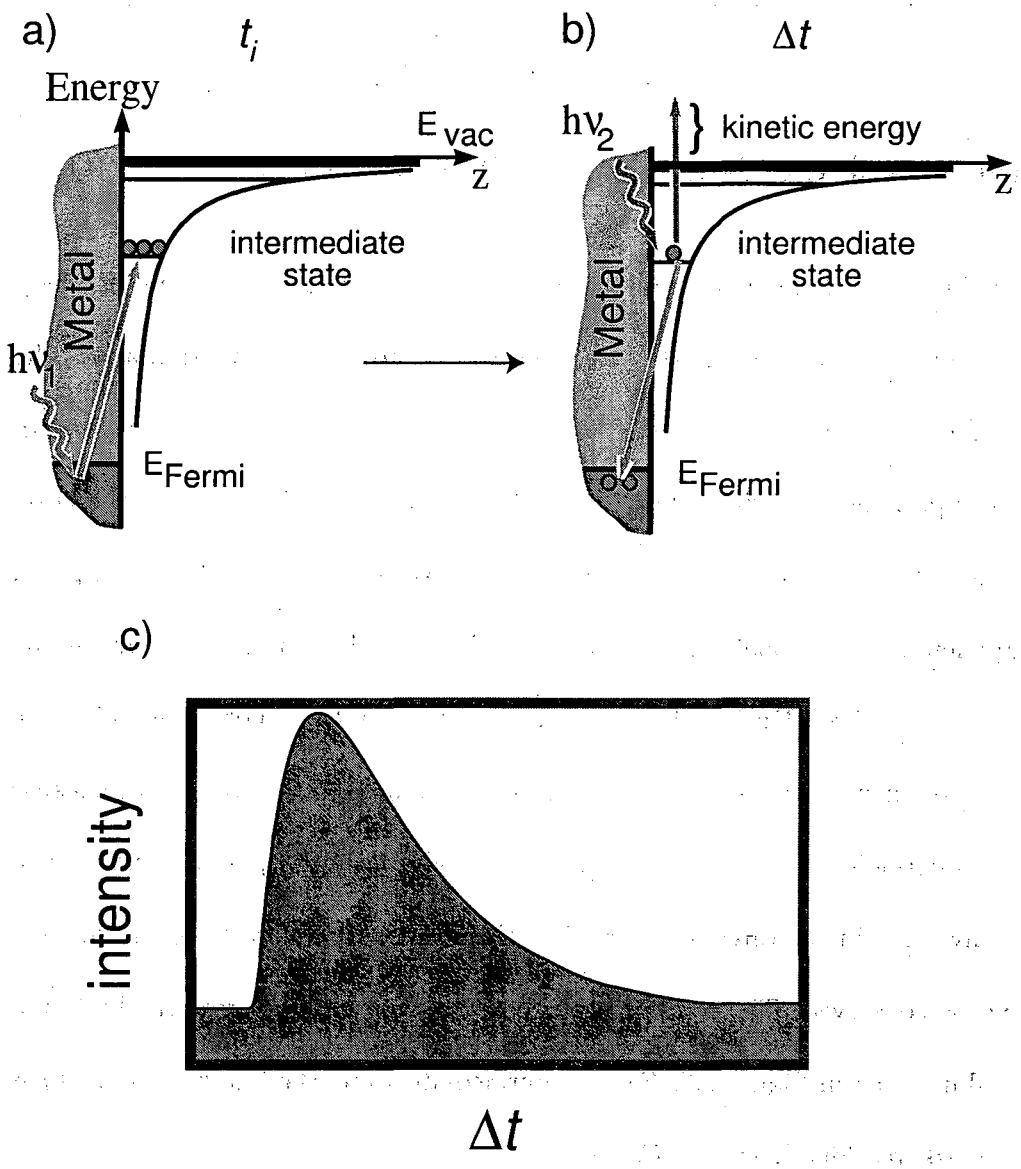


Figure 2.6: Schematic description of time resolved two photon photoemission. a) A pump pulse, $\hbar\nu_1$, excites an electron from below the Fermi level of the substrate into an unoccupied intermediate state at initial time $t_i$. b) A second pulse, $\hbar\nu_2$, photoemits the intermediate state electron into the vacuum at delay time $\Delta t$. The kinetic energy of the photoemitted electron is measured with a time of flight analysis. (c) Intensity of the TPPE signal as a function of $\Delta t$ reflects the excited state dynamics.

relaxation, where an electron at higher momentum states decays into lower momentum states via electron-electron scattering, was also observed at the Ag(111) surface [38].

## 2.6 Angle Resolved Two Photon Photoemission

The ability to perform angle resolved photoemission offers the opportunity to study the angle dependence of the photoemitted electron, which provides information about the three dimensional band structure of the metal or a metal/adsorbate interface. The electron wavefunction in a periodic potential is described by Bloch functions, where the wavefunction is determined by wavevector, $k$ [37]. At the surface the wavevector $k$ can be decomposed into two components, the perpendicular momentum, $k_\perp$, and the parallel momentum, $k_\parallel$, with respect to the surface. During the photoemission process $k_\perp$ is not conserved. The perpendicular component changes as the electron moves across the surface barrier because the potential is aperiodic in nature. However, the periodicity of the potential parallel to the surface is invariant in the direction normal to the surface, therefore $k_\parallel$ for an ordered periodic surface is conserved. The refraction of electrons photoemitted from the bulk into the vacuum is illustrated in Figure 2.7. For an intermediate state, the binding energy $E_b$ is related to the measured kinetic energy $E_{kin}$ by

$$E_b = \hbar\omega - E_{kin} \tag{2.6}$$

where $\hbar\omega$ is the energy of the photon used for photoemission. As seen in Figure 2.7, $k_\perp$ and $k_\parallel$ are given by

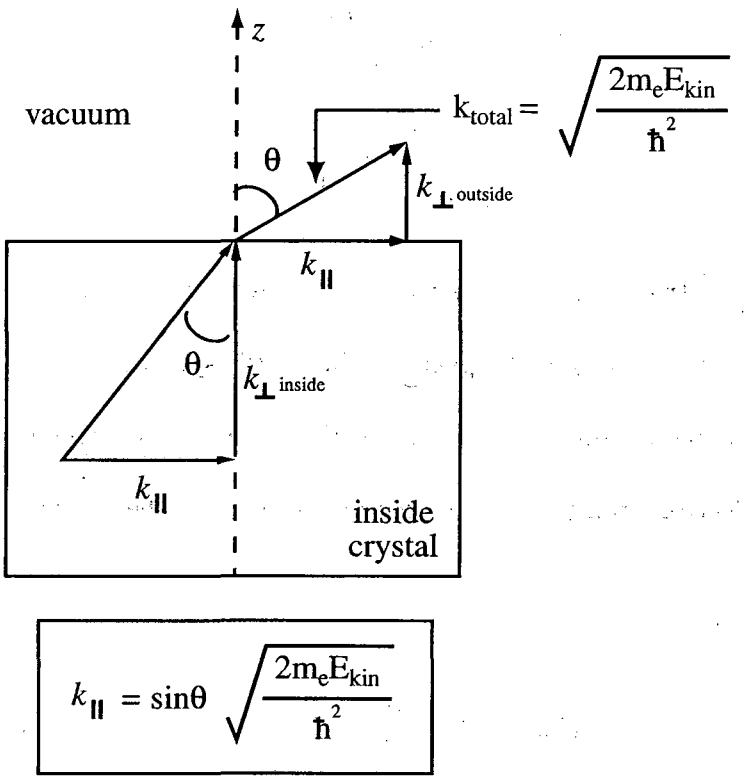


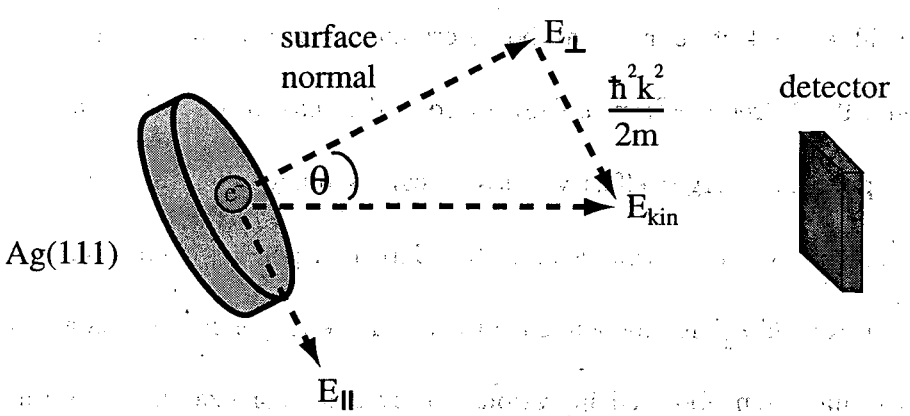


Figure 2.7: Schematic of angle resolved two photon photoemission. The parallel momentum, $k_{\parallel}$, is conserved in the photoemission process. By varying the angle between the surface normal and the detector, $k_{\parallel}$ can be determined.

$$k_{\parallel} = \sin\theta \sqrt{\frac{2m_e E_{kin}}{\hbar^2}}, \tag{2.7}$$

$$k_{\perp} = \cos\theta \sqrt{\frac{2m_e E_{kin}}{\hbar^2}}, \tag{2.8}$$

where $m_e$ is the free electron mass and $\theta$ is the angle between the surface normal and the detector. As the angle $\theta$ is changed, the peaks in the TPPE spectra changes according to the band dispersion along the direction parallel to the surface. The dispersion relation is determined by the electron transport properties in the metal. The dispersion relation is given by

$$E(k_{\parallel}) = V_0 - \frac{\hbar^2 k_{\parallel}^2}{2m^*} + E_0, \tag{2.9}$$

where $m^*$ is the effective mass of the electron, and $E_0$ is the perpendicular component of the electron energy. The value of $E_0$ can be measured from surface normal photoemission in which $k_{\parallel} = 0$. The value of effective mass can be determined by fitting measured $E(k_{\parallel})$ versus $k_{\parallel}$ to Equation 2.9. A free electron is delocalized and it has an effective mass of 1 with a parabolic dispersion. Larger effective mass means stronger coupling strength between the interface and the electron, thus leading to a larger dispersion curvature. For a spatially localized electron, $E(k_{\parallel})$ is independent of $k_{\parallel}$, and the dispersion plot is a flat line. Localized electron has been observed in various adsorbates. For example, electron dynamically localizes at the alkane/Ag(111) interface due to strong interactions between the electron and adsorbates, which results in the formation of polarons [46]. A disordered benzene layer localizes electron in defect sites [31]. Localized electrons were also observed

in self assembling monolayer islands [47]. In the current study, the dynamical electron localization is due to electron solvation by the adsorbate polar molecules.

## 2.7 Prior Studies of Two Photon Photoemission

Early TPPE experiments have been focused on studying the two and three dimensional band structures and electron dynamics at metal or semiconductor surfaces. Along with the advancements in femtosecond lasers, TPPE has also been employed in the following studies: electron dynamics in adsorbate overlayers, coherent excitation of electron wave packets [43], optical dephasing of electrons in metals [48], nuclear motion in photodesorption processes [7], two-dimensional band structure development in self-assembling monolayer [47, 49, 50], and spin-resolved electron relaxation in ferromagnetic systems [51].

The coherent excitation of several higher order image states (quantum $n > 4$) results in dynamics distinctly different from dynamics of a single quantum state. The quantum beats observed in the dynamics was attributed to the coherent interference between the wave functions of different image states. The energy separation of mixed quantum states was calculated from the beating period. Aeschlimann and coworkers used TPPE to measure the lifetimes of excited electron with different spins in ferromagnetic solids [51]. The majority spin-state electrons have lifetimes twice as long as that of minority-spin electrons. Petek and coworkers demonstrated the ability to control excited electron distribution in a metal through the optical phase of the excitation light [48]. The electronic dephasing dynamics were observed utilizing phase resolved pulses with time durations of $\sim 20$ fs.

The behavior of hot electron gases at or near surfaces has been a subject of intense

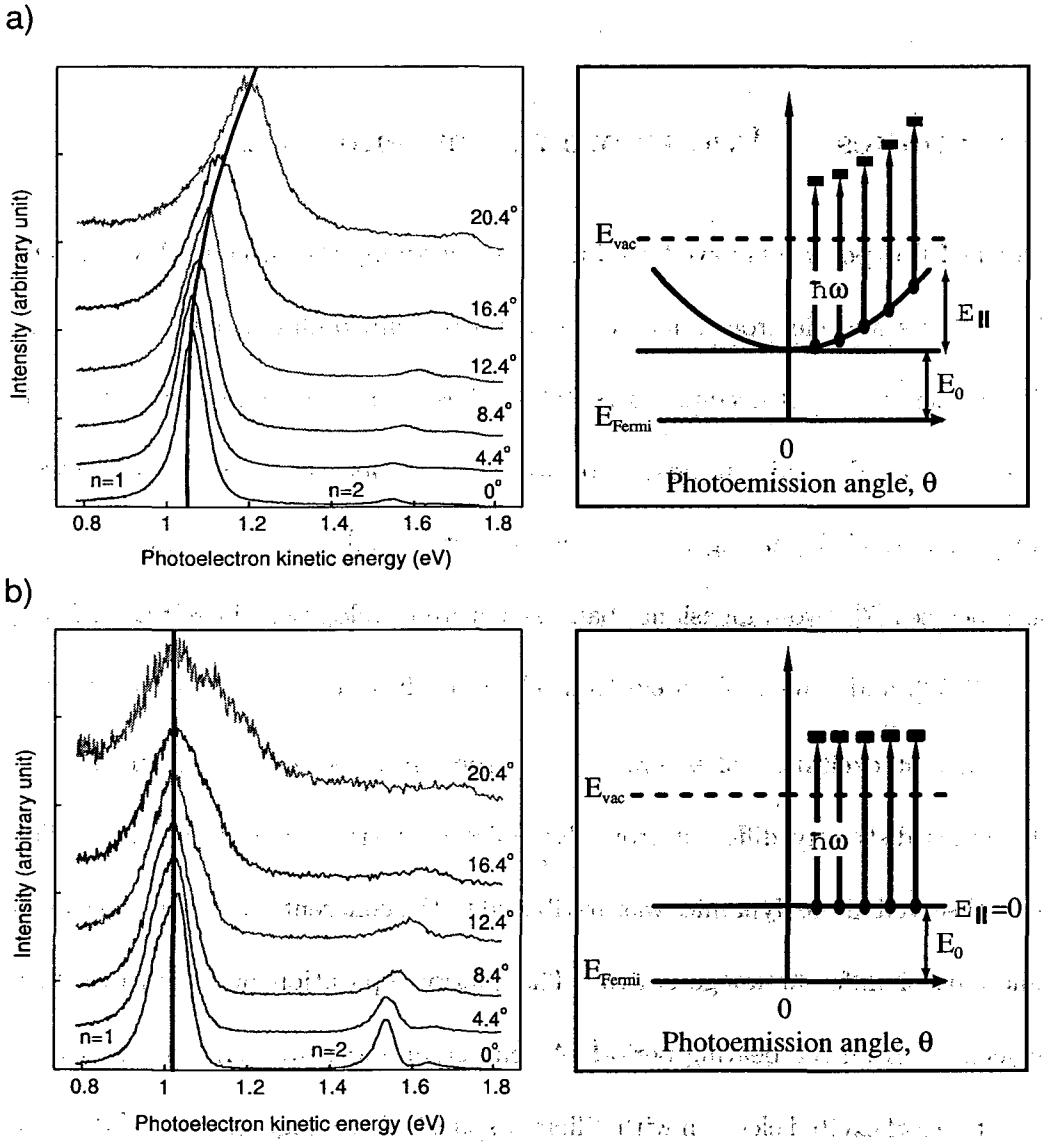


Figure 2.8: Angle resolved TPPE for monolayer butanol adsorbed on Ag(111) at different $\Delta t$ between laser pulses. a) A delocalized n=1 state was observed with angle resolved TPPE at $\Delta t$=0. For a spatially delocalize electron, photoemitted electron kinetic energy increases as the angles between the sample normal and the detector axis increases. b) At $\Delta t$=500 fs, a localized n=1 state was observed. For a localized electron, the kinetic energy is angle independent.

research. Ultrafast laser induced NO desorption from Pd(111) surface was attributed to the non-equilibrium hot electrons generated by the laser pulse. Hot electrons generate by an ultrafast laser pulse in the CO/O/Ru(0001) system were also found to be responsible for the oxidation of CO adsorbate and resulting in the formation of $CO_2$ molecules [52]. The $CO_2$ formation was caused by a hot electron transfer reaction from the substrate to adsorbates. On a longer time scale, hot electron relaxation in the metal is coupled to phonon excitations, which ultimately results in a phonon induced CO desorption. Petek and coworkers used TPPE to observe electron photodesorption of Cs atoms from a Cu(111) surface [7]. What they found is that the excitation pulse alters the electron distribution of the Cs atom promoting electron from the Cs-Cu bonding state to the antibonding state. The subsequent nuclear motion of Cs-Cu bond relaxation also changes the energy of the antibonding state. A complete picture of Cs atom nuclear motion was obtained by photoemitting the excited state electron in the antibonding state at different pump-probe time delays, i.e. at different Cs-Cu nuclear distance, and by measuring the electron energy changes associated with the Cs-Cu bond stretching. This represents the first femtosecond time resolved observation of nuclear motion of atoms on surfaces.

Wolf and coworkers used the Cu(111) and CO/Cu(111) to study TPPE excitation mechanisms for clean surface image states and adsorbate induced states [53,54]. A direct excitation versus an indirect excitation mechanism can be distinguished by using $s$ and $p$ polarized light to populate the unoccupied intermediate states. Direct excitation means that the intermediate state is populated by directly coupling between an initial state and the final state. For indirect excitation, the intermediate states are populated by scattering

and relaxation of photoexcited nonequilibrium hot electrons from the substrate. On the Cu(111) surface, they observed a direct excitation for the $n = 1$ image state. For CO induced $\sigma$, $\pi$, and $2\pi^*$ states, an indirect excitation process was determined for the $\sigma$ state and a direct excitation for both the $\pi$ and $2\pi^*$ states. They also measured the transition dipole orientation for the excitation process.

Recent interests in utilizing the self-arrangement property of the self assembled monolayer (SAM) as molecular electronic devices have prompted the studies of SAM electronic structures on metal surfaces [47]. A series of complicated adsorbate induced states were observed. Most importantly, the electron is localized at low adsorbate coverage, which corresponds to the formation of islands on the surface. At higher coverage, where the islands began to coalesce, electron was delocalize throughout the surface. This is important in determining the critical distance between the nearest molecular devices before cross linking can interfere with the performance of each device.

Two photon photoemission has also been used in studying the effects of adsorbates on image state electron properties. It has been shown that for a physisorbed layer, the electron affinity of the adsorbate is most critical in determining the binding energies, lifetime, and effective mass of image states electrons. For attractive adsorbates such as Xe, image state electrons tend to reside in the Xe layer, resulting in the formation of quantum well states [6, 32, 55]. On the other hand, a repulsive adsorbate like alkane molecules tends to push electron outside the layer, effectively decoupling the electron from the metal and leading to a longer electron lifetime. The long lifetime allows the image state electron to induce structure rearrangement that leads to electron localization and solvation at the in-

terface [6, 30]. With growing interest in the physics of image state, excited state electron dynamics, and transport properties at surfaces and interfaces, TPPE has become an important tool in the study of surface chemistry, electrochemistry, and electro-optic materials.

# Chapter 3

# Experimental

Two photon photoemission experiments combine the use of an ultrafast laser and an ultra high vacuum system. The ultrafast laser with pulse width on the order of electron lifetime at the sample metal surface is used to probe the electron dynamics on the Ag(111) surface. The Ag(111) sample reside within an ultra high vacuum chamber that ensures the cleanliness of the metal surface for the duration of the experiments. The diagram of TPPE apparatus is shown in Figure 3.1. A brief overview of the vacuum and laser system will be presented in the current thesis since many details regarding the experimental setups have been reported in prior theses [35, 56–59].

## 3.1 The Laser System

The laser system used in the experiment is purchased from Coherent, Inc. The system consists of an Innova 400 Ar-ion laser, a Mira Model 900-F Ti:Sapphire oscillator, a RegA Model 9000 Ti:Sapphire regenerative amplifier, and an optical parametric amplifier

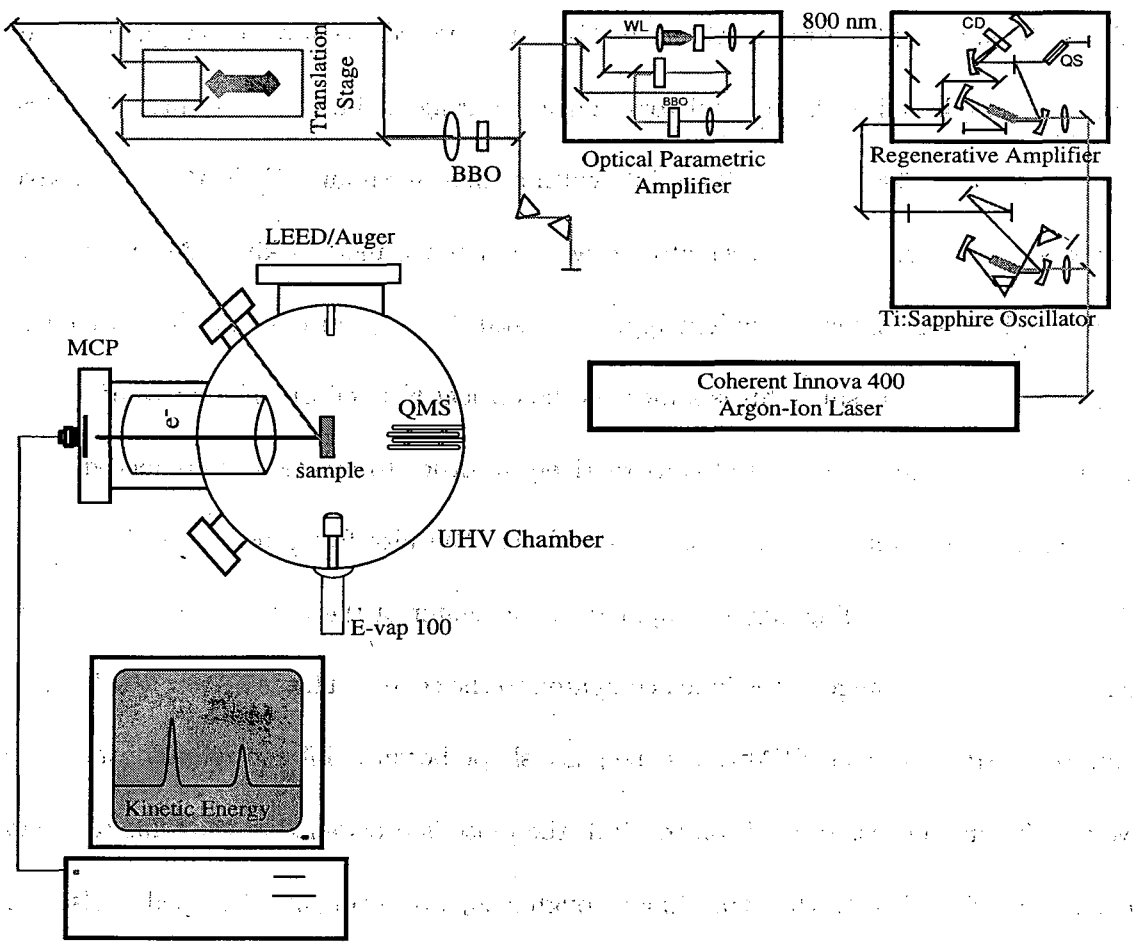


Figure 3.1: Schematic of the experimental apparatus.

(OPA). Innova 400 Ar-ion laser that operates at multiline emission produces a 22 watts light that is used to pump both the oscillator and the amplifier. The oscillator is pumped by 8 watts of power that was split from the Ar-ion laser to create a population inversion in the Ti:Sapphire crystal that serves as the gain media in the cavity. Since the Ti:Sapphire amplifies all wavelength between 680 nm to 1100 nm, the reduction of the amplified wavelength is accomplished with laser mirrors and a birefringent filters. Currently the Mira pulse is centered at 798 nm with 10 nm full width at half maximum (FWHM). A saturable absorber system is used in the oscillator to achieve passive modelocking. As the intense laser pulse alters the index of the Ti:Sapphire crystal, the crystal narrows the laser beam that passes through the slit. This is known as the optical Kerr effect. The phase of a large number of modes are timed to add constructively in order to create a mode locked, high peak intensity pulse for the formation of Kerr lens. The ultrafast pulse is less intense at both its leading and trailing edges compared to the center of the pulse, therefore the two edges will cause less change in the index compared to the center. This is known as self phase modulation (SPM). In fact, SPM alters the pulse shape because different parts of the pulse move at different speeds. In addition to SPM, the pulse is broadened in time due to group velocity dispersion (GVD) while traveling through lenses, resulting in a "chirped" pulse. To compensate for SPM and GVD pulse broadening, a pair of prisms is used as negative GVD to recompress the pulse. Autocorrelation of the oscillator is 198 fs with a width of 140 fs. The repetition rate of the oscillator is 76 Mhz with 850 mW mode locked output power.

The Ti:Sapphire regenerative amplifier, RegA 9000, is pumped by 14 watts of power generated by the Ar-ion laser. An acoustic-optic Q-switch holds off spontaneous

lasing in the amplifier cavity until a 140 fs seed pulse from the oscillator has been injected into the cavity. The injected oscillator pulse is broadened first by a cubic polarizer, then by the Q-switch $TeO_2$ crystal. After 20 to 30 round trips in the cavity, the injected pulse reaches the maximum energy before being ejected by an $SiO_2$ acousto-optic cavity dumper. The amplified pulse is about 40 ps in length. The index of refraction of the $SiO_2$ crystal is altered by an acoustic pulse and thus diffracts the dump pulse away from the cavity. The broadened RegA pulse is then recompressed with a 4-pass pulse grating compressor. The final output pulse centers around 800 nm with 760 mW power and 260 fs pulse width at 200 kHz repetition rate.

Optical parametric amplifier (OPA) uses 25% of the RegA output to generate a white-light continuum that contains spectrum from ultraviolet to mid-infrared. The white-light continuum is used to seed the BBO crystal in the OPA. The rest of the RegA output is frequency doubled by focusing the 800 nm RegA beam into a 1 mm thick Type I BBO crystal to generate the 400 nm "pump" beam. Through optical mixing of the "pump" beam in a second BBO crystal, the "signal" beam and the "idler" beam that conserve the energy of the "pump" beam are generated. Changing the direction of the "pump" beam entering the BBO crystal tunes the "signal" beam from 500 nm to 700 nm, and changes the idler beam simultaneously from 2000 nm to 933 nm. The OPA output at 680 nm is approximately 25 mW in power. Group velocity dispersion compensated by two prisms result in 120 fs pulse width measured by autocorrelation. A spectra of TPPE autocorrelation of the surface state is shown in Figure 3.2. Part of the compressed pulse is frequency doubled by another BBO crystal to generate the UV (the pump) beam in TPPE. The first dichroic mirror separates

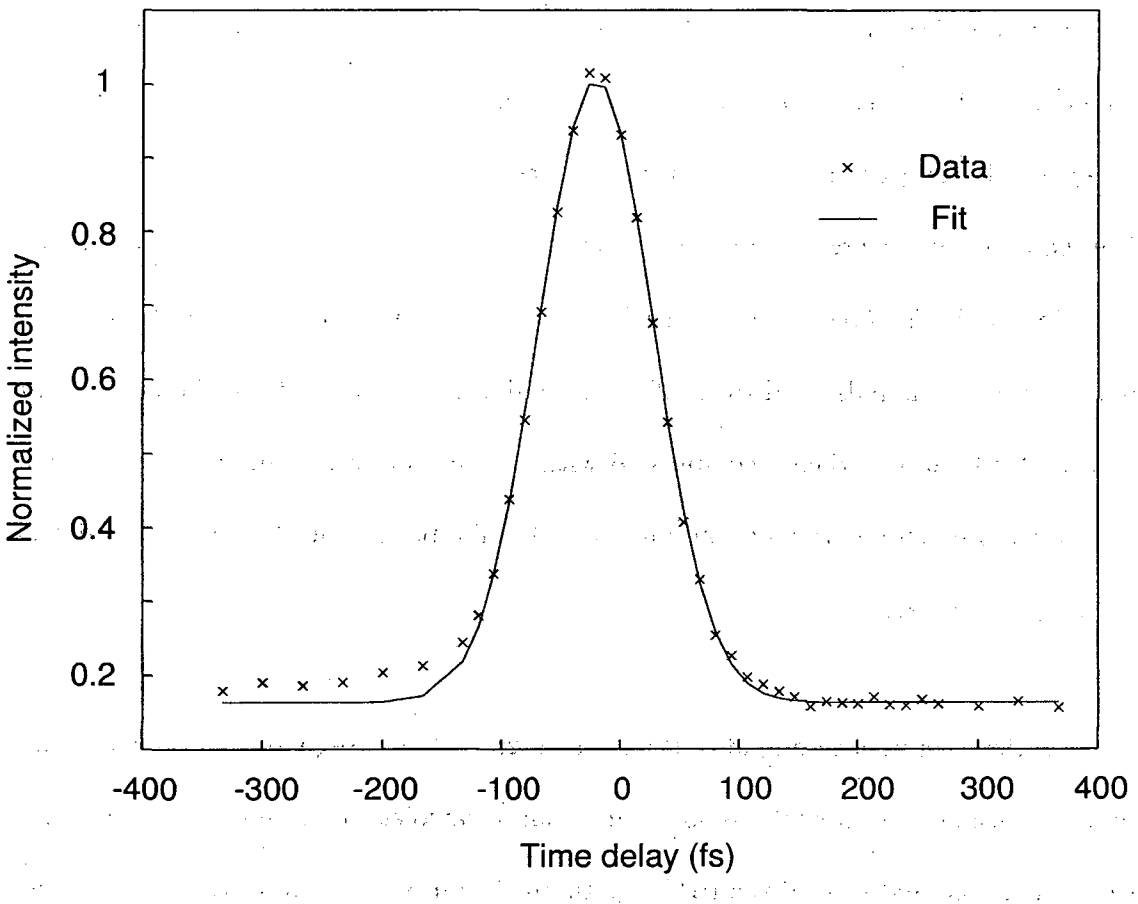


Figure 3.2: Autocorrealtion from the dynamic data of TPPE. The result of TPPE is fit to a Gaussian function with a FWHM of 113 fs.

the UV and the visible (the probe) beam. The visible beam goes through a delay stage then recombines with the UV beam using a second dichroic mirror. The recombined beams must be overlapped both in time and space to produce a two photon excitation in bulk metal. The spatial overlap is accomplished by turning mirrors in the beam path to assure both the visible and the UV lights travel parallel to each other. By adjusting the delay stage for the visible light, the two beams can be overlapped temporally. Both beams are sent through a chamber view port onto the sample surface.

## 3.2 Ultrahigh Vacuum System

In order to conduct studies of image potential state on a surface with minimum contamination, the sample crystal is placed in an ultra high vacuum (UHV) environment. A variety of equipments were built onto the chamber for the TPPE experiments. Detail descriptions of the chamber has been reported in the thesis of Merry [56]. The ultra high vacuum chamber is equipped with a Varian 400 L/s triode ion pump and an Edward EXT 250 turbomolecular pump system. Under normal operations, only one pump will be used on the chamber at a time. The turbomolecular pump is used to remove molecules from the chamber while the pressure is above $1 \times 10^{-8}$ torr, or while the molecules are desorbing from the sample. Thereafter the ion pump is used to achieve a base pressure of $5 \times 10^{-11}$ torr.

A Ag(111) single crystal sample is used for experiments described in this dissertation. The silver crystal is mounted to a sample manipulator that provides precise translation of the sample along three Cartesian coordinates and two rotations. Rotation about the x-y plane allows electrons to be photoemitted at different angles for angle-resolved TPPE. Rotation about the z-axis of the sample allows applications of other instruments installed on the chamber. Heater and liquid helium flow cryostat equipped on the sample holder allows the Ag(111) sample to reach temperatures between 50 K and 725 K. Thermocouple attached to the sample allows precise reading of the sample temperature.

The Ag(111) crystal is subjected to repeated cycles of sputtering with Ar at 500 K for 20 minutes and annealing at 725 K for 20 minutes to maintain the cleanliness of the surface. Sample cleanliness is verified with an Omicron LEED/Auger spectrometer along

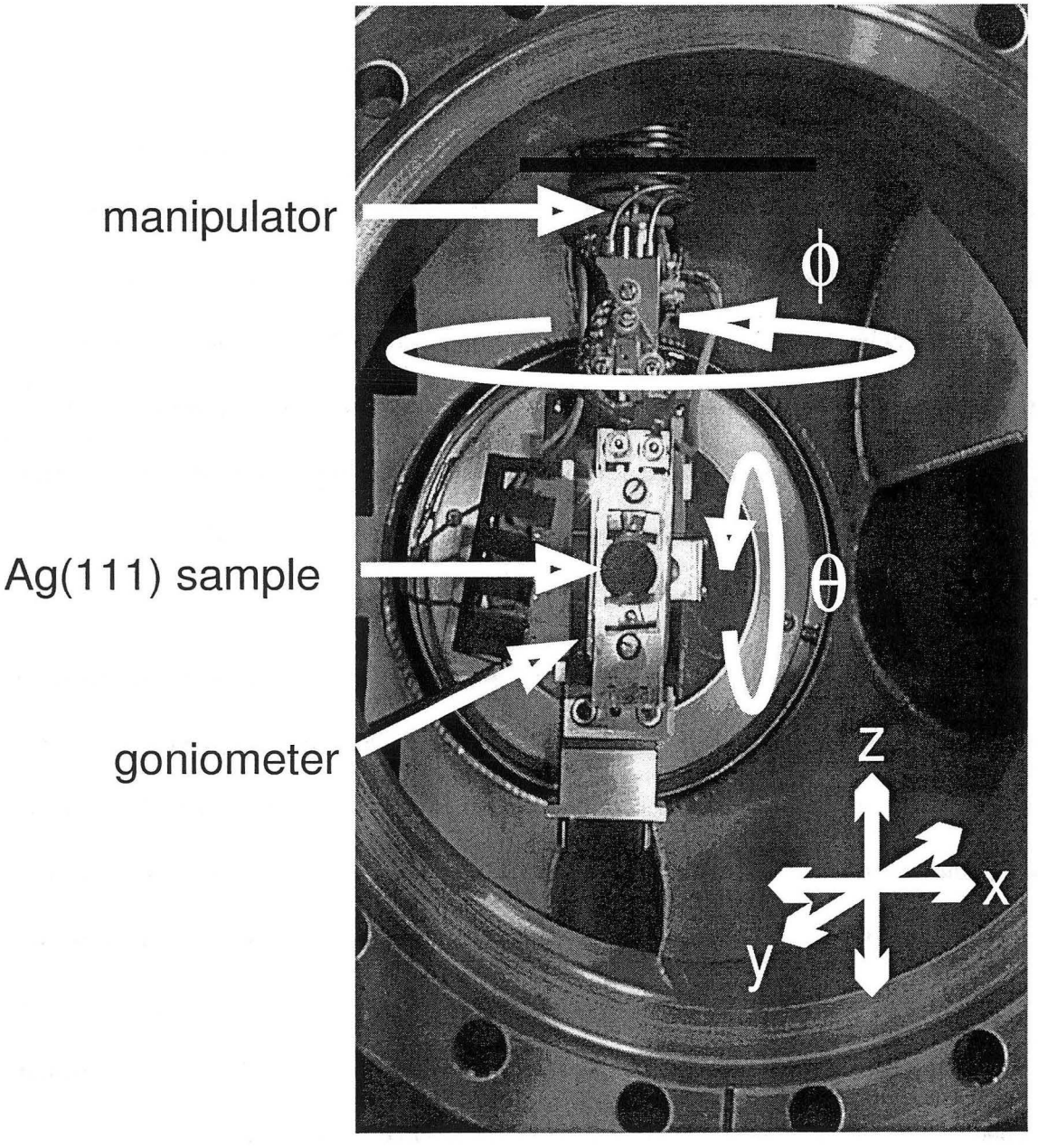


Figure 3.3: Sample manipulator provides precise motion required for experiments in the UHV chamber. Goniometer provides the angle rotation needed in angle-resolved TPPE

with TPPE. Auger spectrometer is used to identify the atomic species present on the surface. The LEED is used to determine the orientation of the surface as well as the orientation of the layer growth. Detailed description of the operation procedure and technical information of the Omicron LEED/Auger spectrometer has been reported in the thesis of Wong [35]. A TPPE and Auger spectra for clean Ag(111) surface is shown in Figure 3.4. A quadrupole mass spectrometer is also used to identify molecules inside the UHV chamber.

A leak valve or a miniature evaporation system is used to grow thin adsorbate layer(s) on the sample surface. The leak valve is attached to a high vacuum sample line at which the gaseous sample is first purified via freeze-pump-and-thaw technique before being introducing into the chamber. Layer growth by vapor deposition is accomplished by opening the leak valve and expose the Ag(111) sample to the vapor of desired adsorbates. Layer by layer growth is calibrated by comparing different surface exposures to TPPE spectra and LEED pattern. The evaporation system produces metal or semiconductor molecular beam which is used for epitaxy growth of refractive materials. Picture of the purchased E-vap 100 is shown in Figure 3.5. The E-vap 100 uses an electron beam power source for thermionic emission to generate a constant beam of electron. The electron beam is then used to bombard an 1-millimeter diameter metal wire of material to be deposited in order to generate a constant stream of molecular beam. Source aperture collimate the molecular beam as it exist the evaporation system. The wire is mounted on a manual linear drive feed through, and must be feed periodically in order to maintain a constant evaporation rate. During deposition, the Ag(111) sample is placed in direct line of sight of the evaporation head to maximize the deposition rate.

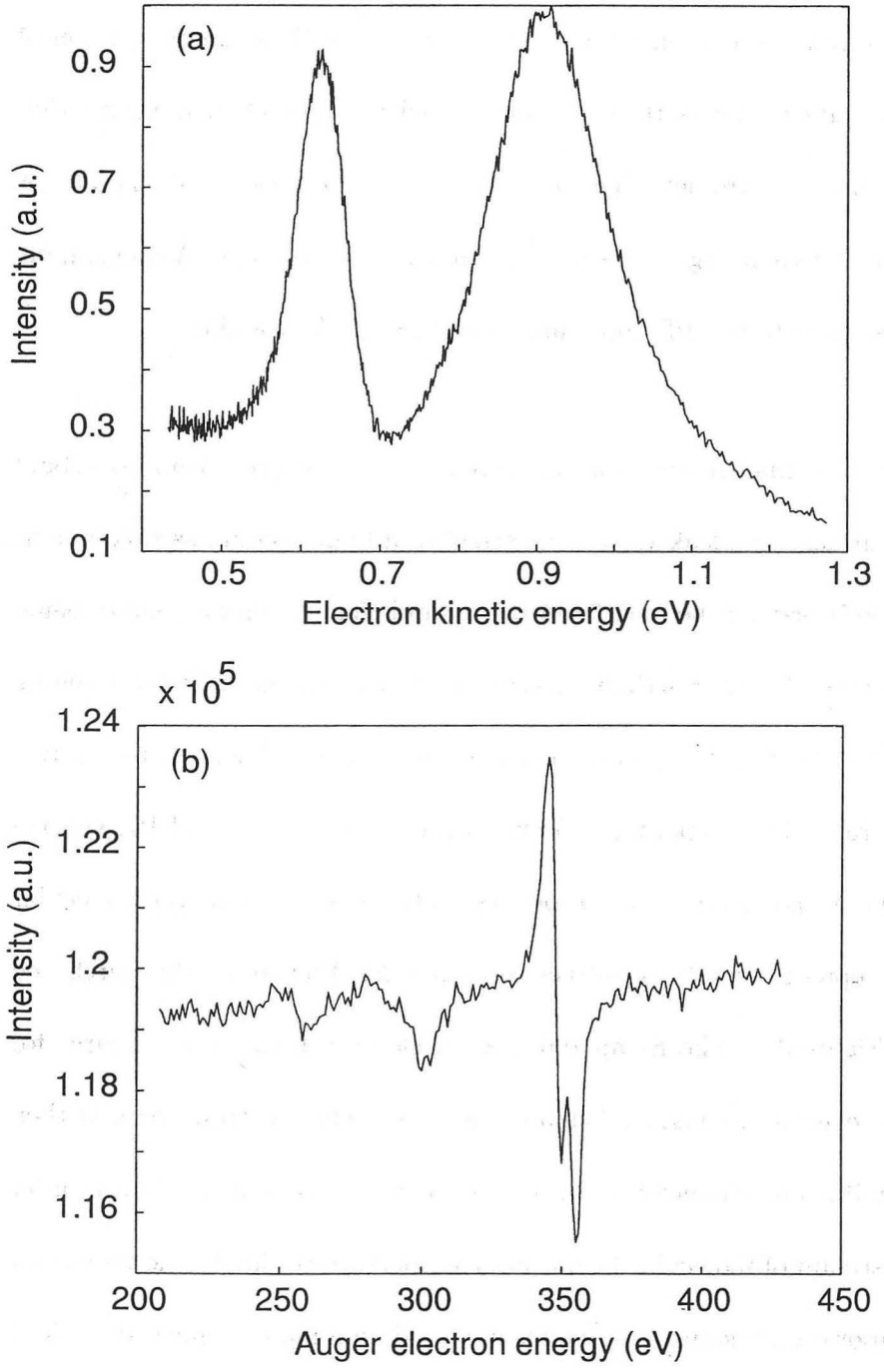


Figure 3.4: (a) TPPE spectra of a clean Ag(111) surface at 708 nm. Two peaks shown in the spectra are the surface state (left) and the n=1 image potential state (right). (b) Auger spectra of a clean Ag(111).

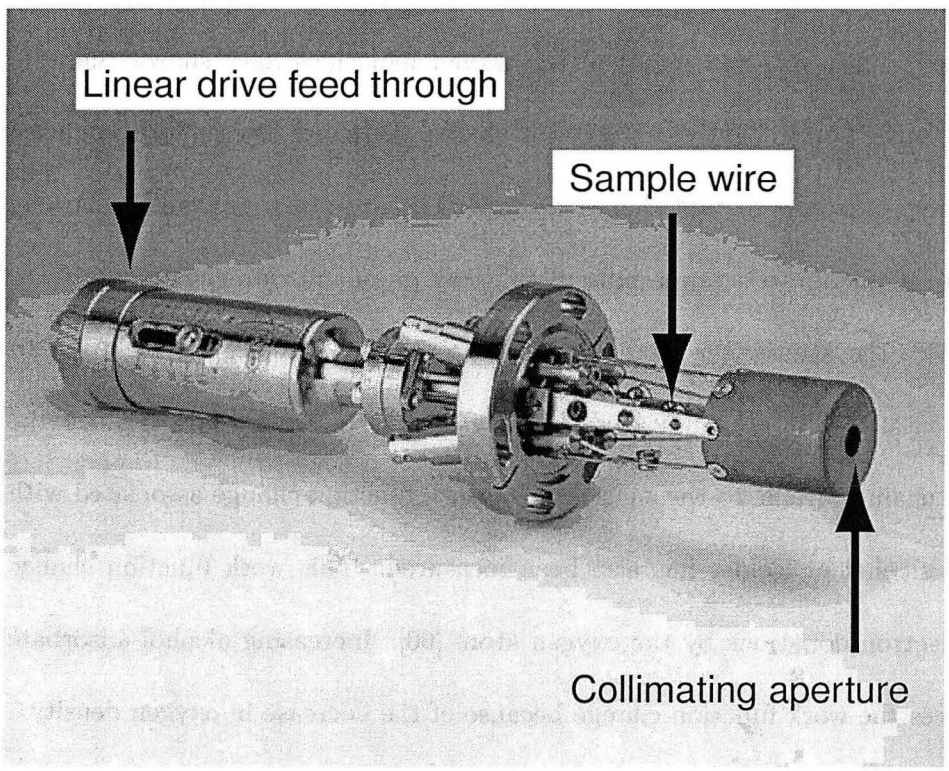


Figure 3.5: Evaporation doser, E-vap 100, from MDC. Evaporation doser is used to grow refractive materials on Ag(111).

## 3.3 Alcohol Molecules Solvation Experiments

Alcohol molecules adsorption on a Ag surface has been studied by Gellman, et al. [60, 61], Kleyn, et al. [62], and Weinberg, et al. [63]. Through high-resolution electron energy loss spectroscopy, Gellman and coworkers were able to identify vibrational structures of alcohol molecules adsorbed onto a Ag(110) surface. Comparison of vibrational stretch between monolayer, multilayer, and liquid phase alcohol molecules have shown that the presence of the Ag surface only slightly perturbs the alcohol molecules. Angular dependence of the electron energy loss cross section identified the C-O bond to be roughly align parallel to the surface from methanol to octanol molecules. X-ray photoemission spectroscopy was also used to identify the adsorption geometry of the alcohols molecules on the Ag(110) surface. Experimental results also indicated that the alcohol molecules adsorbed on the surface with alkyl chains parallel to the surface. The work function change associated with the adsorption of alcohol molecules has also been measured. This work function change is attributed to electron donations by the oxygen atom [60]. Increasing alcohol adsorbate chain length reduces the work function change because of the decrease in oxygen density.

For the alcohol molecules on Ag(111) experiments, Aldrich spectra grade anhydrous methanol, (1)d-methanol,1-propanol, 1-butanol, and 1-pentanol were used. Samples were transferred in a nitrogen dry box onto the sample line with a base pressure of $5 \times 10^{-7}$ torr. Alcohol sample was then purified by repeated freeze-pump-thaw before being introduced via a leak valve into the UHV chamber.

The layer growth characterization of different alcohol molecules on Ag(111) surface was accomplished with TPPE and LEED. Adsorption temperature was determined by

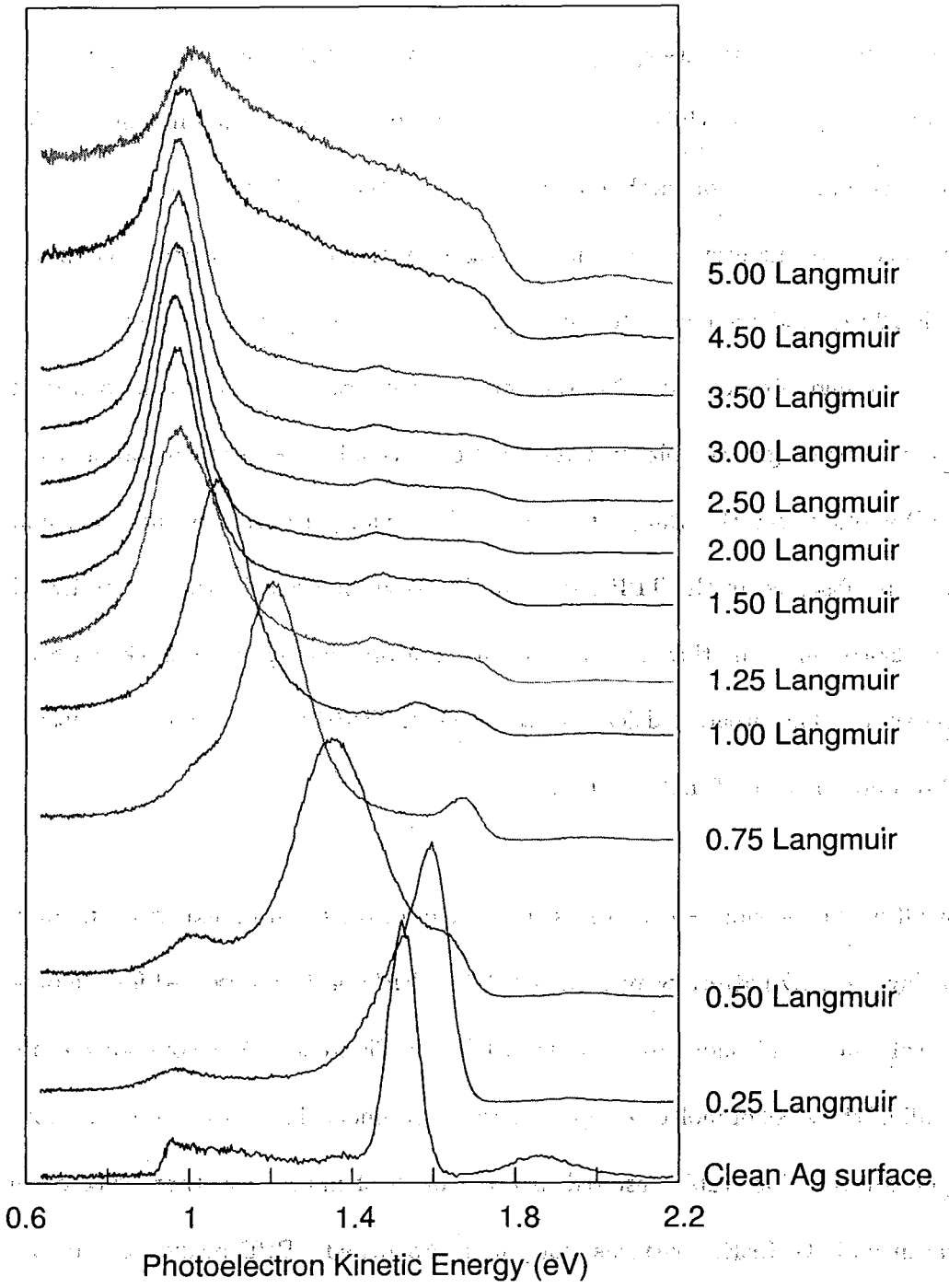


Figure 3.6: Methanol/Ag(111) coverage dependent TPPE spectrum. The monolayer coverage is determined to be between 2-3.5 Langmuir, where there is no change in the TPPE spectrum.

keeping a back pressure of the adsorbate molecules in the chamber while slowly lowering the substrate temperature until adsorption was observed with TPPE. Holding the substrate at the adsorption temperature while increasing the surface coverage results in a steady decrease in the work function. For methanol adsorption on the Ag(111) surface, Figure 3.6 shows TPPE spectra of increasing methanol coverage. In this case, monolayer adsorption temperature is 120 K, and the complete monolayer surface coverage was determined to be between 2 to 3.5 Langmuir exposure. No apparent work function change can be observed between those two coverage. Monolayer determination was validated with the observation of sharp LEED spots within this range of coverage. At monolayer coverage, the $n = 1$ and $n = 2$ states were observed in the TPPE spectra. Increased methanol exposure at 120 K yields a slow adsorption of multilayers, which resulted in broadening of the peaks with no visible LEED spots. The broad and featureless peaks in TPPE spectra at high exposure reflect the disordered nature of multilayer adsorption.

For all of the alcohol adsorbates used in the electron solvation experiments, only ordered monolayer LEED pattern were observed. The LEED pattern observed for a monolayer coverage of different alcohol adsorbates is sketched in Figure 3.7. As a common feature observed for all of the alcohol molecules used for the experiment, increased exposure above the monolayer coverage inevitably resulted in the growth of multilayers that reflected in the disappearance of the LEED patterns along with broadened TPPE peaks. The monolayer adsorption temperature and exposure that resulted in monolayer growth and LEED pattern for each alcohol species used in the experiment is summarized in Table 3.1. As the alcohol molecules increase in chain length, the adsorption temperature become higher and

Table 3.1: Monolayer adsorption temperature and coverage exposure

| Adsorbates | Monolayer adsorption temperature | Monolayer coverage exposure |
|---|---|---|
| Methanol | 120 | 2-3.5 |
| Propanol | 160 | 1 |
| Butanol | 170 | 0.5-1.5 |
| Pentanol | 180 | 1 |

the exposure required for a monolayer adsorption decreases.

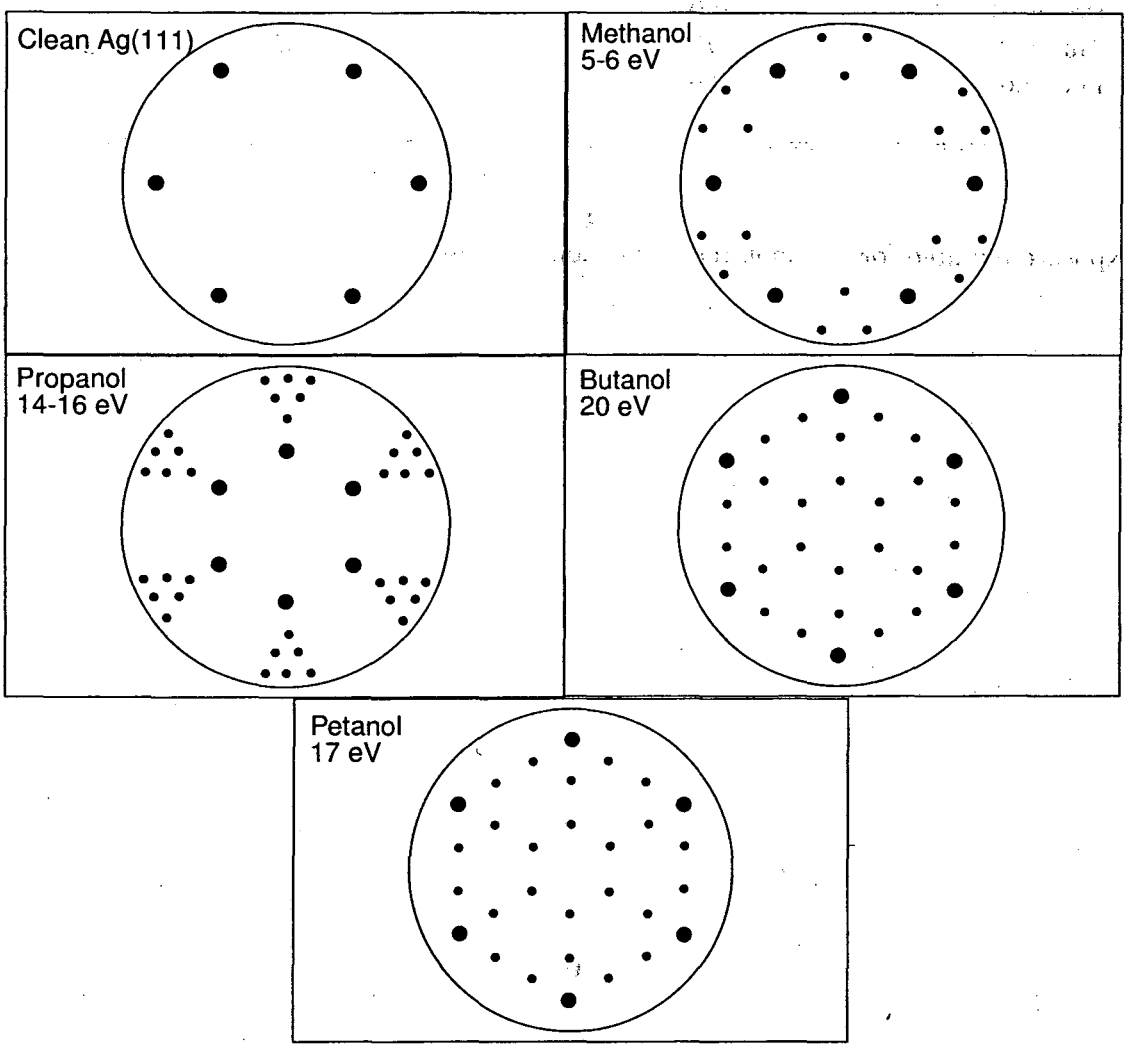


Figure 3.7: Observed LEED patterns for different alcohol molecules monolayer adsorbed on the Ag(111) surface. Observation of LEED pattern indicates alcohol molecules form order layer on Ag(111). Electron beam energies used to obtain the LEED patterns are also included in the figures.

# Chapter 4

# Electron at a Polar Adsorbate/Metal Interface

The interactions of solutes with their surroundings is a subject of great importance since these interactions determine many of the physical and chemical phenomenon that take place in the condense phase. The rate of chemical reaction that takes place in the condense phase largely depends on the mechanistic details of the solvation process. Electron solvation represents one of the most fundamental type of solvent-solute interaction. Two dimensional electron solvation at the metal/alcohol interface represents the first ever studies of electron solvation in reduced geometry as well as at an interface. The first part of the chapter is devoted to an overview of previous solvation experiments that take place in the liquid or glass medium. The concept of work function and local work function is presented in the second section in this chapter. It is necessary to present these two seemingly trivial but in reality not so simple concepts because the observation of electron solvation by TPPE relies

on applications of the local work function theory. The last part of the chapter includes the experimental results and discussions of the systematic studies of electron solvation by alcohol molecules on a Ag(111) surface. Electron solvation in alcohol is used to compare with electron solvation observed in nitriles.

## 4.1 Previous Solvation Experiments

Ever since the first observation of solvated electron in ammonia by Kraus [64], kinetic and thermodynamic properties of solvation has been a topic of intense research. The development of the radiolysis experiments during the 60's opens the way for electron solvation studies by providing an efficient and reliable means to generate excess electrons. Radiation pulse photo ionize electrons from the medium, "hot" excess electron can then interact with the surrounding molecules. Absorption spectra taken immediately following the radiation pulse provides the energy of the excess electrons as they interact with the solvent molecules. The first direct observation of the electron solvation process was reported by Baxendale and Wardman [65]. After irradiating alcohols sample, they observed an appearance of the optical absorption band of solvated electron. Time evolution of the absorption spectra was used to explain the process of electron solvation.

Following Baxendale and Wardman, numerous experimental [66–77] and theoretical works [78–83] contributed to further understanding of the physics of electron solvation. Kevan and coworkers [67] studied electron solvation in various alcohol glasses at 77 K by pulse radiolysis and later by photoionization [73]. In each alcohol glass, trapped electron transient absorption spectra blue shift on a microsecond timescale. The rate of spectra

diffusion occurs faster for more polar solvent. They suggested dipole reorientation around the solute is responsible for the transient spectra shift. Initially the electron is trapped in a shallow potential well, electrostatic interaction between the trapped electron and the surrounding dipole promotes the reorientation of the molecular dipole to produce a deeper potential well. Stronger short range interaction between the electron and the more polar solvent results in faster blue shifts. Temperature dependent studies indicate samples placed at higher temperature results in higher electron solvation rate constants. At lower temperature, the molecular dipoles still undergo reorientation, albeit a hindered motion. A semicontinuum model was proposed by Kevan [78, 79] to explain the effect of dipole reorientation, spectra shifts, and temperature effects. Parameters such as solvation radius and solvent angle were calculated as a function of temperature to compare with experimental results. The fastest solvent response was obtained by Kevan with nanoseconds time resolution.

Higashimura and coworkers studied electron solvation in various organic glasses between 4 K and 77 K by gamma ray radiolysis [66]. At 4 K, the absorption band was attributed to trap electrons at pre-existing traps where molecular dipoles remain unrelaxed. Upon annealing the sample from 4 K up to 77 K, they observed the band blue shifts, which they explained as the gradual reorientation of the molecular dipole as "trapped" electron transforms to "solvated" electron. Cooling the initially solvated electron from 77 K down to 4 K also resulted in absorption band blue shifting. In this case, although the molecular dipole has relaxed and reached equilibrium structure with the presence of the electron at 77 K, lowering the temperature causes the contraction of electron traps in the organic glass.

and results in the spectrum blue shifting.

A different solvation model was proposed by Kroh [83], Salmon [76], and Funabashi [80, 81] to explain electron solvation. Funabashi argues that the two absorption band observed in alcohol glasses should not be described as "trapped" or "solvated" electrons, but instead they were electrons at two different trap sites: the hydrogen bonded OH chains and the alkane part of the molecule. Migration of trapped electron from shallow traps, the alkane site, to deep traps, the OH-chain traps caused the change in absorption spectra. Salmon and Kroh [76] further points out the change in spectra is not due to dipole reorientation, it is due to either the loss of electron to recombination reaction in the glass or migration of electron from shallow traps to deep traps. At extremely low temperature, about 4 K, the viscosity in these system is too high, which relegates the reorientation of the dipole to a minor role in electron solvation. Instead the migration seems to be the more likely explanation for the spectral changes at shorter times and lower temperature.

Similar to results observed in alcohol glasses studies, electron solvation in liquid alcohols also exhibits two distinct species of electrons: trapped electrons and solvated electrons [84–88]. Initially trapped electrons absorb in the infrared spectrum; subsequently the electrons rapidly solvate and transform into visible absorption. The formation time of the solvated electrons have been measured by many different research groups. Measured with picosecond time resolution, the solvation time varied between 1 to 50 picoseconds for various aliphatic alcohols. At short times, initial localization of the quasi-free state takes place either by a configuration fluctuation or by a preexisting trap in the liquid. Subsequent solvent rearrangement near the trapping site results in a solvated electron. Two different

time scales were obtained from the experiments, an instrument limited fast component (less than a picosecond) and a slower component. The slower component was found to correlate with dielectric relaxation time of the liquid, indicating that the orientational relaxation was the dominant mechanism in structural reorganization.

Time dependent fluorescence Stokes shift experiments has also been used to investigate solvation dynamics of larger solute molecules [89–93]. The uncharged, rigid molecules, inside a polar solvent is excited by a short pulse. Excited state solute creates a strong local field on the surrounding solvent to rearrange and form a configuration that solvates the excited state solute. As these solvent rearrangement takes place, the solvent perturbs the electronic state of the molecule, and causes changes in the solute emission spectrum. The emission spectrum of the excited state changes as the solvent relaxes around the excited molecule. Time resolved spectra changes are linked to the dynamical movement of the solvent. Through out the dipole solvation experiments, the observed solvation time does not depend on the probe molecule used and appear to reflect primarily the properties of the polar solvent studied. Time scales observed in these solvation studies are shown to be related to the longitudinal and Debye relaxation time of the solvent.

Recent development of the ultrafast laser allows probing of the solvation dynamics on a femtosecond time scale. Examination of short time solvation dynamics reveals an ultrafast component of energy relaxation that was not able to be observed before. Transient absorption femtosecond studies of electron solvation in alcohol liquids conducted by Barbara and co-workers show that the solvation process is complex, especially in the short time regime after electron creation [8, 94, 95]. They suggest that the observed 300 fs relaxation

time is due to either the radiationless transition from the electronically excited "p" to the "s" ground state or to the alcohol molecules solvation of the excited "p" state electron. The slower time scale seen in the experiment is attributed to the slower diffusive solvation motion, similar to those observed in photoionization and photolysis experiments. Ultrafast fluorescence Stokes shift studies of chromophore in polar solvent by Fleming illuminated the complexity of the ultrafast solvation dynamics [17, 89, 96, 97]. Multiple solvation time scales were observed for coumarin 343 (a large fluorescence dye molecule) solvation in liquid ethanol. The fast relaxation has a time constant of $\sim$ 60 fs that accounts for the majority of the energy relaxation. This ultrafast phase of solvation has been observed in many solvent studies and varies little from solvent to solvent [98]. The nature of the short-time solvent response was attributed to the isolated individual molecular interaction between the solute and solvent, which is labelled as the inertial motion. Each solvent molecules responded as individual solvent molecules without the presence of other solvent molecules. Similar results were also observed in the molecular dynamic simulations by Maroncelli [99]. Molecular dynamic simulations have also shown that the inertial motion involved mostly the reorientation of the solvent molecules in the first few solvent shells around the solute. Solvation experiments of dye molecule in polymethylmethacrylate by Fleming and co-workers demonstrated that the inertial component of solvation is temperature independent between 300 to 30 K, unlike the slower diffusive component of the solvation [96, 97].

Along with the experimental advancement of observing solvation, different models were proposed to explain the results. Theoretical treatments of the dynamics of solvation can be divided into two approaches: the continuum model and the molecular model. Con-

tinuum model treats the condense phase as a collective object described by bulk parameters. Molecular model allows different molecular motions for individual molecules.

The continuum model treats the solvent as a homogeneous medium in which the only relevant property is its bulk, a frequency-dependent dielectric correlation function [89, 100]. The polar solute is replaced by a molecular cavity of some simple shape. The solvation energy is obtained by evaluating the reaction field of the polar solute molecule inside the molecular cavity. The dynamics are simply related to the solvent dielectric properties and the detailed solute-solvent interactions are ignored. More specifically, solvation time scale is proportional to the dielectric constant of the solvent in an infinite frequency electric field, the dielectric constant of the solvent in a static electric field, and the Debye relaxation time of the solvent. Continuum model predicts that solvation time in a fluid should be equal to the longitudinal relaxation time of the solvent. The continuum predicts single relaxation time scale, which is contrary to experimental observation. Experimental results indicate multiple solvation time scales, in which the long solvation time scales show qualitative agreements to longitudinal relaxation time of the solvent. Minding the molecular nature of the solvent, Wolynes [101], Rips [102, 103], and Nichols and Calef [104], proposed theories that involve more sophisticated treatments of the solvent. These theories model the solvent medium as a collection of hard polarizable spheres, whose dynamic properties are handled by the mean spherical approximation (MSA). The MSA model demonstrates that solvation dynamics proceed on multiple time scales. Most solvent exhibits two distinct time scales. The fast solvation time corresponds to the bulk relaxation time $\tau_L$, and the long time scales is associated with Debye relaxation time of the solvent, $\tau_D$. Depending on the distance

from the solvent to the solute, solvent responds to the perturbation in solute at different time scales. Another approaches to model solvation dynamics was proposed by Nichols and Wolynes [104, 105], and Bagchi and Chandra [106, 107]. They derived a generalized Smoluchowski equation to describe the solvent relaxation. In this description the dipolar solvent molecules undergo rotational and translational diffusion in a potential of mean force along with the mean force of the other surrounding solvent dipoles. This theory predicts that the solvation-time-correlation function will generally be non-exponential.

With the development of increasingly powerful computational capabilities, computer simulation of solvation becomes accessible. Maroncelli performed molecular dynamic simulation of electric field correlation function at a polar Lennard-Jones solute in spherical clusters for various solvents [99]. Simulation results indicated that solvation proceeds on multiple time scales. Analysis of the simulation data revealed that the majority of the energy relaxation occurs within the first few hundred femtoseconds. Furthermore, Maroncelli found that the ultrafast solvation dynamics was independent of solvent-solvent interactions. Identical ultrafast dynamics results were obtained for molecular dynamic simulations that included solvent-solvent interactions and those that excluded the interactions. To explore the underlining physics of solvation, Rossky and co-workers have performed numerous quantum molecular dynamics computer simulation of electron solvation in various solvents [9, 108–110]. The quantum energy gap between the electron ground state and the excited state was used as the probe of the solvation process. A 0.3-0.5 picosecond solvent response, which accounts for the majority of the energy relaxation, was observed for the electron solvation in methanol simulations. They attributed this fast solvation component

to the relatively fast, adiabatic response of the solvent. In separate studies, they pointed out that the ultrafast inertial component was the OH bond rotation. To solvate the electron, the methanol molecules orient the OH bonds toward the electron with the positive charge hydrogen closest to the solute.

## 4.2 Work Function and Local Work Function

Work function is the minimum energy required to remove an electron from the metal to a distance far away. More precisely, for an infinitely large uniform metal surface, the work function $\varphi$ is the potential energy difference between two states of the system: the initial neutral sample at 0 K, and the final state with an electron at rest infinitely away from the surface (not affected by the electrostatic image force of the metal) with the ionized metal remain at ground state [37,111]. Potential energy of these two states are often referred to as the Fermi energy, $E_f$, and the vacuum energy, $E_v$, respectively. The energy separation between $E_v$ and $E_f$ or the work function is composed of two contributions: the bulk chemical potential, $\bar{\mu}$, and the electrostatic surface potential, $\Delta\Phi$ (Figure 4.1). Work function is expressed as [111]

$$\varphi = E_v - E_f = \Delta\Phi - \bar{\mu} \tag{4.1}$$

The bulk chemical potential represents the electron's potential energy deep inside the bulk owing to the formation of the chemical bonds. Chemical potential is the bulk metal contribution to the work function, and depends on the nature of the solid. On the other hand, $\Delta\Phi$ is a pure surface contribution to the work function. As shown in Figure 4.2(a), electron

distribution at the surface is a step function at 0 K. However, at elevated temperature the electron density spills out beyond the surface, creating an excess electron density outside the surface while leaving a positive charge density inside the metal. As a result, the formation of the dipole layer at the surface (Figure 4.2(b)) contributes to the work function.

The surface potential contribution to the work function arises because the asymmetrical environment, with the bulk metal on one side and vacuum on the other side. The potential energy of the electron inside the metal is lowered by $\Delta\Phi$ because the electron is closer to the positive charged dipole layer compared to that in vacuum. For an infinitely large surface, the dipole layer is equivalent to two infinitely large parallel charged plates. The surface potential varies linearly with distance $z$ from within the two plates, but it is a constant outside the plates. Potential energy diagram of the work function for an infinitely large surface is shown in Figure 4.1. Since the surface potential for an infinitely large metal is a constant in $z$, the work function is also a constant in $z$.

The definition of work function usually applies to an "idealized" surface with the following properties: the metal is infinite in size and the surface of the metal is homogeneous. However, real surfaces are of finite size and composed of discrete atoms that create corrugation in electron density on the surface. For a real surface with finite size dipole layer at the interface, the electrostatic surface potential is not constant in distance $z$ outside the charged plates.

As shown in Figure 4.1(b), the solid angle $\Omega$ to the periphery of the finite dipole layer decreases with increasing $z$, and so does the surface potential $\phi_1(z)$ in Figure 4.1(a). At sufficiently far away from the surface, both the dipole layer and the surface potential

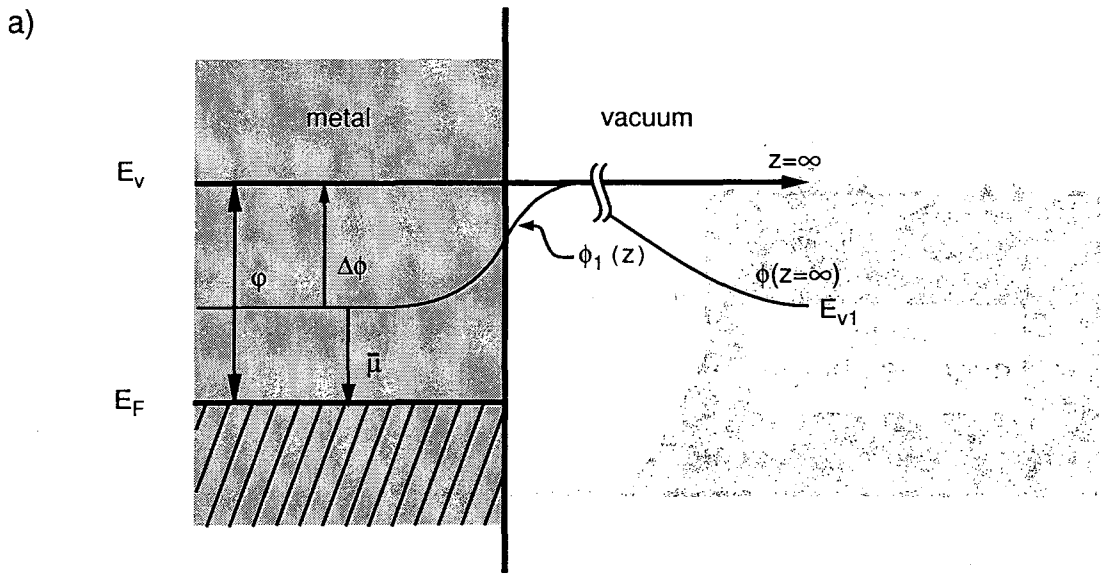


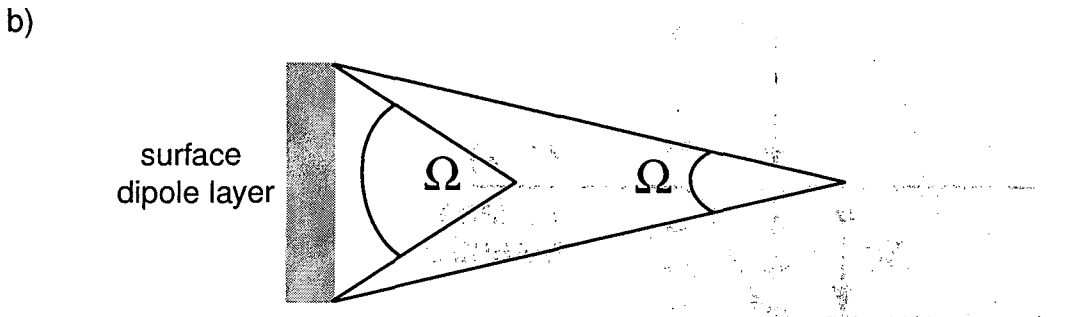


Figure 4.1: a) Potential energy diagram of the work function $\varphi$ for materials. The work function equals the sum of surface potential, $\Delta\Phi$, and the chemical potential, $\bar{\mu}$. As the electron moves across the surface dipole layer, the potential energy of the electron is lowered by $\Delta\Phi$. $E_v$ is the surface potential for an infinitely large metal, which remains constant in the vacuum. It is the vacuum energy of an infinitely large metal. $\phi_1(z)$ is the surface potential of a finite size surface. The surface potential decreases with increasing $z$. At $z = \infty$ the dipole layer can be considered as infinitesimal and the work function equals to the bulk chemical potential. $E_{v1}$ is the "global" vacuum energy for a finite size surface. b) The solid angle $\Omega$ to the peripheral of the dipole layer represents the surface potential of a finite size surface. Larger $\Omega$ results in a higher surface potential. At $z = \infty$ where $\Omega = 0$, the surface potential vanishes.

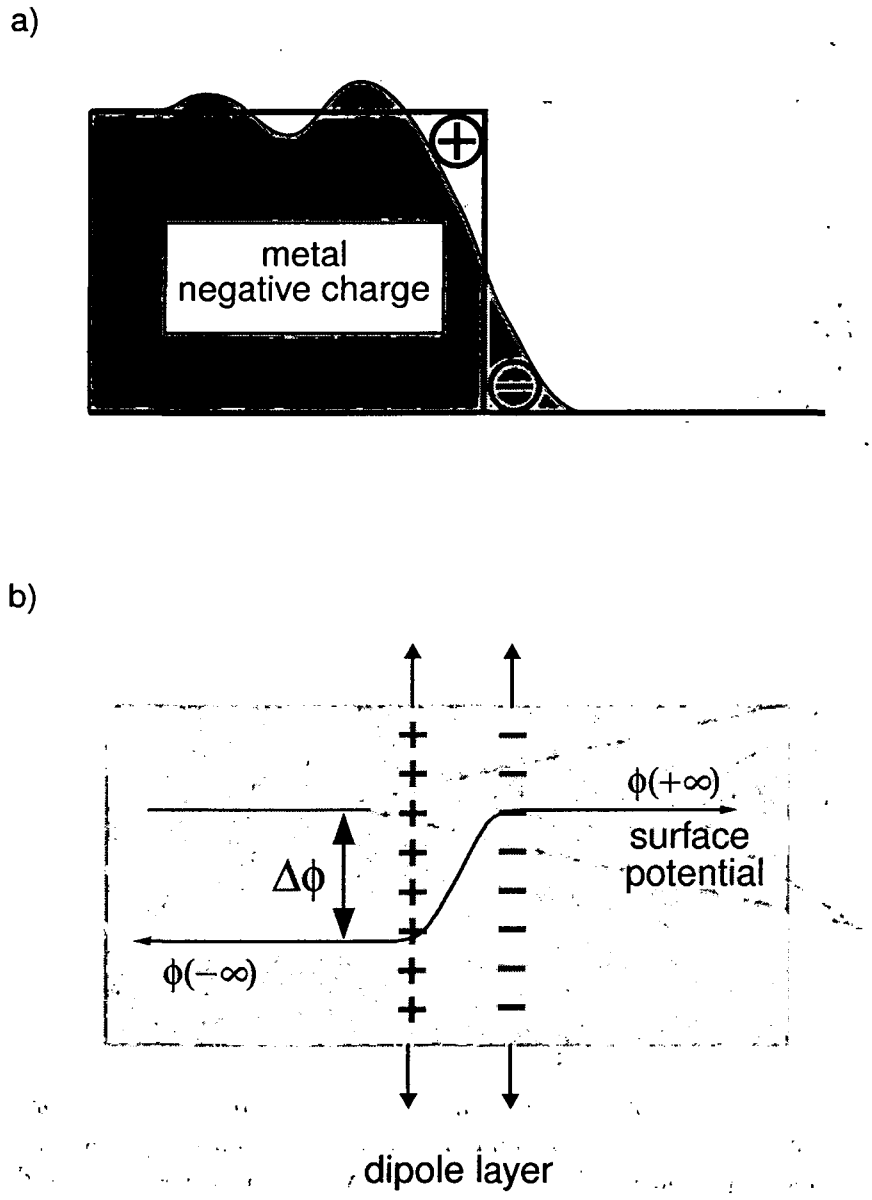


Figure 4.2: a) The electron density distribution at a metal surface. Electron density extends beyond the surface, causing an accumulation of negative charges outside the metal and positive charges inside the metal. b) Surface potential at the metal surface. A surface dipole layer arises due to the accumulation of charges at both sides of the surface. The potential energy across the dipole layer is $\Delta\Phi$.

can be considered as infinitesimal as $\Omega$ approaches zero. However, if the dipole layer is surrounded by other dipole layers, $\phi(z)$ will acquire an average value determined by the weight of the solid angles of the respective dipolar region. At infinitely far away from the surface, all surface potentials go to zero, and the work function of the metal reduces to only the bulk chemical potential, which is precisely the work function defined at 0 K (since no surface dipole layer exists at 0 K). The bulk chemical potential that the surface potential converges to far away from the surface is considered as the "global" vacuum level of the system. At large $z$, the work function is a constant with respect to the surface (parallel or perpendicular to the surface), as define by Equation 4.1. However, the work function close to the surface is not a constant since the surface potential $\phi$ is not a constant. In fact, the work function depends on where it is measured.

Unlike an ideal surface, real surfaces are made up of discrete atoms. A realistic surface contains atomic-scale defects such as point-defects, steps, adatoms, islands, patches, and heteroatoms. The atomistic nature of the surface results in corrugation of electron density [111]. For example, the orientation of the exposed crystal face affects the value of the work function because of different lattice arrangement and electron density. Figure 4.3(a) shows the picture of a typical surface with structures. Surface roughness leads to a charge redistribution and hence, variations in the surface potential, $\phi(x, y, z)$. Close to the surface, where the solid angle $\Omega$ is large, the surface potential, $\phi_1(x, y, z)$, $\phi_2(x, y, z)$, and $\phi_3(x, y, z)$, are distinct. These surface potentials are termed "local" surface potential because each potential acquires the characteristic charge distribution of the surface structure. A "local" work function of surface structures can be measured at a few Ångstrom away from the

surface where the local surface potential reflects the atomic detail of the surface. The local work function is defined as

$$\varphi_{loc}(x, y, z) = \phi(x, y, z) - E_f, \tag{4.2}$$

where $\varphi_{loc}(x, y, z)$ varies parallel and perpendicular to the surface [111, 112]. Further away from the surface, solid angle $\Omega_2$ includes different surface inhomogeneities. The surface potential takes on an average value from all the surface features and merges into a common "global" vacuum energy, $E_v$.

The local work function must be probed at a distance that is comparable to the size of the surface inhomogeneity in order to be sensitive to the surface features. Local work function should be measured at a distance $z < 2R$ from the surface, where $R$ is the radius of the surface structure. An image state electron that resides at few Ångstrom away from the surface can be used to measure the local work function of atomic scale surface inhomogeneities. The expectation value of the n=1 and the n=2 image state electron is 3 Å and 12 Å from the surface, respectively.

An electron which is removed from the metal also experiences an image potential while being moved toward the positive $z$ direction. The image potential, $\Phi_{Im}$, has been discussed extensively in the earlier chapter of this thesis. An image potential arises due to the electron polarization of the surface charge density, which results in an electrostatic attraction to an image charge in the metal. The image potential is a long range interaction that is on the order of $\sim 10^4$ Å. This is much longer compared to surface potential that converges to the vacuum energy within a few Ångstrom from the surface. Although the

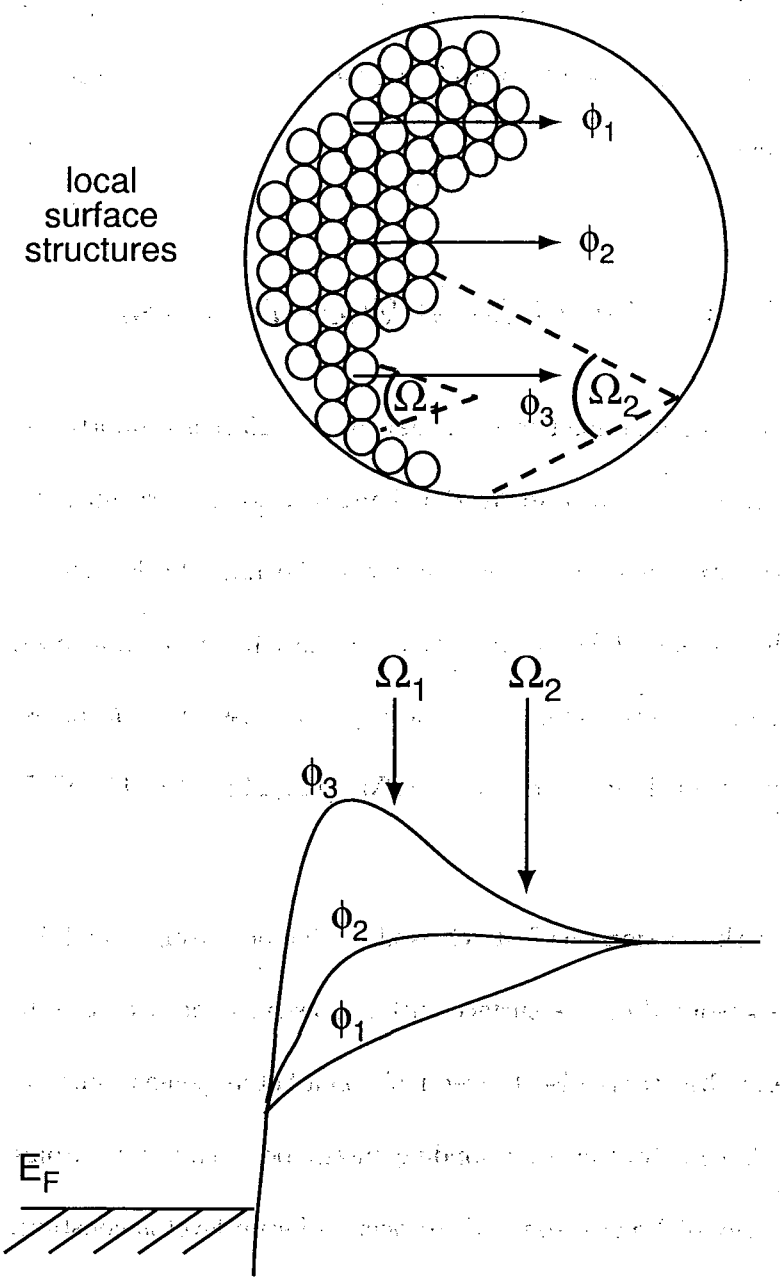


Figure 4.3: A real surface contains atomistic defects such as steps, islands, patches, and pits. Photoemission along different local surface structures will experience different surface potential, $\phi_1$, $\phi_2$, and $\phi_3$. Close to the surface, at solid angle $\Omega_1$, the surface potential reflects the charge distribution of a small area on the surface. Further away, at solid angle $\Omega_2$, the surface potential includes a large surface area of different structure. At far away from the surface, all the local surface potentials merge into one that takes on an average value of the entire surface.

complete potential should be expressed as $\phi(x, y, z) + \phi_{Im}(z)$, the image potential is not expressed in the definition of local work function because it can be considered as a constant compared to a local surface potential.

## 4.3 Experimental Observation of Local Work Function

The variation of the local work function perpendicular to the surface is proportional to the size of the local structure. In order to observe the changes in local work function caused by an atomic size surface structure, the work function probe must be located at a few Ångstroms away from the surface. Observations of local work function have been accomplished with several different experimental techniques: photoemission of adsorbed xenon (PAX) [111, 112], scanning tunnelling microscopy (STM) [113, 114], and TPPE [5, 115–117].

Measurement of local work function was first achieved by Wandelt using PAX [111, 112, 118]. At below 80 K, Xe is adsorbed on the surface with successive exposure. Due to the difference in adsorption energy, Xe atoms adsorb selectively on a heterogeneous surface, e.g. step-sites and terrace-sites. Because of the weak bonding energy between the Xe atoms and any surface, the binding energy of Xe electron with respect to Fermi level is constant. Meanwhile, the binding energy is modified by the local surface potential, which changes the electron binding with respect to the vacuum level. Since Xe atoms reside close to the surface, photoemission of adsorbed Xe electron can be used to probe the variation in local surface structures. Comparisons of the energy difference in the electron photoemission yield changes in local surface potential, i.e. local work function.

The PAX experiments carried out by Wandelt demonstrate the sensitivity of adsorbed Xe to a local work function. Photoemission from adsorbed Xe atoms on a 0.5 monolayer Cu on top of Pt(111) surface shows both the characteristics of Cu and Pt. The successive PAX spectra for increasing Xe coverage indicates a selective site adsorption for Xe. Because the adsorption energy of Xe on a Pt surface is higher compared to that of Cu, Xe preferentially adsorbs on Pt instead of Cu. Exposure of surface to hydrogen cause Pt to undergo a Cu induced surface rearrangement from Pt(111) to Pt(111)'1x1' reconstructed. Subsequent PAX can resolve Cu sites, Pt(111) sites, and Pt(111)'1x1' sites. This result demonstrates the extreme sensitivity of adsorbed Xe atoms to the local surface potential close to the surface.

Advent of the scanning tunnelling microscopy allows the determination of surface structures with atomic precision. Utilizing the STM tip's close proximity to the surface and its sensitivity to the tunnelling current, Sakurai and coworkers [113,114] were able to obtain the topographic image of Au/Cu(111) as well as the local work function. They measured the local work function for bare Cu, large Au terrace, the Au/Cu steps, and the Au/Au steps. The local work function measured at bare Cu and Au terrace agrees well with the Cu(111) and Au(111) work functions. On the other hand, the local work function measured at steps agrees with the Smoluchowski [119] smoothing model of induced surface dipole moments.

The local work function has also been observed by TPPE for metal overlayer on a metal substrate. The first system studied by TPPE was Ag/Pd(111) [115]. For a clean Pd(111) surface, only one peak that corresponded to the $n = 1$ image state of the Pd was

observed. At full monolayer coverage, only one peak appeared in the spectrum, the $n = 1$ image state of the Ag overlayer. This peak remained unchanged with further Ag deposition. Between the two coverage, two $n = 1$ states were observed, which corresponded to areas of different layer thickness. The image states assignment was substantiated by fitting a series of image states Rydberg series. The linear decrease of the work function reflects the growth of the Ag island prior to the completion of a monolayer. The image states reside close to the surface and its energies are perturbed by the surface electrostatic potential of the patches. The photoemission spectra of image states electrons reveal the work function of the individual patch at which the electrons reside. From the coverage dependent evolution of the TPPE spectra, Steinmann and coworkers were able to conclude layer-by-layer growth of Ag on Pd(111). In addition, local work function for Ag on Au(111) surface was observed by Borensztein [116] and Chambliss [117], and Ag on Cu(111) surface was observed by Wallauer and Fauster [5]. In each case, image states of the substrate decrease in intensity as the coverage of the overlayer increases. For each system, the work function decreases monotonically with increasing overlayer deposition until a complete monolayer coverage. At full monolayer coverage, only the image states of the overlayer can be observed. For the Ag on Au(111) system, additional deposition above monolayer coverage causes the $n = 1$ image state peaks to sharpen as well as the appearance of the $n = 2$ image state peak of the Ag overlayer.

## 4.4 Measurement of Work Function and Local Work Function with TPPE

Two photon photoemission first populates the unoccupied intermediate states, such as the image states, and subsequently photoemits electrons from these intermediate states. The photoelectron kinetic energy was measured via a time-of-flight method. A field free region between the metal surface and the electron detector is required to ensure an accurate determination of the photoelectron energy. The electric field within the flight region alters the velocity and kinetic energy of the electron. The field free region is achieved with 1) a colloidal graphite coated flight tube that shields most of the electron flight path from stray electric field and 2) a battery powered bias potential that compensates for the contact potential difference between the sample and the flight tube-detector assemble (Figure 4.4(a)).

The contact potential between the sample and the detector arises because their work functions are different. While both the sample and the detector are grounded to prevent surface charging, the difference in their vacuum energies causes the photoelectron to experience an electric field before entering the flight tube. By applying a battery powered floating dc bias between the sample and the flight tube-detector assembly, the difference in vacuum energies is removed (Figure 4.4(b)). Both the bias and the flight tube ensure a constant electron kinetic energy throughout most of the flight path.

To properly compensate for the contact potential, the work function difference between the sample and the detector must first be determined. The "true" image state binding energies can be determined by subtracting the photon energy from the photoelectron

kinetic energies in TPPE and then fitting the image state binding energies to Equation 2.5. The difference between the "measured" and the "true" image state binding energy is the proper contact potential or the work function difference. With the properly adjusted contact potential, further changes in the photoelectron kinetic energy would indicate either a change in the image state binding energy or a change in the sample work function. These changes can be brought about by altering the charge distribution at the surface, i.e. the surface potential ($\phi(x, y, z, t)$ in Figure 4.4).

As mentioned above, the first few image state electrons reside at a few Ångstrom from the surface, making them sensitive to local surface inhomogeneities. Patches of surface dipole have different local work functions. The image state electrons with different local work functions that are photoemitted from the same surface and same photon energy will manifest at different kinetic energies in the TPPE spectra (see Figure 4.4). As will be shown in the following sections, an electron solvated by dynamical reorganization of the surface dipole, which manifests in the time dependent local work function. In this case, Equation 4.2 can be rewritten as

$$\varphi_{loc}(x, y, z, t) = \phi(x, y, z, t) - E_f, \tag{4.3}$$

where both $\varphi_{loc}$ and $\phi$ are time dependent quantities.

## 4.5 Two-Dimensional Electron Solvation by Alcohol Molecules

Two dimensional electron dynamics upon photo injection into a metal/alcohol monolayer interface has been studied with time-resolved and angle-resolved TPPE. A thin

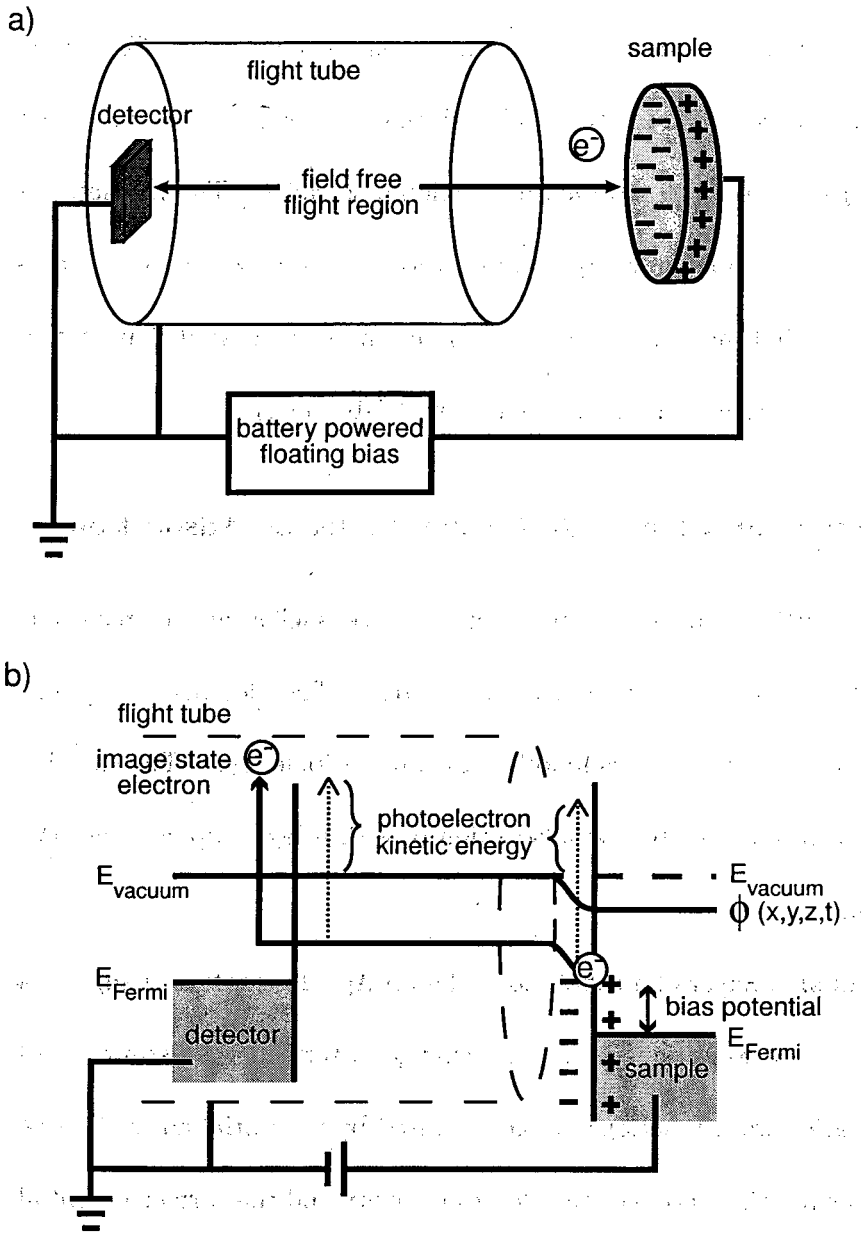


Figure 4.4: a) A flight tube and a battery powered bias that compensate for the contact potential difference create a field free flight region between the sample and the detector. b) By properly applying a bias between the sample and the flight tube-detector assembly, the difference in vacuum energies is removed. Dynamical reorganization of the surface dipole changes the surface potential, $\phi(x, y, z, t)$. Image state electron photoemitted from different surface potentials with the same photon energy (dotted line) manifests in different kinetic energies.

layer of adsorbates with a strong molecular dipole, in this case the alcohol molecules, interacts strongly with the photo injected electron that resides close to the surface. The strong electron-adsorbate interactions result in electron induced molecular reorganization similar to solute induced solvent reorganization observed in the liquid solvation. The mechanisms of molecular reorganization, dynamics of energy stabilization and localization are investigated with straight chain alcohol molecules (methanol, 1-propanol, 1-butanol, 1-pentanol) and deuterated molecules ( deuterated methanol, deuterated 1-butanol).

### 4.5.1 Static Work Function Change by Alcohol Molecule Adsorption

In general the adsorption of molecules on a metal surface, such as alcohol molecules on Ag(111) surface, modifies the work function of the system. The electrostatic surface potential contribution to the work function is modified by a new dipole layer. The chemical potential of the metal is also modified by the adsorption of a thin layer dipole molecules, however, this effect is small.

The adsorption of an adlayer of alcohol molecules on Ag(111) surface changes $\Delta\Phi$ in Equation 4.1 and hence, the work function. This change is termed the "static" work function change. This "static" work function change is caused by the initial adsorption geometry of the alcohol molecules that modifies the electron density and the surface potential. A "dynamic" change in the work function, as will be introduced later, results from the time dependent reorganization of the dipoles on the surface.

The static work function change can be determined utilizing TPPE at zero time delay, $\Delta t = 0$, where the pump and the probe pulse overlap temporally, and the image state electron has no time to interact with surface adsorbates. Using the energy separation

between the image state peaks in the $\Delta t = 0$ spectra and Equation 2.5, the quantum defect "$a$" can be obtained for the image state series. The quantum defect $a$ is then inserted back into Equation 2.5 to obtain the "true" binding energies of image states. The energy difference between the experimentally measured binding energy and the true binding energy is the static work function change.

Static work function change owing to the adsorption on Ag(111) was measured with TPPE for methanol, deuterated methanol ($CH_3OD$), 1-propanol, 1-butanol, deuterated butanol ($C_4H_9OD$), and 1-pentanol. Previous measurements of work function change due to linear chain alcohol molecules adsorption were performed by Gellman and coworkers on a Ag(100) surface [60]. They measured the work function change with a Kelvin probe during the temperature programmed desorption of the alcohol molecules from the Ag(100) surface. The experimentally measured static work function change on a Ag(111) surface with TPPE is listed in Table 4.1 along with work function change on Ag(100) measured by Gellman. The subsequent TPPE measurements were conducted with a properly adjusted contact potential difference between the sample and the detector as described in the previous section. Thereafter the measured image state binding energy coincides with the true binding energy at $\Delta t = 0$.

### 4.5.2 Dynamic TPPE Electron Kinetic Energies

Two photon photoemission of alcohol molecules adsorbed onto a metal surface shows a time dependent photoelectron kinetic energy. Figure 4.5(a) shows the time dependent dynamics of peaks observed in TPPE for a typical metal/monolayer alcohol adsorbates interface, in which the TPPE of a monolayer of butanol molecules adsorbed on Ag(111) sur-

Table 4.1: Work function change for alcohol molecules adsorption

| Adsorbates | Ag(111) surface | Ag(110) surface |
|---|---|---|
| Methanol | -1.24 eV | -1.15 eV |
| Propanol | -0.98 eV | -0.98 eV |
| Butanol | -0.86 eV | -0.88 eV |
| Pentanol | -0.83 eV | -0.81 eV |

face. Both the peak intensities and the photoelectron kinetic energies decrease as a function of time delay between the pump and the probe pulse. The time dependent photoelectron kinetic energies observed in Figure 4.5(a) is more clearly depicted in Figure 4.5(b). The time evolution of the TPPE spectra involves complex dynamics of energy relaxation as well as additional appearance of new states.

A TPPE wavelength survey is used to identify the photoemission mechanism of the electron. Several different wavelengths are used for the excitation/photoemission of the electrons while observing the kinetic energy change. Figure 4.6(a) shows the TPPE spectrum of monolayer methanol/Ag(111) photoemitted at $\Delta t = 0$ using several different wavelengths. The $\Delta t = 0$ TPPE is used for wavelength survey to avoid energy relaxation. Two photon photoemission peaks maximum in Figure 4.6(a) is plotted in Figure 4.6(b) versus photoemission photon energies, $h\Delta\nu_2$. The lines represent best fits, which shows the kinetic energy changes by about $1h\nu_2$. The slope of $1h\Delta\nu_2$ indicates that the electrons are photoemitted from fixed energy intermediate states such as image potential states. The two peaks observed in $\Delta t = 0$ TPPE spectrum can be fit to a hydrogenic series of Equation 2.5 as the $n = 1$ and $n = 2$ states with quantum defect of $a = 0.12$, further substantiating their assignment as image potential states.

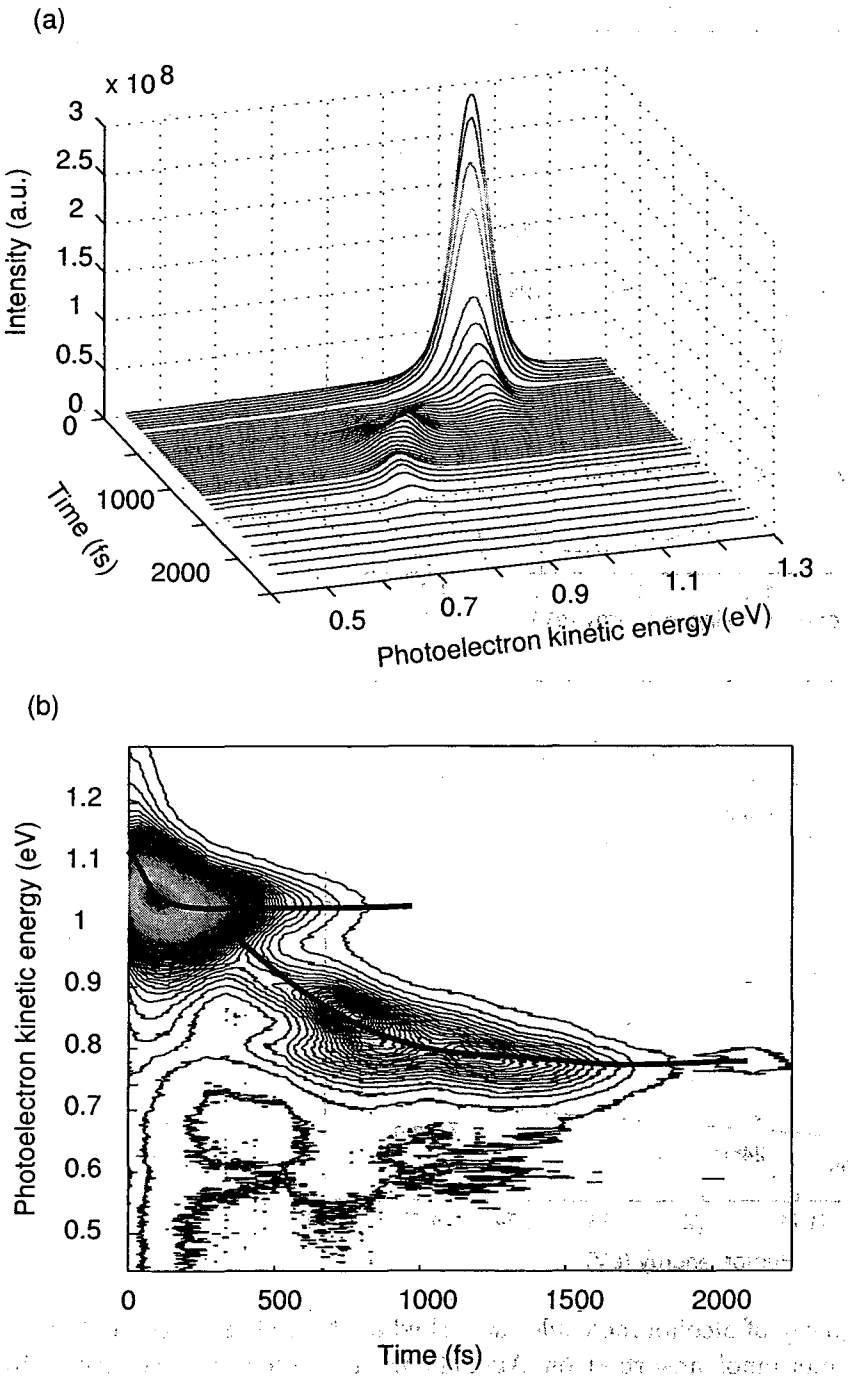


Figure 4.5: Two photon photoemission electron dynamics at a metal/butanol interface. (a) Two photon photoemission population and photoelectron kinetic energy dynamics. (b) Time evolution of photoelectron kinetic energy. Peak shifts are guided by lines.

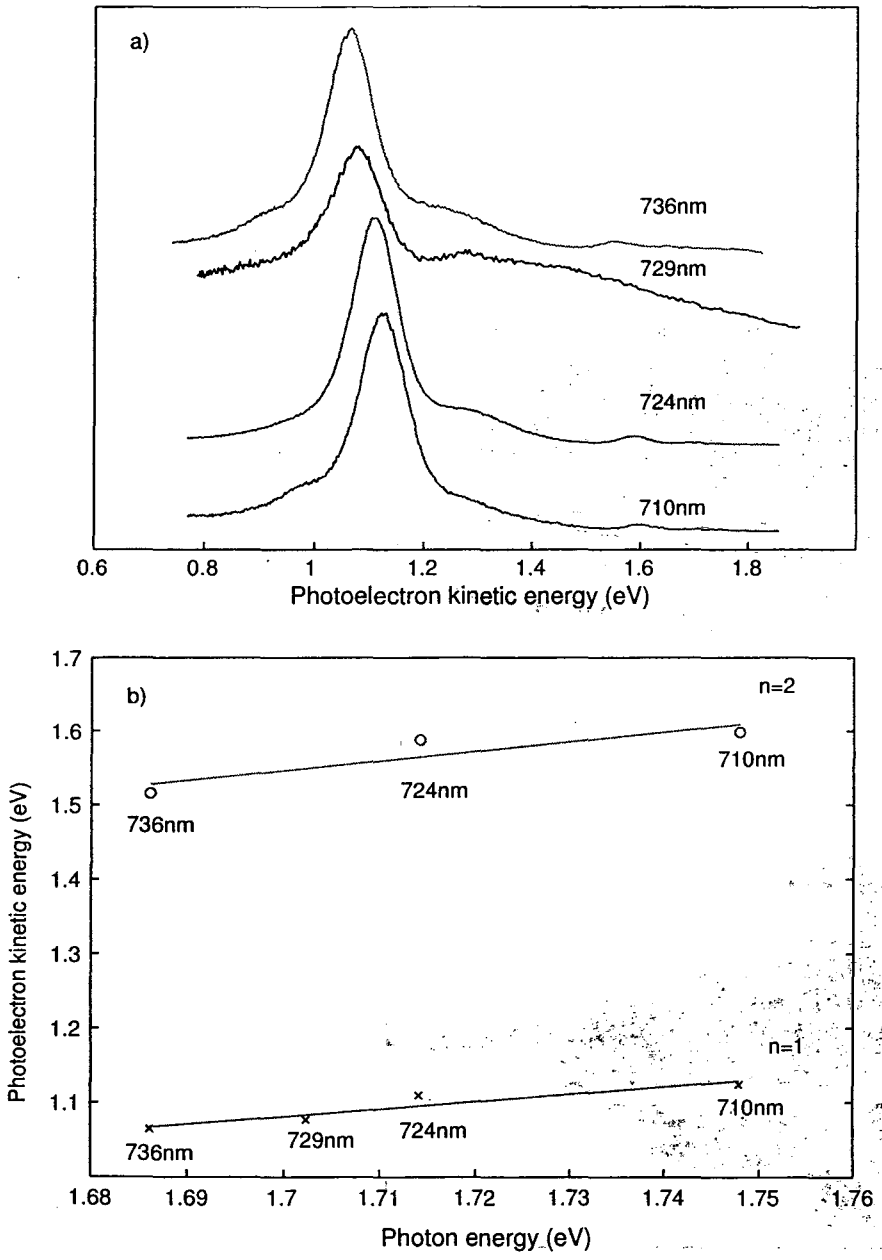


Figure 4.6: Wavelength survey of alcohol molecules adsorbed on Ag(111) surface at $\Delta t = 0$. (a) TPPE of monolayer methanol adsorbed on Ag(111) with different wavelength. (b) TPPE peak maximums as a function of photon energies. The fit (line) shows a slope of $1h\Delta\nu_2$, indicates the electrons are photoemitted from fixed energy intermediate states, such as image potential states.

### 4.5.3 Coverage Dependent Dynamics

Electron dynamics of two different adsorbate surface coverage are studied with TPPE. The adsorbate surface coverage is determined with exposure time and pressure while at constant sample temperature. Figure 4.7 shows the time evolution of TPPE peaks maximum for two different surface coverage of deuterated methanol on Ag(111). At a lower coverage (solid lines), 2.8 langmuire, three peaks are observed: a peak initially at 1.18 eV (circle) that decays in energy exponentially with a time constant of $\tau = 200$ fs, a second peak initially at 0.97 eV (x) that decays exponentially with $\tau = 264$ fs, and a third peak (diamond) initially at 0.77 eV that remains constant in energy. At higher coverage (dotted line), 4.5 lagmuire, only two peaks are observed: one peak initially at 0.96 eV (solid square) and the other peak initially at 0.94 eV (solid triangle) that decay exponentially with $\tau = 463$ fs and 469 fs, respectively.

The population dynamics of these states for each surface coverage is shown in Figure 4.8. The population dynamics in Figure 4.8 has been fit by convolving the instrument function with a single exponential decay. Lines through data points shows the best fit. At low coverage (Figure 4.8(a)), the peak initially at 1.18 eV (circle) has an extremely short lifetime of 52 fs, while the peak initially at 0.97 eV (x) has a lifetime of 1100 fs. Lifetime for the third peak can not be obtained because it is only visible within the first 350 fs. Population dynamics of the 4.5 langmuire deuterated methanol coverage (solid line) and 5 langmuire methanol coverage (dotted line) is shown in Figure 4.8(b) for comparsion. The two deuterated methanol peaks have lifetimes of 1220 fs (solid square) and 1190 fs (solid triangle) while the two methanol peaks have lifetimes of 1550 fs (x) and 1440 fs (+).

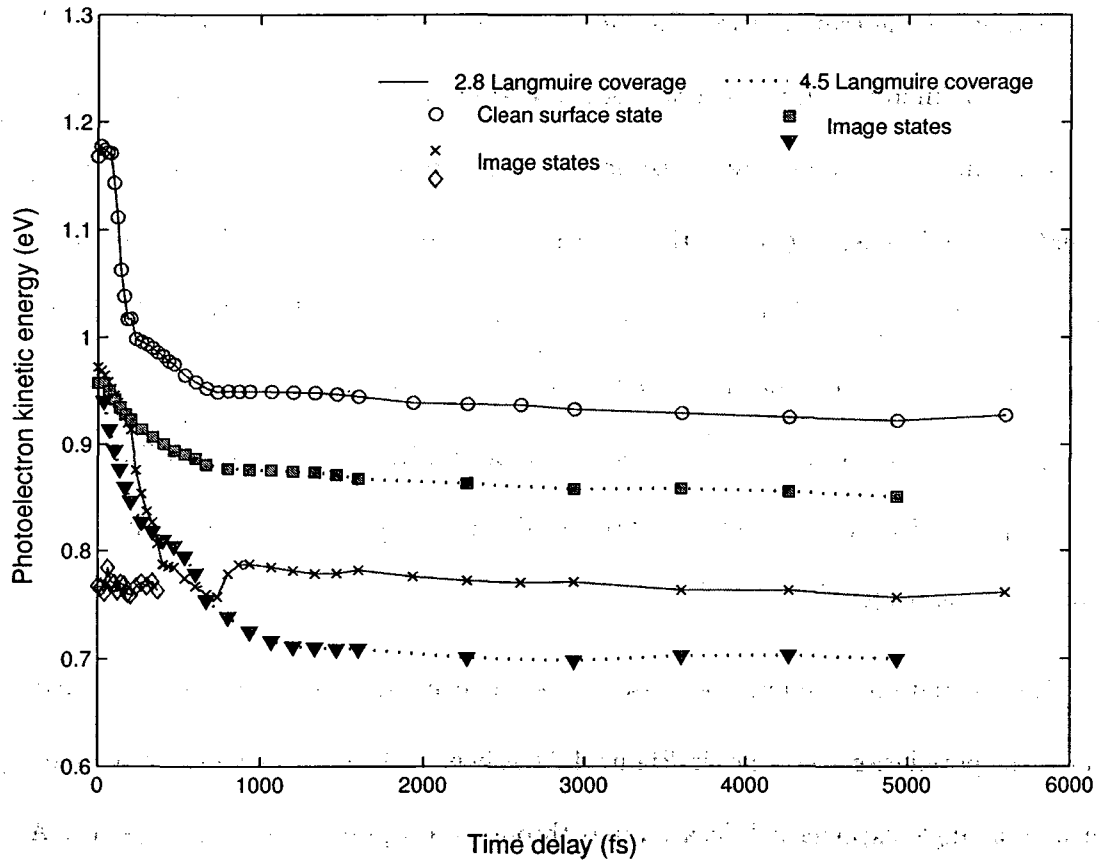


Figure 4.7: Image state photoelectron dynamics at two different surface coverage of deuterated methanol on Ag(111). Photoelectron kinetic energy is plotted against delay time between the pump and the probe pulse. At 2.8 langmuire (in solid line), three peaks are observed (circle, x, and diamond), while at 4.5 langmuire (in dotted line), only two peaks are observed (solid square and solid triangle). Energy relaxation for the two different coverage exhibits similar dynamics, indicating similar molecular reorganization caused the energy reduction.

Lifetimes of $\sim$ 1000 fs for a monolayer coverage indicate that the methanol or deuterated methanol monolayer effectively decouples the image state electron from the metal substrate, shifting the image state electron density partially outside of the adsorbate layer, into the vacuum. The low coverage peak (circle) has a lifetime that is comparable to the clean surface $n = 1$ image state lifetime of 36 fs. This indicates that 2.8 langmuire exposure results in an incomplete surface coverage. Image state with longer lifetime suggests that electron interacts strongly with patches of deuterated methanol, while the peak with short lifetime implies that electron interacts strongly with patches of clean Ag(111) surface. At a complete monolayer coverage of 4.5 langmuire, electron interacts only with the adsorbate. Although the two peaks at low coverage have different lifetimes, energy relaxation of these two states have similar time constants of $\tau \sim 300$ fs, indicating similar molecular motion that caused the energy stabilization.

### 4.5.4 Alcohol Molecule Dependent Kinetic Energies Dynamics

A series of straight chain alcohol molecules are used to study the electron dynamics upon photo injection from bulk metal to a metal/alcohol monolayer interface. The magnitudes and the dynamics of the TPPE kinetic energy relaxation are used for comparison in attempts to understand electron-adsorbates interactions.

#### Methanol

Methanol ($CH_3OH$) is the smallest alcohol molecules studied with TPPE. Monolayer methanol adsorbed on Ag(111) at about 120 K and forms an ordered monolayer (at 5 langmuire exposure) that can be observed with LEED (Figure 3.7(b)). Dipole moment

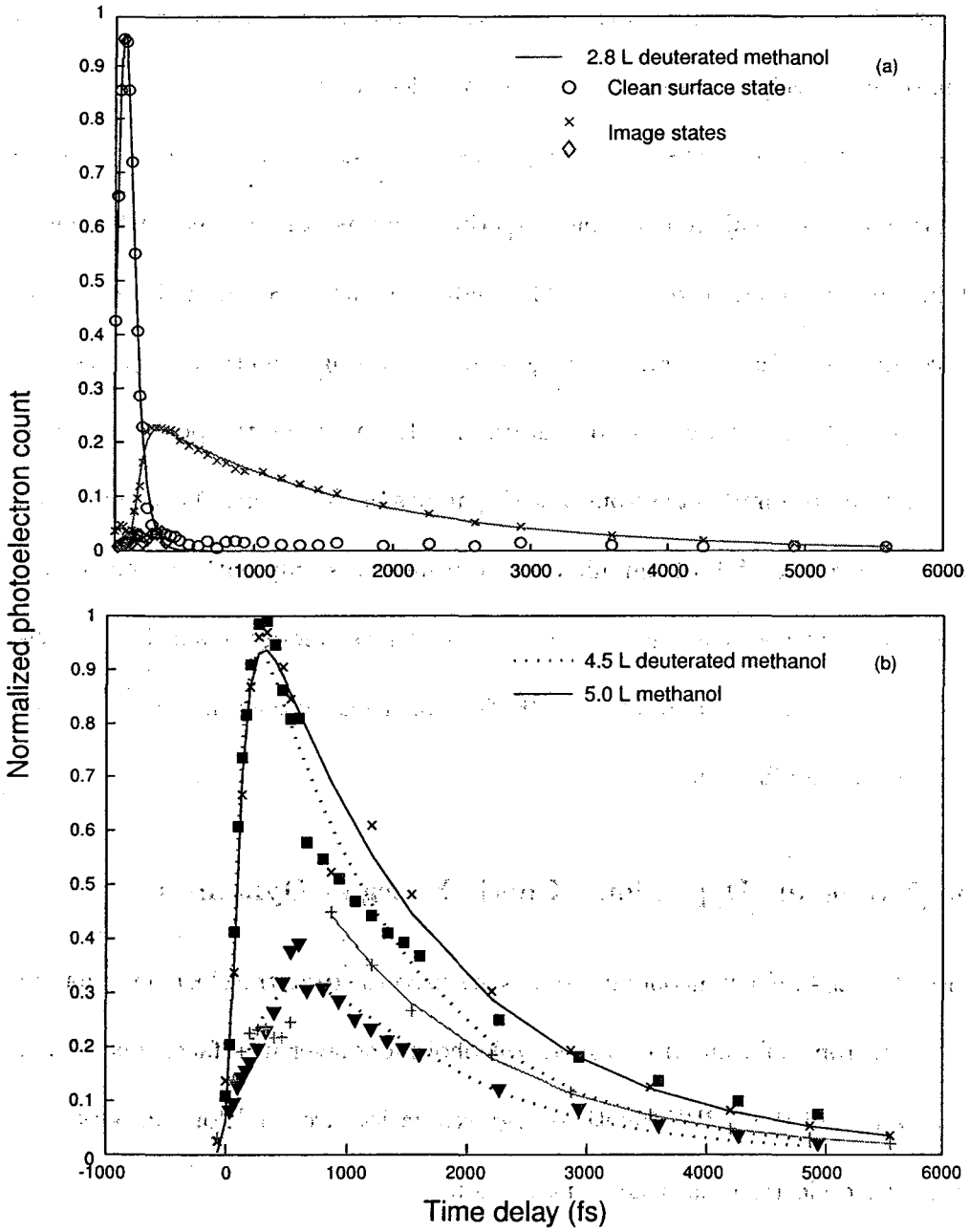


Figure 4.8: Normalized photoelectron counts plotted as a function of delay time. Lines represent the best fit. (a) At 2.8 langmuire deuterated methanol, incomplete surface coverage results in the appearance of a clean surface image state (circle) that has a lifetime of 52 fs. (b) TPPE population dynamics for the 4.5 langmuire deuterated methanol (dotted line) and 5 langmuire methanol (solid line) on Ag(111). Similar population dynamics are observed for these two systems. The deuterated methanol peaks have lifetimes of 1220 fs (solid square) and 1190 fs (solid triangle), while the two methanol peaks have lifetimes of 1550 fs (x) and 1440 fs (+), respectively.

of 1.70 Debye for methanol is the strongest dipole compared to other straight chain alcohol molecules [120]. The kinetic energies of the $n = 1$ image state electrons as a function of time delay between the pump and the probe pulses are shown in Figure 4.9. At $\Delta t = 0$ only one $n = 1$ image state can be seen. Within 200 fs, a second $n = 1$ image state appears in the TPPE spectra. The kinetic energies of both states are observed to decrease as a function of $\Delta t$. The kinetic energy of the initial $n = 1$ image state shifts by $0.106 \pm 0.010$ eV and the kinetic energy of the other $n = 1$ image state shifts by $0.237 \pm 0.010$ eV. The maximum change in the kinetic energy is defined as the solvation energy. The $n = 2$ state is not seen in the spectra due to low signal to noise ratio. Population dynamics of these two states is displayed in Figure 4.8. The two $n = 1$ image states have lifetimes of 1550 fs (circle) and 1440 fs (x).

**Propanol**

Propanol ($CH_3CH_2CH_2OH$), with an dipole moment of 1.68 Debye, adsorbs on Ag(111) surface at about 140 K [120]. Adsorption of 1 langmuire of propanol at 160 K equals to one monolayer. LEED pattern of ordered propanol monolayer is indicated in Figure 3.7(c). The time evolution of kinetic energy of the monolayer propanol image electrons photoemitted with $h\nu_2 = 682$ nm light are shown in Figure 4.10. For propanol/Ag(111), image state $n = 1$, $n = 2$, and $n = 3$ are observed in the TPPE spectra. At $\Delta t \leq 200$ fs, only one set of image state series with a quantum defect of $a = 0.12$ appears in the spectra. All three image states change kinetic energies in unison, maintaining a constant quantum defect. Between $\Delta t = 200$ fs to $\Delta t = 1600$ fs, an additional image state series appears in the spectra. The new image state series also shifts in kinetic energies while maintaining a

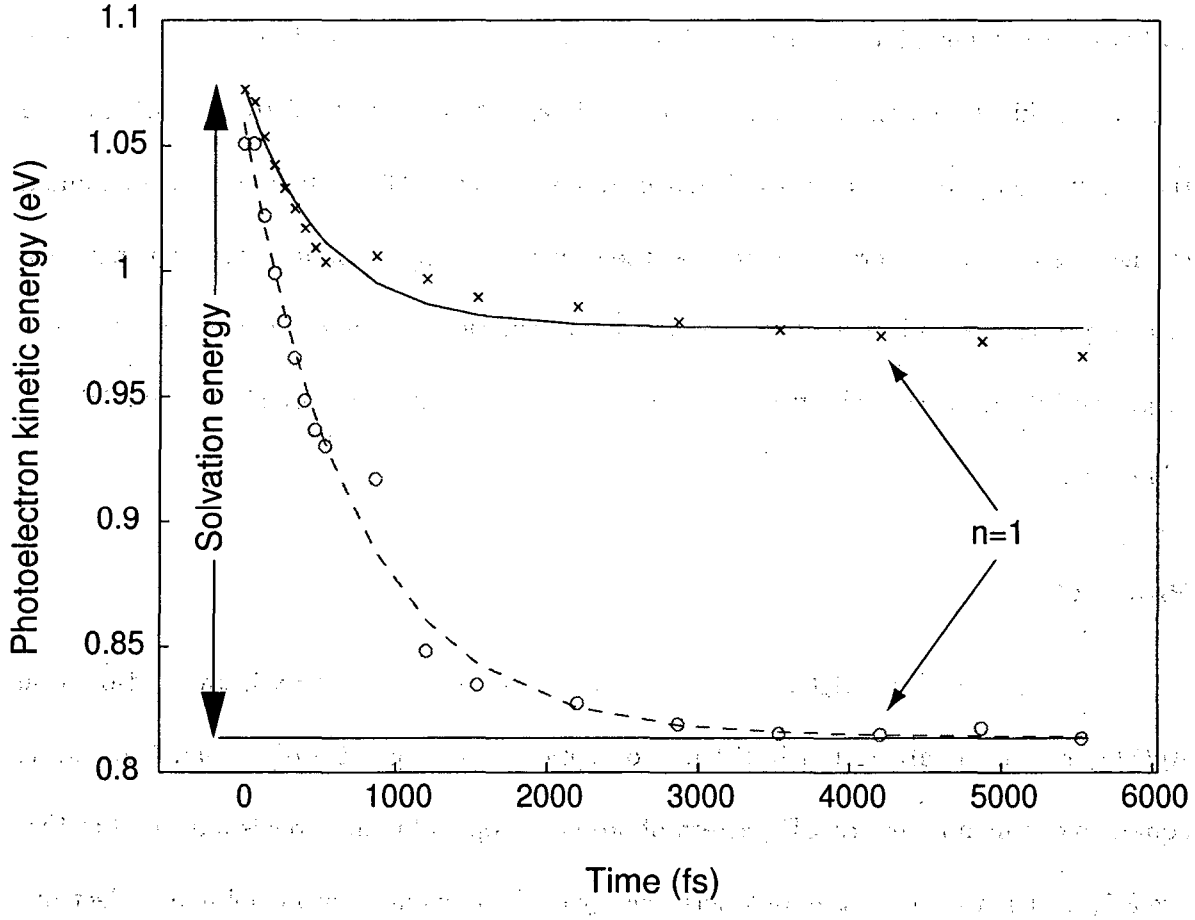


Figure 4.9: Image state electron kinetic energies as a function of time delay between the pump and probe pulses at a monolayer of methanol adsorbed on Ag(111). Two $n = 1$ image state are observed. Energy relaxation of photoelectrons can fit to exponential decay. Maximum change in photoelectron kinetic energies is defined as the solvation energy.

constant quantum defect of $a = 0.12$. The initial image state series (circle) shifts in energies exponentially with $\tau = 302$ fs. The second image state series (x) has an exponential decay time constant of 510 fs. The overall solvation energy is $0.251 \pm 0.010$ eV.

### Butanol

Monolayer butanol ($CH_3CH_2CH_2CH_2OH$) adsorbed on Ag(111) at 160 K with about 1 langmuire exposure. The work function change owing to adsorption of a monolayer is 0.86 eV. Straight chain butanol has a molecular dipole of 1.66 Debye [120]. Figure 4.11 shows both the $n = 1$ and $n = 2$ image state electron kinetic energy dynamics. Butanol photoelectrons kinetic energy dynamics present a strong resemblance to those of a monolayer of methanol and propanol. Multiple image state series relax simultaneously with a constant $a = 1.11$ quantum defect. The first image state series (circle) relax with $\tau = 260$ fs. Both energies of the second $n = 1$ and $n = 2$ image state series (x) decrease exponentially with $\tau = 530$ fs. Total change in energy for butanol is $0.254 \pm 0.010$ eV.

### Pentanol

Straight chain pentanol ($CH_3CH_2CH_2CH_2CH_2OH$) is the longest alcohol molecules studied with TPPE in this dissertation. Pentanol has a molecular dipole of 1.64 Debye [120]. As the alcohol molecules increase in size, the adsorption temperature of the molecule also increases. Pentanol adsorbed on the Ag(111) surface at about 180 K. The work function change due to alcohol molecule adsorption also decreases with the increase in alcohol molecule size. Monolayer pentanol lowers the Ag(111) work function by 0.83 eV. Photoelectron kinetic energy relaxation for pentanol adsorbed on Ag(111) is shown in Figure 4.12.

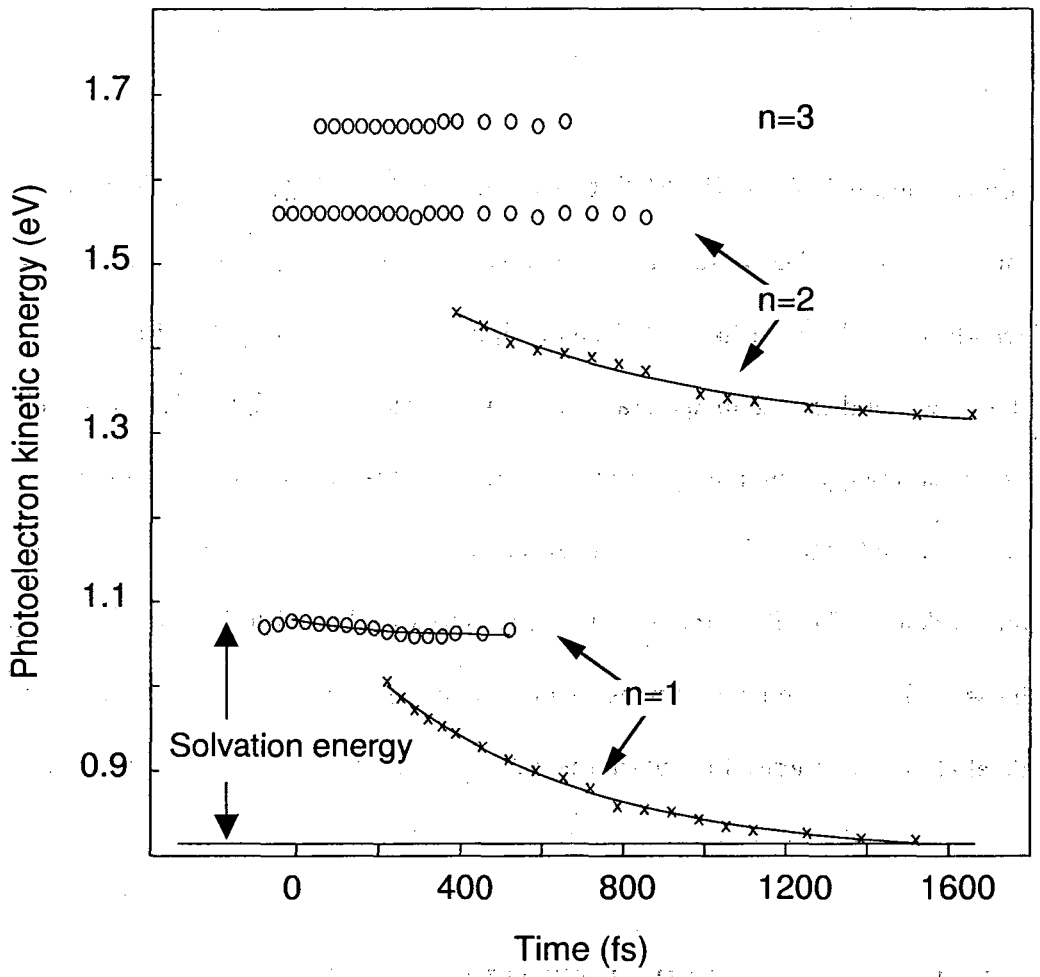


Figure 4.10: TPPE kinetic energy dynamics at monolayer of propanol adsorbed on Ag(111). Multiple image state series appear in the spectra. Image states within each image state series change kinetic energies in unison, maintaining a constant quantum defect of $a = 0.12$. Initial set of image state series (circle) decays in energy exponentially with a time constant of 302 fs. The second image state series (x) has an exponential decay time constant of 510 fs.

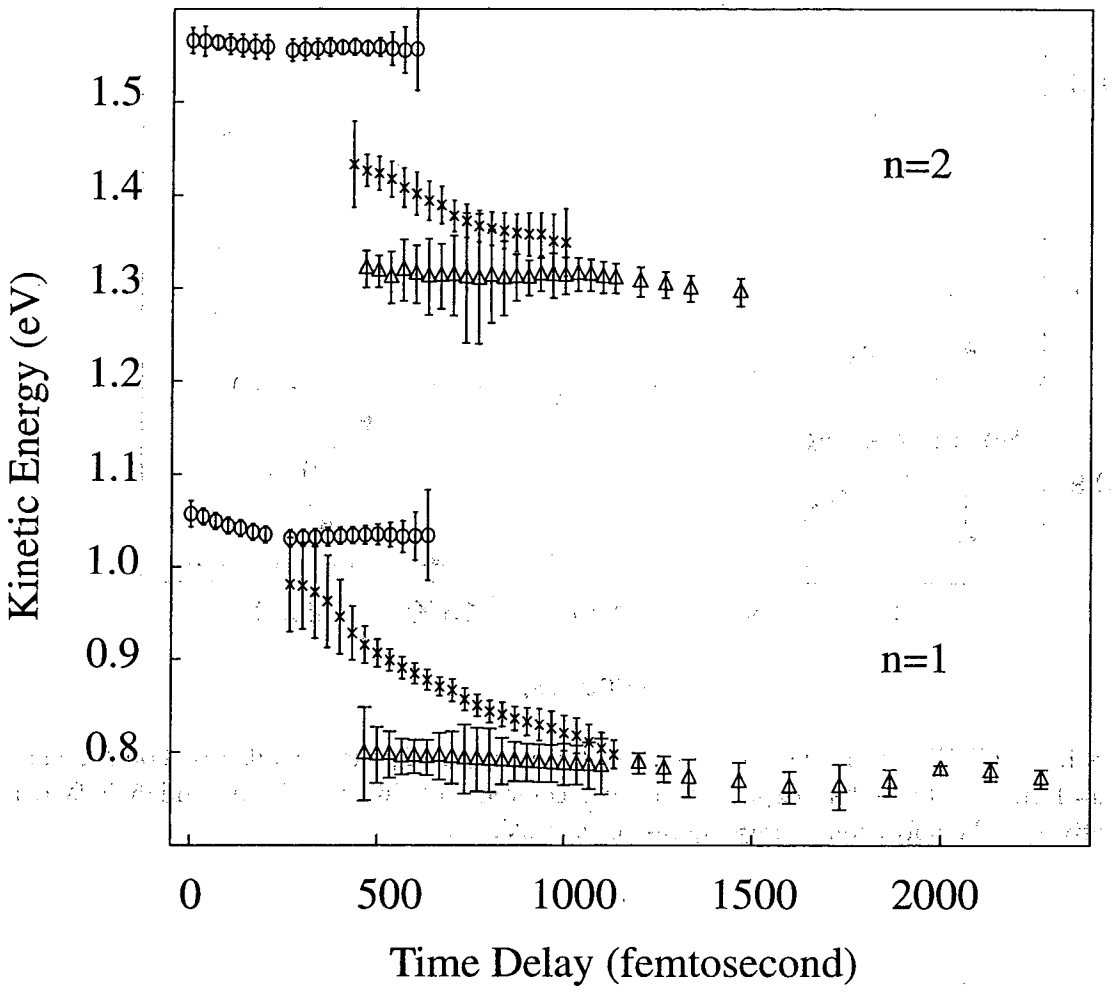


Figure 4.11: TPPE kinetic energy dynamics at monolayer of butanol adsorbed on Ag(111). The error bars indicate 95% confidence intervals. All three hydrogenic series have a quantum defect of $a = 1.11$. The first (circle) and second (x) image state series have a exponential decay time constant of 260 and 530 fs, respectively. The third series appears to have a constant energy. The total solvation energy equals to 0.25 eV.

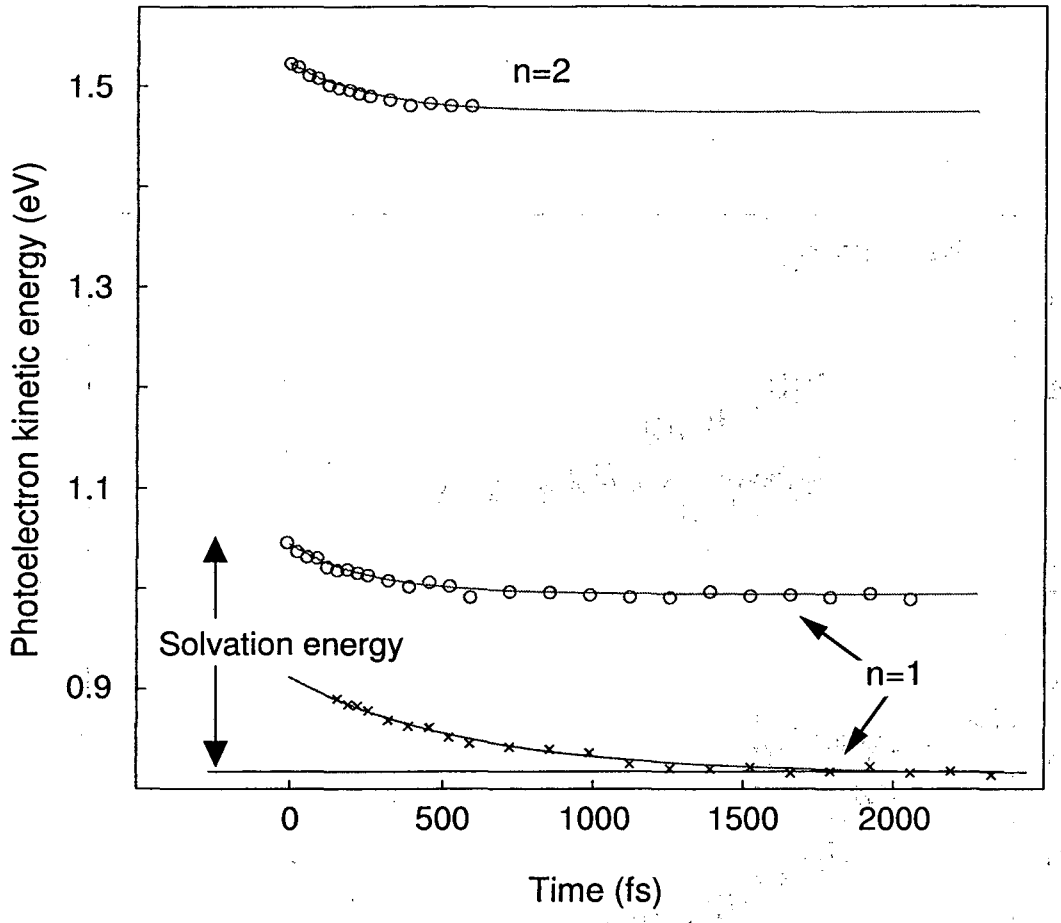


Figure 4.12: TPPE kinetic energy dynamics at monolayer of pentanol adsorbed on Ag(111). The n=1 image states has exponential time constant of 269 fs (circle) and 545 fs (x), respectively. The solvation energy equals to 0.23 eV.

The dynamics of energy relaxation for pentanol shows a strong resemblance to other alcohol molecules. The initial image state series shift in energy exponentially with $\tau = 269$ fs and a quantum defect of $a = 0.11$. The second $n = 1$ image state relaxes exponentially with $\tau = 545$ fs. No $n = 2$ image state is observed for the second image state series. Total solvation energy for pentanol is $0.231 \pm 0.010$ eV.

### 4.5.5 Deuterated Alcohol Molecules

Two photon photoemission electron dynamics at deuterate methanol ($CH_3OD$)/Ag(111) and deuterated butanol ($CH_3CH_2CH_2CH_2OD$)/Ag(111) interfaces are studied to compare with those of non-deuterated alcohol/Ag(111) interfaces. In general there is no discernable difference between the deuterated species and the non-deuterated species. Figure 4.13 shows the image state electron kinetic energy dynamics for both methanol and deuterated methanol. Image state electron relaxes with similar time scale and energy for both alcohol species. Population dynamics for both alcohol species are shown in Figure 4.8(b), where both deuterated methanol and methanol have a lifetime of about $\sim$ 1500 fs. Similar electron dynamics are also observed for butanol and deuterated butanol.

### 4.5.6 Temperature Dependent Solvation Dynamics

The temperature dependence of the solvation dynamics is investigated for a monolayer of butanol on Ag(111). TPPE energy relaxation dynamics are taken at four different sample temperatures: 170 K, 130 K, 100 K, and 50 K. Initial butanol layer is deposited at 180 K prior to lowering the sample temperature. Figure 4.14 shows the time evolutions of photoelectron kinetic energy at four temperatures. At 100 K and 50 K, TPPE signals can be observed until $\Delta t \sim 1200$ fs. For the 170 K and 130 K measurements, TPPE peaks can only be seen within 600 fs time delay owing to fast signal decaying. Lowering the sample temperature improves the signal to noise ratio, thus allowing the observation of the TPPE signal at longer time delay. Both n=1 and n=2 image states are observed in the TPPE spec-

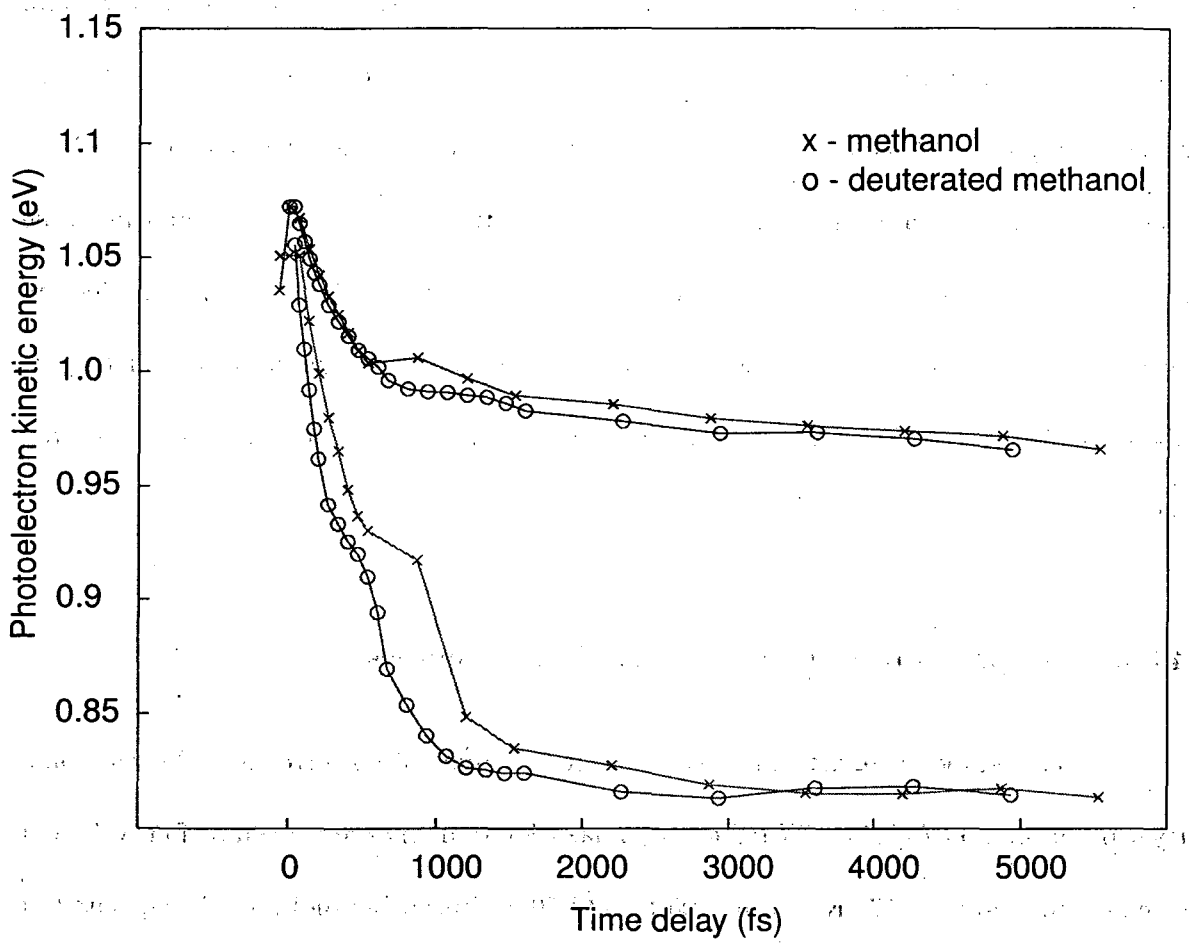


Figure 4.13: Electron solvation dynamics for methanol and deuterated methanol adsorbed on Ag(111). Similar solvation energy and dynamics were observed for methanol and deuterated methanol.

tra. Lowering the sample temperature shifts the binding energy of the image state closer to the Fermi level, thus lowering the photoelectron kinetic energy. Similar shifts in the peak position of the image states have been observed on clean Ag(111) [58], Cu(100) [121], and Cu(111) [122]. However, lowering the sample temperature do not change the relaxation dynamics of image states. Figure 4.15 depicts a close up view of the n=1 and n=2 image state energy dynamics. At these four temperatures, the n=1 image state relaxation can be fit to a single exponential decay with a $\tau \sim 205 \pm 40$ fs and the n=2 image state with a $\tau \sim 180 \pm 40$ fs, showing that the solvation dynamics and the solvation process is identical at all four temperatures. Both the n=1 and n=2 image state shift in unison and relax by about 0.03 eV from 0 to 500 fs, which is similar to the energy shift observed in other alcohol solvation.

### 4.5.7 Discussion

Two photon photoemission for all of the alcohol/Ag(111) interfaces shows image state electron energy relaxation. An important result in these energy relaxations is that they always shift in unison, while both the $n = 1$ and $n = 2$ (sometimes $n = 3$) image state shift in energies. While the image state series decreases in energy, the quantum defect "$a$" that characterizes the series remains constant along with the binding energy of each image state. To maintain the same image state electrons binding energies, the energy level to which image states are converging must be decreasing in energy as well. Equation 2.5 in Section 2.2 states that the image state series converges to the vacuum level, $E_{vac}$, of the system. Further examination on the definition of work function in Section 4.2 shows that for a finite size metal, the vacuum level only exists at a distance very far away from the surface.

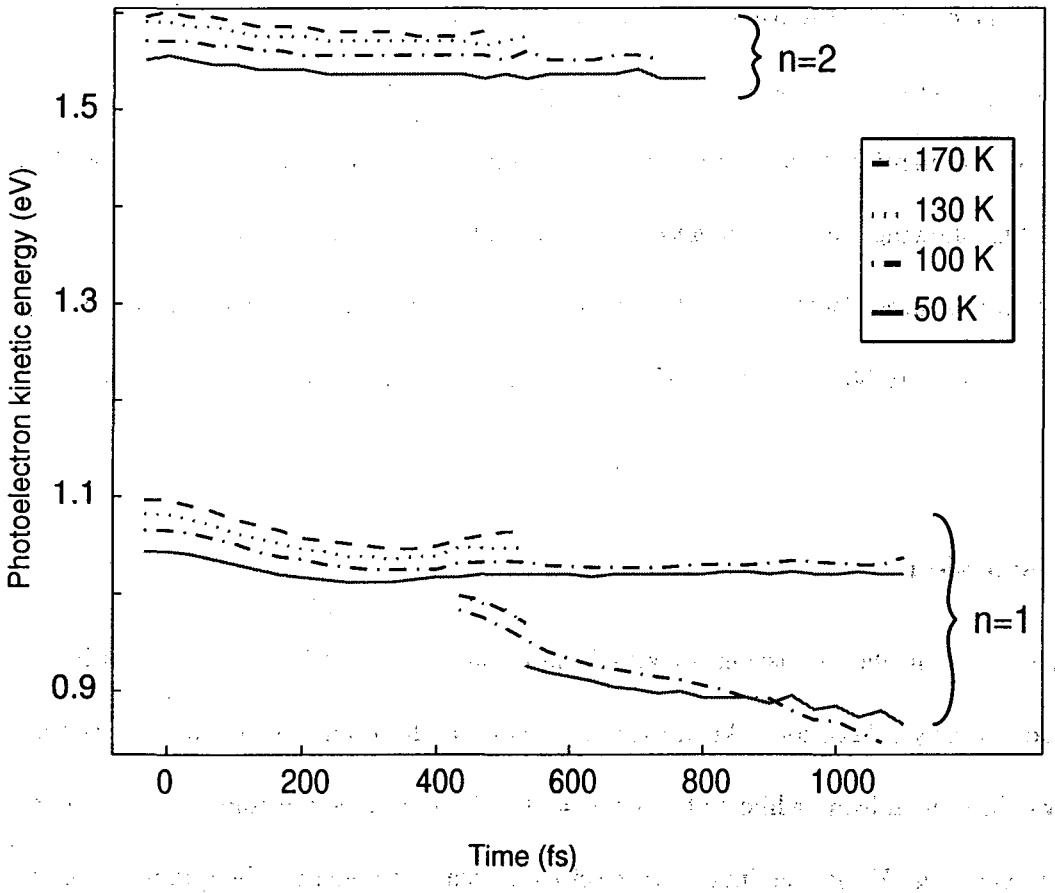


Figure 4.14: Electron solvation dynamics for butanol on Ag(111) from 170 K to 50 K. Both $n = 1$ and $n = 2$ image state are observed in the TPPE spectra. Lowering the sample temperature results in a constant energy shift for each image state series.

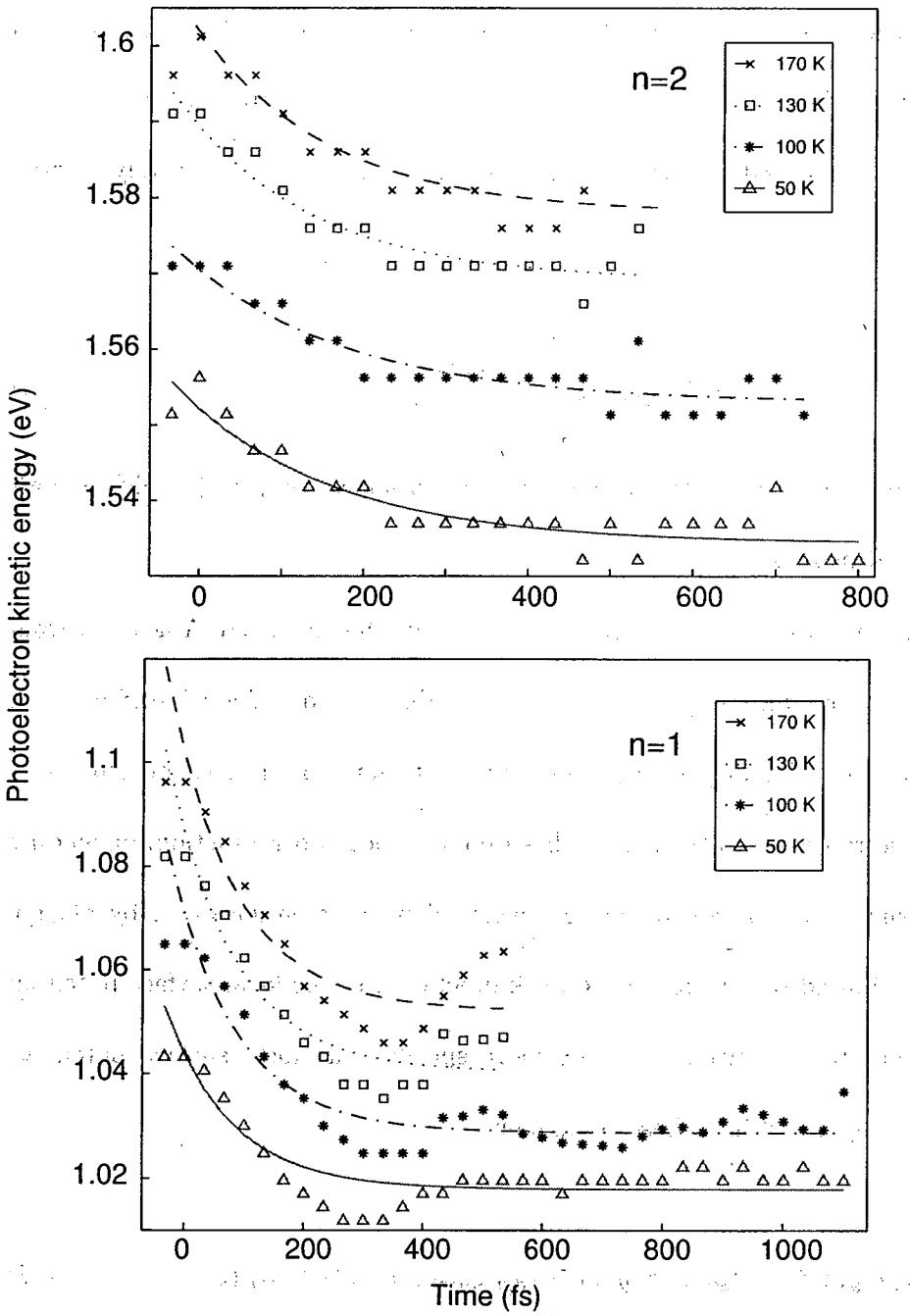


Figure 4.15: Image states solvation dynamics at various temperature. At each temperature, the $n = 1$ and $n = 2$ relax energy exponentially with a time constant of 205 and 180 fs, respectively.

For the first few image states that reside at a few Ångstrom from the surface, the image states converge to a local surface potential, $\phi_{loc}$, which reflects the local surface electron density. As indicated in the image state dynamics, the local surface potential to which the image states converge is decreasing in energy. Equation 2.5 can be more accurately written as

$$E = \phi_{loc}(x, y, z, t) - \frac{0.85eV}{(n+a)^2} \tag{4.4}$$

where the energies are referenced to the local surface potential $\phi_{loc}(x, y, z, t)$, which is both a function of time and position.

Description of work function in Section 4.2 shows that at a few Ångstrom from the surface, the local work function reflects the charge distribution of local surface area. Simultaneous appearance of multiple image potential state series in TPPE spectrum also indicates that an electron close to the surface has different local work function, depending on local surface structures. Energy relaxation observed in electron solvation by alcohol molecules can be attributed to changes in the work function, i.e. the local surface potential $\phi_{loc}(x, y, z, t)$ adjacent to the surface. To be more specific, the local surface potential, $\phi_{loc}(x, y, z, t)$ can be separated into these components:

$$\phi_{loc}(x, y, z, t) = \phi_{static}(x, y, z) + \phi_{dynamic}(x, y, z, t) + \phi_{IP}(z) \tag{4.5}$$

where $\phi_{IP}(z)$ is the image potential, $\phi_{static}(x, y, z)$ is the surface potential due to the initial adsorption of the polar adsorbate, and $\phi_{dynamic}(x, y, z, t)$ is the dynamical change in the local surface potential observed in TPPE. The simultaneous appearance of multiple image

state series, and the dynamical change in local surface potential result from time dependent variation of the local work function caused by the adsorbate reorganization on the surface. In this case, the reorganization is the rotation of the alcohol molecular dipole to solvate the image state electron.

An image state electron that resides at only a few Ångstroms outside the surface significantly perturbs the equilibrium structure of the alcohol layer. The alcohol molecules respond to the perturbation by rotating the positive end of their molecular dipoles towards the electron, i.e. by "solvating" it. This reorientation results in an increased projection of the molecular dipole along the surface normal from the initial adsorption geometry. Dipole rotation also results in a reduction of the surface potential, $\phi_{dynamic}(x, y, z, t)$, to which the image state progression converges. The difference between the static surface potential, $\phi_{static}(x, y, z)$, and the dynamic surface potential, $\phi_{dynamic}(x, y, z, t)$ is the solvation energy. Figure 4.16 schematically illustrates the solvation process at an adsorbate/metal interface. Initial adsorption of alcohol molecules lowers the work function of the metal by lowering the surface potential component of the work function, $\Phi$. At $\Delta t = 0$, the image potential states converge to $\phi_{static}(x, y, z)$. As molecules rotate its dipole to solvate the image state electron, the local surface potential and local work function are also lowered. By aligning the dipoles toward vacuum, the positive charge accumulation on the vacuum side of the surface increases, thus lowering the work function.

Two photon photoemission studies of electron solvation by alcohol molecules indicate that the solvation time scales and solvation energies are relatively similar from methanol to pentanol. The maximum solvation energy for these alcohols is $\sim 2.5$ eV, and the longest

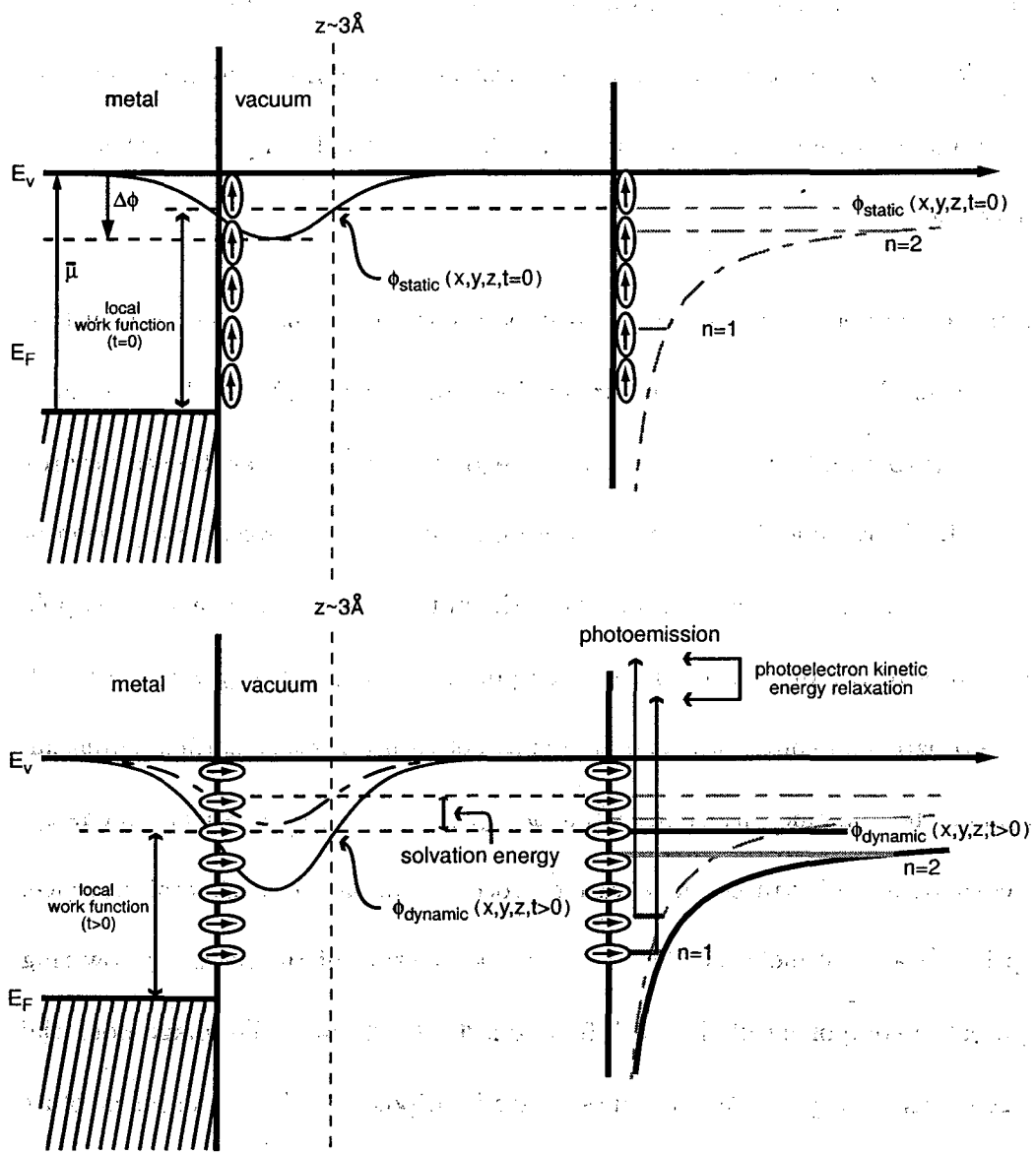


Figure 4.16: Schematic description of local work function and local work function change due to dipole solvation. At $\Delta t = 0$, the dipoles are aligned parallel to the surface. Local work function experienced by image state electrons equals to $\phi_{static} - E_f$. Surface potential, $\phi_{static}$, results from the initial adsorption of the polar molecules. As the polar molecules rotate to solvate the electron, the surface potential and the image state series decrease in energy. The new surface potential energy $\phi_{dynamic}$ arise due to the rotation of the dipole patch. Changes in the local work function (or in the surface potential) is the electron stabilization energy, i.e. solvation energy. The kinetic energy of the electron is measured with respect to a fixed vacuum level, $E_v$. Thus, energy relaxation in image state electron is the solvation energy.

solvation energy relaxation is exponential with time constant of $\sim$ 500 fs. The same solvation energy and relaxation time scale suggest that the solvation motion is similar for all species of straight chain alcohols. In this case, the solvation motion is the rotational motion of the O-H group on the alcohol that points the O-H bond toward the electron. Computer simulation of electron solvated by methanol shows that at equilibrium, the electron is localized within a solvent shell of methanol with the O-H bond of each methanol directed toward the electron [108]. Analysis of specific solvent modes in the relaxation of an excess electron in liquid methanol by Rossky and coworkers shows that the O-H bond motion is the fastest solvent response compared to other methanol rotational motions [110]. In their nonadiabatic molecular dynamics simulation of solvated electron in methanol, Rossky and coworkers attributed the fast adiabatic response of the solvent to the observed fast exponential energy relaxation on the time scale of about 500 fs [109]. This is comparable to the longest solvation time observed in TPPE electron solvation. Pump-probe spectroscopy of the equilibrated solvated electron in liquid alcohols by Barbara and coworkers also observed a fast spectra evolution of $\sim$ 500 fs [95]. In the solvation simulation, Rossky observed a Gaussian relaxation that is on the time scale of 10-30 fs, which they attributed to the ultrafast inertia part of the solvent response.

Two photon photoemission temperature dependent studies have shown temperature independent solvation dynamics. This result excludes the possibility of diffusive solvation mechanism. The diffusive solvation motion scales with the solvent viscosity, which would be slow for a solvent at a glassy or crystalline state of $\sim$ 100 K [13, 96, 123, 124]. If the diffusive solvation can be observed, the solvation time should scale with the temper-

ature, since viscosity is proportional to the temperature. The rotational motion, on the other hand, varies with the dipole density on the surface, which is comparable between 300 to 80 K. The temperature independent solvation dynamics indicates a rotational solvation mechanism as well.

Partial charges of straight chain alcohol calculated with density functional theory are shown in Table 4.2. The O-H group is the strongest dipole on all of the alcohol molecules examined. While the alcohol molecule increases in size, the dipole moment on the O-H group remains mostly unchanged. The ability of the O-H group to stabilize excess electron remains unchanged for different alcohol molecules. This agrees well with the experimental finding of constant solvation energy and solvation dynamics for all the straight chain alcohol molecules.

Within our experimental time resolution, no difference in solvation dynamics is observed for image state electron solvated by deuterated methanol or methanol, as well as by deuterated butanol and butanol. This is consistent with experiments performed by Yoshihara and coworkers on Coumarin 102 solvation by deuterated methanol and normal methanol [125]. Within the first 500 fs, no difference in solvation dynamics is observed for these two solvents. The isotope effect only appears in the second and third solvation time constant of about 2 picosecond and 15 picosecond, respectively. Owing to the lack of time resolution, they did not observe the ultrafast solvent response that was on the order of $\sim 50$ fs.

Multiple image potential state series are observed in all of the alcohol solvent experiments. Except for methanol, the appearance of the second image state series oc-

Table 4.2: Alcohol molecules charge density

| Methanol | | Propanol | | Butanol | | Pentanol | |
|---|---|---|---|---|---|---|---|
| **H** | **0.3375** | **H** | **0.3042** | **H** | **0.3042** | **H** | **0.3041** |
| **O** | **-0.6516** | **O** | **-0.5402** | **O** | **-0.5410** | **O** | **-0.5410** |
| C | 0.0064 | C | 0.0716 | C | 0.0650 | C | 0.0646 |
| H | 0.1237 | H | 0.0723 | H | 0.0726 | H | 0.0727 |
| H | 0.0920 | H | 0.0723 | H | 0.0726 | H | 0.0727 |
| H | 0.0920 | C | -0.1772 | C | -0.1723 | C | -0.1795 |
| | | H | 0.1054 | H | 0.1015 | H | 0.1018 |
| | | H | 0.1054 | H | 0.1015 | H | 0.1018 |
| | | C | -0.3209 | C | -0.1767 | C | -0.1708 |
| | | H | 0.1056 | H | 0.0901 | H | 0.0860 |
| | | H | 0.1008 | H | 0.0901 | H | 0.0860 |
| | | H | 0.1008 | C | -0.3092 | C | -0.1667 |
| | | | | H | 0.0978 | H | 0.0916 |
| | | | | H | 0.1020 | H | 0.0916 |
| | | | | H | 0.1020 | C | -0.3119 |
| | | | | | | H | 0.0987 |
| | | | | | | H | 0.0992 |
| | | | | | | H | 0.0992 |

curs at $\sim$ 400 fs. Initially, a single observed image state series indicates that the local electrostatic environment is uniform over the entire surface sampled by the electron. The appearance of multiple image state series signifies surface inhomogeneities that cause variation in $\phi_{loc}(x, y, z, t)$, and different solvation pathways characterized by different values of the surface dipole moment. Surface inhomogeneities cause variations in surface potential, which in turn results in areas with different local work functions. Smaller energy relaxation observed for some of the image state series might be caused by incomplete rotation of the O-H bond to solvate the electron.

## 4.6 Dynamical Electron Localization

The process of electron solvation in liquid is often accompanied by localization of the solute. The formation of solvent cage surrounding the initially delocalized electron was observed both in experiments and in computer simulations. Upon the creation of the electron, solvent molecules rearrange and localize the solute. At equilibrium, the solvated electron is localized in a cavity with radius of $\sim$ 3 Å surrounded by a solvent shell of $\sim$ 6 molecules [108]. For solvation in crystalline solvent, the process is less clear. Excess electron in frozen polar solvent is observed to be solvated and localized by the polar solvent, but the order of occurrence is unclear.

Apart from energy relaxation due to solvent rearrangement, electrons are also observed to be dynamically localized by the solvent motion. Dynamical localization of electrons has been observed in all alcohol solvation experiments in this dissertation. Angle-resolved TPPE is used to measure the electron wavefunction parallel to the surface. Delo-

calized electron shows a parabolic dispersion, while the localized electron possesses a flat dispersion. The mass of the electron can be computed from the TPPE dispersion spectra, where a dispersion of 1 is equivalent to a free electron mass. Figure 4.17 shows the plots of localized and delocalized TPPE spectra as well as the $n = 1$ image state dispersion at various time delays for the butanol solvation experiment. Image state electron excited from the bulk metal initially possesses a parabolic dispersion with an effective mass of $\sim 1$. By increasing the delay time, a new localized feature can be seen in the TPPE spectra. The localized peak can only be observed clearly at high angle ($22.4^o$) because the the localized and the delocalized peaks overlap at low angle. At 187 fs, both the localized and delocalized peaks are visible. The amplitude of the delocalized state decreases as $\Delta t$ increases. By $\Delta t = 300$ fs, only the localized state is visible in the TPPE spectra. Similar result have been observed for other alcohol solvation experiments. Initially delocalized electrons are localized within the first 300 fs.

Two different mechanisms have been proposed for the process of electron localization in a frozen polar solvent. One theory suggests that initially delocalized electron samples a large area before it localizes in pre-existing trap sites or defect sites in the medium [66]. The other theory suggests that the strong electrostatic interactions between the electron and surrounding medium induce the formation of trap site and then follows by electron localization in the dynamically formed trap site [73, 78, 79]. These two localization mechanisms can be distinguished by examining the short time dynamics of localization. Figure 4.18 shows the zero time delay TPPE spectrum at different angles for propanol. Solid and dash lines represent the deconvoled localized and delocalized states in TPPE, respectively. As

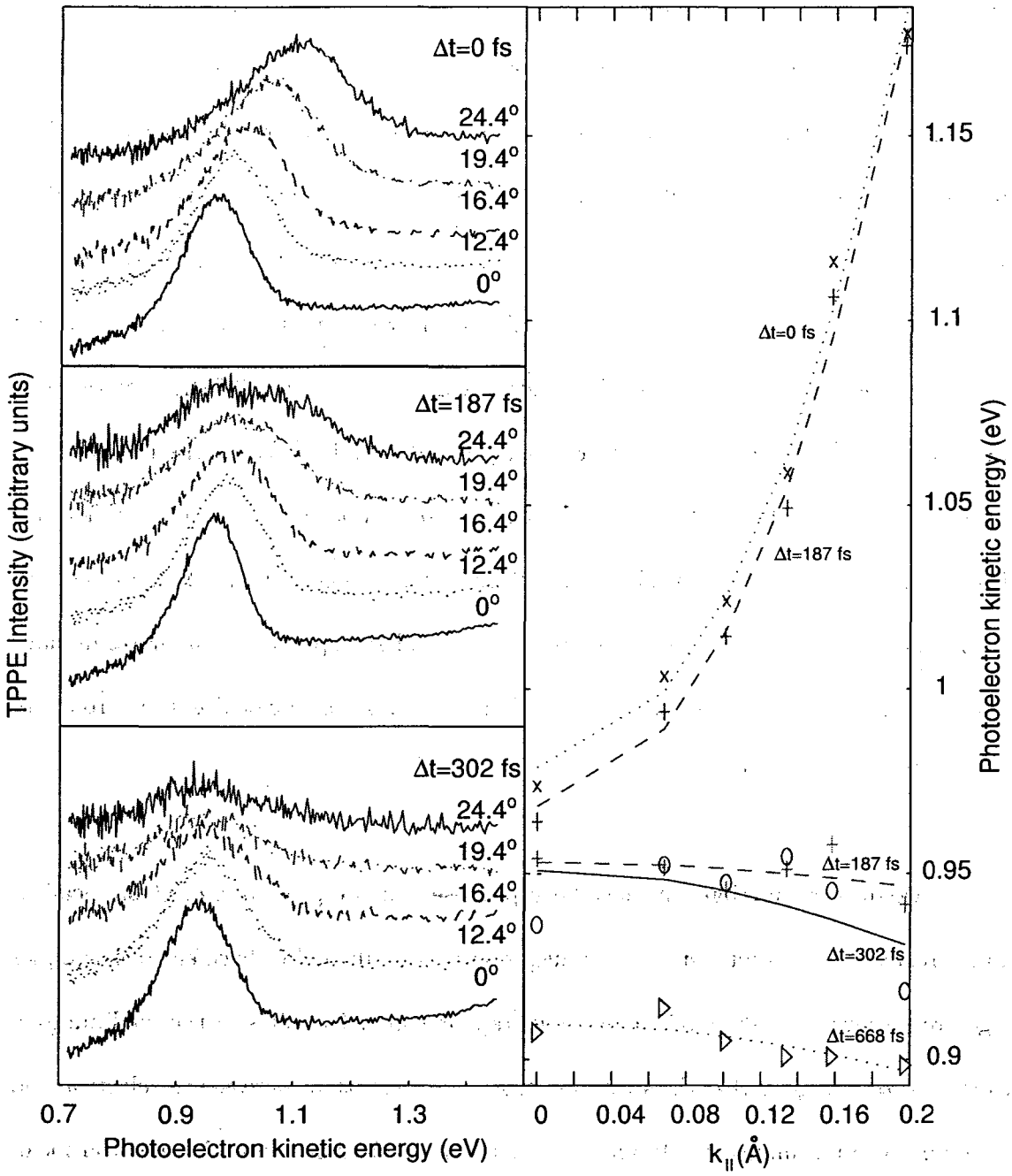


Figure 4.17: Angle-resolved TPPE of monolayer butanol adsorbed on Ag(111) surface. At $\Delta t = 0$ fs, only delocalized image state electron appears in the spectra. As time delay increases, a new localized peak grows in the spectra. At $\Delta t = 187$ fs, both localized and delocalized $n = 1$ image states are observed in the spectra. By $\Delta t = 300$ fs, only localized peak appears. Even after it is localized, the electron continues to decrease in energy owing to solvation by adsorbates.

can be seen in $\Delta t = 0$ spectrum, a small localized peak exists. At $\Delta t = 0$ the solvent does not have time to reorganize, thus the formation of the localized electron must occur due to trapping in pre-existed defect sites. Similar observation has been observed for localization in benzene, where electron was observed to be localized by defects. As $\Delta t$ increases, the localized peak increases in amplitude compared to the delocalized state, which suggests the dynamical localization by solvent motions. The observed localization dynamics is similar to that of the polaron formation where an electron induced lattice distortion cause the electron to localizes at a single lattice site due to favorable energetics [46]. Although it appears that most electrons are localized via dynamical solvent rotation, TPPE results suggest that both localization mechanisms are active in the electron solvation by adsorbed alcohol molecules. Because of the inability to separate the localized and delocalized peak intensities, the precise rate of population transfer between the localized and the delocalized electrons can not be obtained.

Although an idealized image state electron is considered delocalized throughout the entire space at $\Delta t = 0$, in reality, the delocalized electron is confined within some physical boundaries. A purely delocalized electron has infinitesimally small charge density above each molecular dipole, thus can not exert adequate electrostatic force to induce rotation of dipoles. The spatial extend of the delocalization electron is limited by the electron scattering off surface defects, i.e. the coherence length of the electron. The coherent length of the electron can be estimated from the angle dependence of the Lorentzian peak widths ($\Gamma_{\parallel}$) in TPPE [126]. The scattering process parallel to the surface contributes to the Lorentizan widths in parallel momemtum, $p_{\parallel}$, which can be determined with:

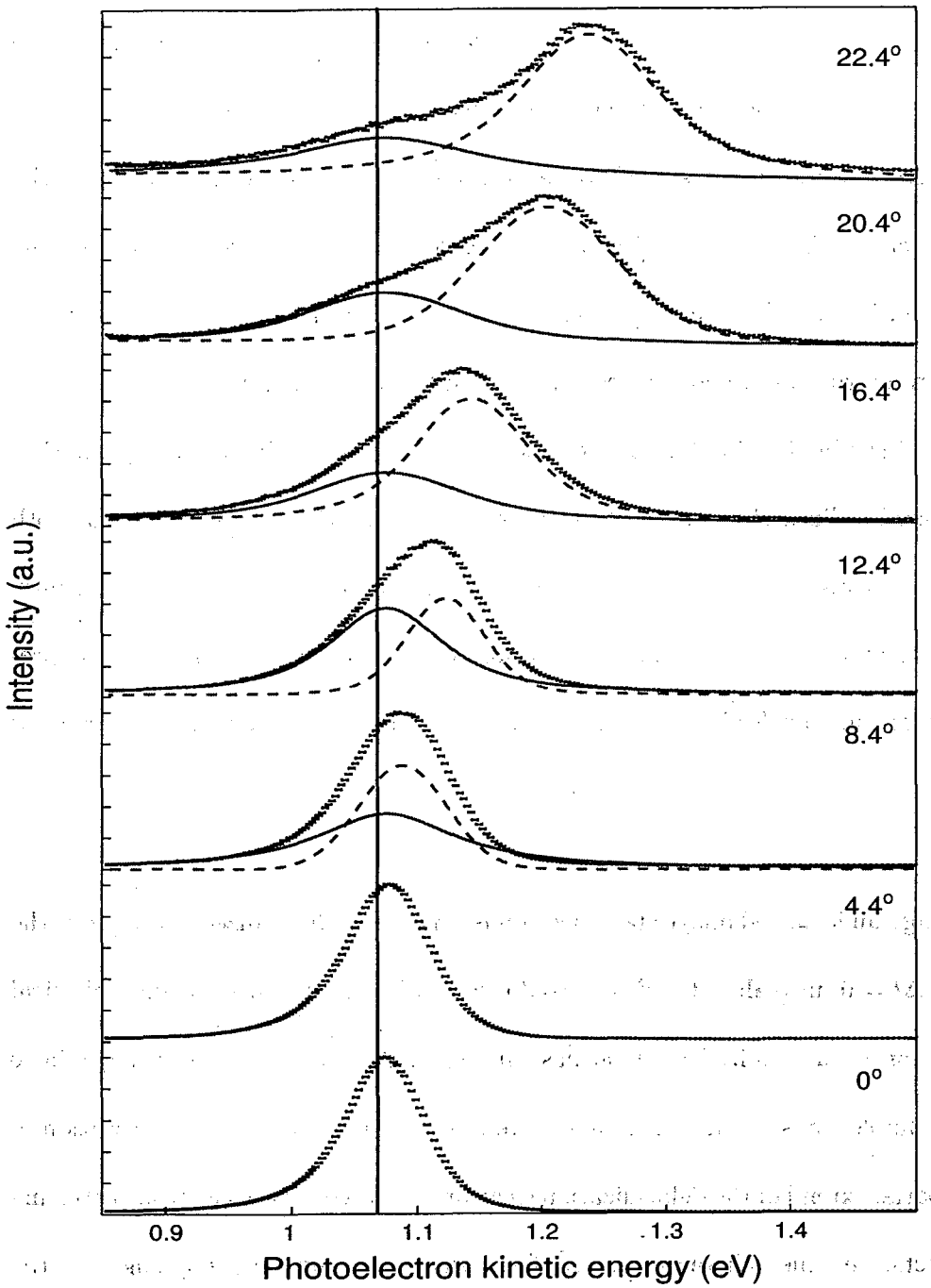


Figure 4.18: Angle-resolved TPPE at $\Delta t = 0$ of monolayer propanol adsorbed on Ag(111) surface for $n = 1$ image state. Solid and dash lines represent the deconvolution of localized and delocalized states, respectively.

$$\Gamma_{\parallel} = \Gamma(p_{\parallel}) - \Gamma(p_{\parallel} = 0) \tag{4.6}$$

where $p_{\parallel}$ is the momentum of the electron parallel to the surface. The Lorentzian peak widths can be used to estimate the coherence length, $\Delta x$, of an electron with the following equation:

$$\Delta x = \frac{p_{\parallel}\hbar}{m^{*}\Gamma_{\parallel}} \tag{4.7}$$

Angle resolved TPPE of propanol/Ag(111) in Figure 4.18 is used to estimate the coherence length. At $p_{\parallel} = 0.2$ Å$^{-1}$ and $\Gamma_{\parallel} = 0.015$ eV, $\Delta x$ is $\sim$ 100 Å. A size of $\sim$ 100 Å corresponds to a few hundred alcohol molecules that have the length of $\sim$ 3.48 Å (methanol) to $\sim$ 9.64 Å (pentanol). The size of the surface patch that solvates the electron can also be estimated from the perspective of thermodynamics. If the energy required for a dipole rotation is on the order of kT, the rotation energy is about 4 meV to 9 meV for experiments that take place between 50 K to 100 K. For a solvation energy of $\sim$0.25 eV, the size of the patch is also on the order of $\sim$ 100 Å.

## 4.7 Electron Solvation by Nitrile

Two dimensional electron solvation by polar molecules has also been observed in nitrile/Ag(111) [126]. Acetonitrile and butyonitrile have been used in the studies of electron solvation. Observation of photoelectron kinetic energy relaxation in both nitriles is also attributed to the changes in the local work function caused by the reorientation of nitrile molecular dipoles. Figure 4.19 displays the monolayer acetonitirle/Ag(111) image

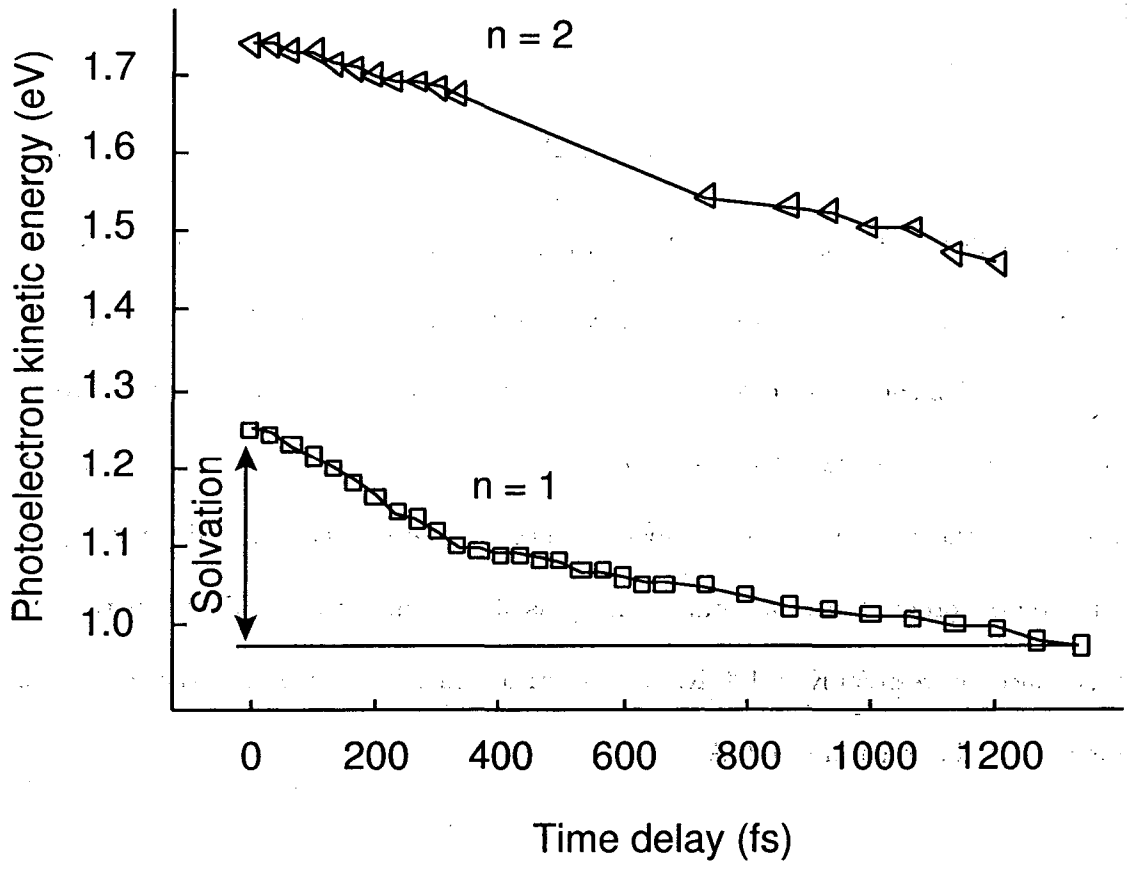


Figure 4.19: Electron solvation dynamics of monolayer acetonitrile adsorbed on Ag(111). The $n = 1$ and $n = 2$ image state electrons relax in kinetic energy as a function of time.

potential state energies as a function of delay time. For monolayer acetonitrile, a 0.25 eV shift in local work function was observed. Dynamical localization can only be observed in bilayer nitrile coverage. The appearance of the localized and delocalized states in the nitrile system is distinctly different from the alcohol systems. In the nitrile system, the localized and delocalized states appear as separate peaks rather then one single peak in electron solvation by alcohol molecules. For monolayer acetonitrile, no localized state was observed. For two layers of acetonitrile, the population evolution showed a population transfer from the delocalized state to the localized state. The delocalized state decays within 300 fs. At 300 fs, only the localized state remains in the TPPE spectra. Both the localized and delocalized electron decrease in kinetic energy on the same time scale, suggesting that same type of molecular motion—molecular dipole rotation—is responsible for solvation of both states.

## 4.8 Disk Dipole Model

A simple model is used to estimating the changes in the electrostatic potential due to molecular dipole reorientation induced by an image potential state electron. The reorientation of the molecular dipoles causes the initially delocalize electron to localize parallel to the surface. At very large distances, the electron is not able to "see" the dipole patch. At distances comparable to the size of the patch, the energy of the electron is strongly influenced by the charge distribution of the dipole patch. As described in Section 4.6, the size of the surface patch can be estimated from the width of the TPPE peak width and from the thermodynamic consideration.

An image state electron residing at a few Ångstroms outside the surface significantly perturbs the structure of the polar molecule layer. The polar molecules respond to the perturbation by rotating the positive end of their molecular dipoles toward the electron. Rotation of the molecular dipole results in the increase of the dipole projection along the surface normal, thus changing the electron static forces felt by the image state electron.

The molecular surface charges can be represented by an uniform charged disk. Figure 4.20 illustrates an electron residing at a distance $z$ along the central axis of a circular charged disk with a radius $R$ that has a uniform positive surface charge density $\sigma$. The electrostatic potential of such a system can be calculated by first considering that the disk is made up of concentric rings of width $da$. The potential between two elementary charges, $q$, is

$$\phi(r) = \frac{q_1 q_2}{4\pi\epsilon_o r^2} \tag{4.8}$$

where $\epsilon_o$ is the vacuum permittivity. The potential due to a positive charged ring with a width $da$ can be expressed as

$$\phi(r) = (\int_0^{2\pi a} \frac{-q}{4\pi\epsilon_o} \frac{\sigma ds}{r^2})da \tag{4.9}$$

The electron is represented by charge $q$ and $\sigma$ is the surface charge density of the ring. Simple geometry consideration allows Equation 4.9 to be rewritten as

$$\phi(r) = (\int_0^{2\pi a} \frac{-q}{4\pi\epsilon_o} \frac{\sigma ds}{(z^2 + a^2)})da \tag{4.10}$$

For a circular charge distribution, the electric field perpendicular to the central axis cancels,

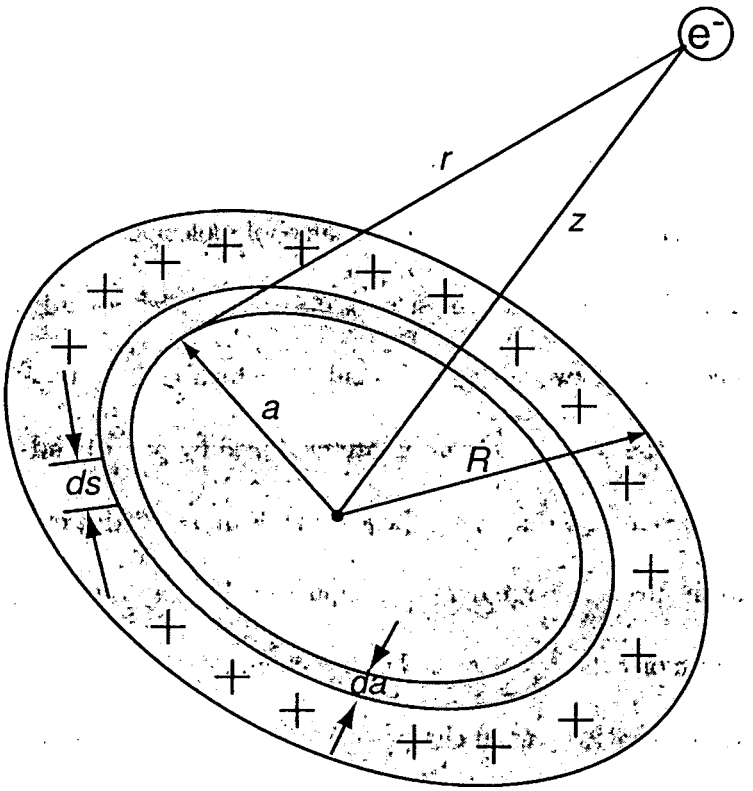


Figure 4.20: An electron resides at distance $z$ along the central axis of a uniform positive charge disk with surface charge density $\sigma$ and radius $R$. A differential element of charge occupies a length $ds$ with an infinitesimal width $da$.

leaving only the parallel component, which is $\cos\theta = \frac{z}{(z^2+a^2)^{\frac{1}{2}}}$. Integrating only the parallel component over both the length element $ds$ and radial element $da$ gives

$$\phi(z) = \int_0^R (\int_0^{2\pi a} \frac{-q}{4\pi\epsilon_o} \frac{z\sigma ds}{(z^2+a^2)^{\frac{3}{2}}})da = \frac{-q}{4\pi\epsilon_o}\int_0^R \frac{2\pi a z\sigma da}{(z^2+a^2)^{\frac{3}{2}}} = \frac{-q\sigma}{2\epsilon_o}(\sqrt{z^2+R^2}-z) \quad (4.11)$$

For two dimensional electron solvation by rotation of molecular dipoles, the two oppositely charged disks represent the surface patch or reoriented alcohol molecules, as seen in Figure 4.21. The radius of the disks, $R$, accounts for the size of the surface patch solvating the electron. The solvating dipole consists of two charges, $\delta^+$ and $\delta^-$, which are separated by a distance $l$. The charges arise from the partial charges on atoms linked by polar bonds. The two oppositely charged disks represent collectively the positive ends and negative ends of the molecular dipoles. The uniform surface charge density $\sigma$ equals to $\delta^+ \times \rho$, where $\rho$ is the two dimensional concentration of molecular dipoles on the surface and $\delta^+$ is the partial charge on the dipole. Equivalently, all negative partial charges are included in a negatively charged disk with a uniform charge density $-\sigma$. For the potential along the $z$ axis, $l$ is the separation between the two partial charges projected on to the surface normal axis. The rotation of the dipole, which changes the dipole projection along the surface normal, is represented by increasing the separation between the two charged disks, as depicted in Figure 4.21.

At $\Delta t = 0$, before molecular dipoles reorganize in response to the presence of the electron, the dipoles lie parallel to the surface. Thus, the net dipole projection is zero. As molecular dipoles rotate, the dipole projection increases. The dipole projection along with surface normal reaches maximum when the dipole aligns perpendicular to the surface. The

separation of the two disks, $l$, is equivalent to the length of the dipole when the dipole aligns perpendicular to the surface.

For $l = 0$, the electrostatic potential of an image state electron, which resides at $z$ from the two oppositely charged disks along the central axis, results in a potential that equals to zero. As dipoles rotate to solvate the electron, the dipole projection increases and the potential also increases. For an image state electron residing at $z$ and $z+l$ from the positively charged and negatively charged disk, respectively (as shown in Figure 4.21), the electrostatic potential along the surface normal, $z$, can be obtained using Equation 4.11. The total potential equals to the sum of potentials due to the positive and negative charged disk. The potential due to the negatively charged disk can be obtained with Equation 4.21 by replacing $z$ with $z + l$. The potential is

$$\phi(z) = \frac{-q\sigma}{2\epsilon_o}(\sqrt{z^2 + R^2} - z) + \frac{q\sigma}{2\epsilon_o}(\sqrt{(z+l)^2 + R^2} - (z+l)) \tag{4.12}$$

$$\phi(z) = -\phi_o(\frac{1}{l}[\sqrt{z^2 + R^2} - \sqrt{(z+l)^2 + R^2}] + 1) \tag{4.13}$$

$$\phi_o = \frac{ql\sigma}{2\epsilon_o} \tag{4.14}$$

where $\phi_o$ is the magnitude of the change in potential due to dipole rotation, and $q$ is the elementary charge.

The radius of the disk represents the size of the surface patch solvating the electron. The description of the dipole patch estimation was presented in Section 4.6. The energy relaxation dynamics for each $n = 1$ and its corresponding $n = 2$ states are identical as

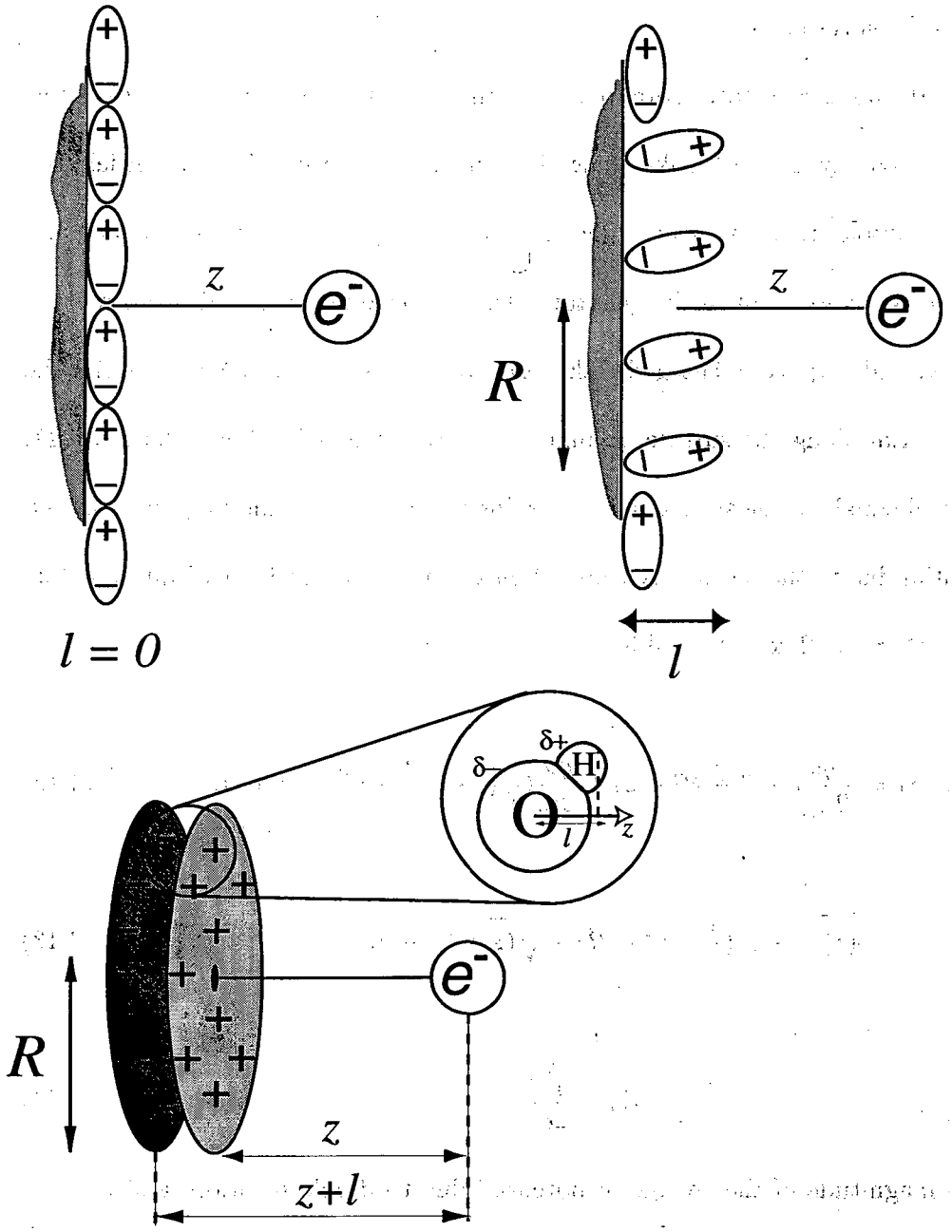


Figure 4.21: Model of alcohol molecular dipoles on a surface. Orientation of the molecular dipoles with respect to the surface normal modifies the surface potential. In the proposed model, two parallel disks represent a patch of molecular dipoles. The collective rotation of the dipoles is equivalent to increasing the disk separation, $l$.

observed with TPPE. This experimental observation agrees with the model estimation for $R \sim 100$ Å. Close to the surface, the behavior of the potential can be observed by expanding Equation 4.13

$$\phi(z) = -\phi_o\{1 - \frac{z + \frac{l}{2}}{R} + ...\} \tag{4.15}$$

For $R \gg z$, the potential can be approximated by a constant -$\phi_o$. Although the $n = 2$ state electron resides at $z \sim 12$ Å from the surface, which is 4 times further away compare to the $n = 1$ state, the surface patch of $R \sim 100$ Å is still much greater than $z$. Therefore both the n=1 and n=2 image state electron experience the same potential, -$\phi_o$. For $R \gg l$, the changes in the disk radius would not significantly influence the electrostatic potential in the $z$ direction. For a probe to be sensitive to the variation in the local surface potential, the size of the local surface potential must be greater than twice the distance of the probe from the surface. Therefore the size of the surface patch must be > 24 Åfor the $n = 2$ image state electron (which resides at $\sim 12$ Å from the surface) to be sensitive to the local work function. This 24 Å patch size serves as a lower limit for the size of surface patch.

For electron solvation by rotation of -OH group on the alcohol molecules, $l$ equals to the O-H bond length of 0.97 Å for all alcohol molecules. Figure 4.22a shows the electrostatic potential of the two disk model for three differential patch size of methanol molecules: $R = 1$ Å, $R = 100$ Å, and $R = 100000$ Å. The van der Waals radius of methanol molecules can be estimated from the bond lengths of the molecule. Each methanol molecule is estimated to occupy $\sim 25$ Å$^2$. The charge density of $\sigma = 2.33 \times 10^{-21} \frac{C}{A^2}$ is obtained with the dipole moment of $5.67 \times 10^{-30}$ C $\cdot$ m divided by the dipole bond length (0.96 Å) and by

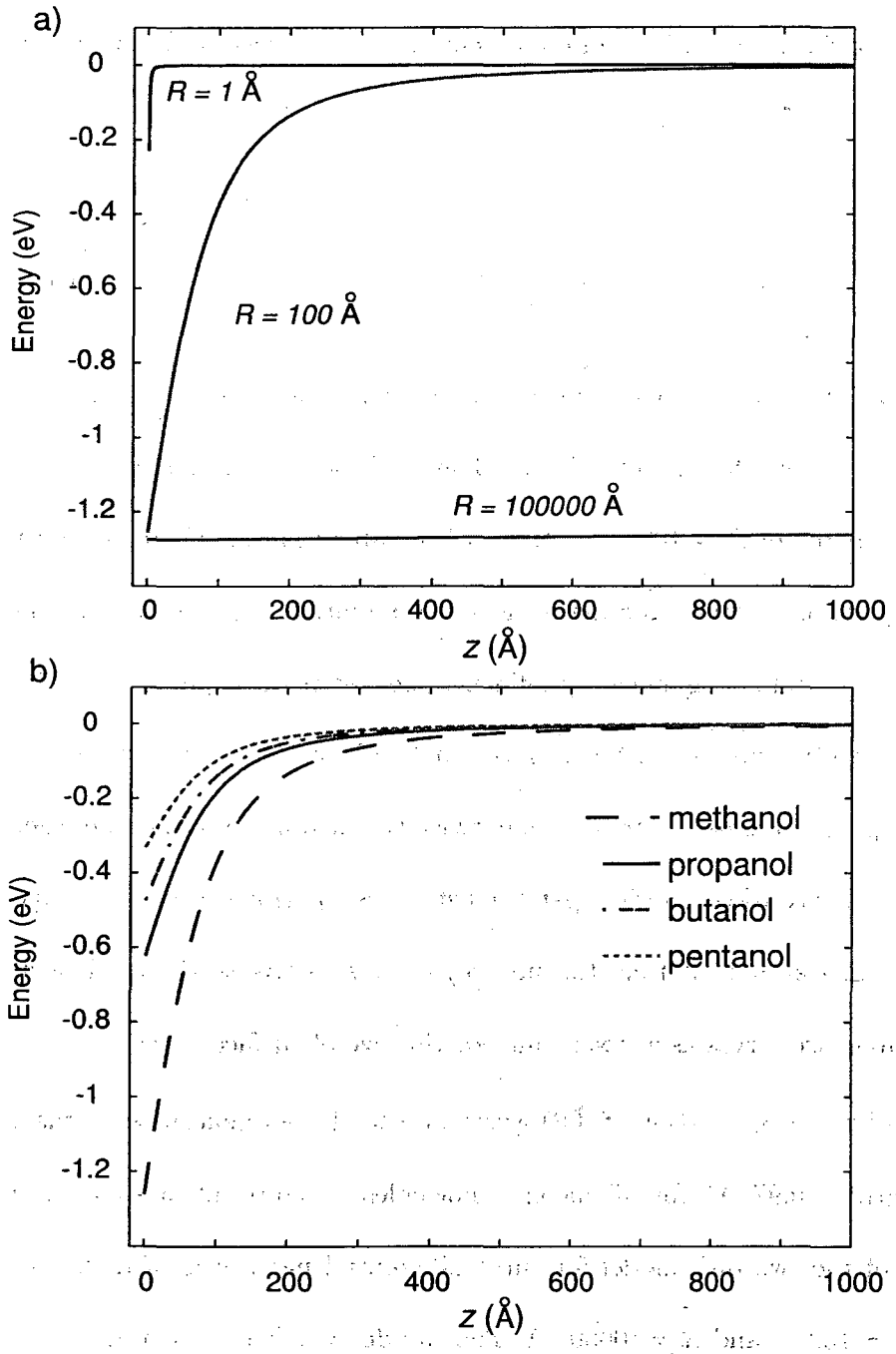


Figure 4.22: Disk dipole potential generated from Equation 4.15 for a) methanol surface patch with three different radius, $R = 1$ Å, $R = 100$ Å, and $R = 100000$ Å and b) four different alcohol molecules with $R = 100$ Å. As the alcohol molecules increase in size, the dipole density decreases, and the change in potential due to dipole rotation also decreases.

the estimated area per molecule. All three potentials show a similar trend. As $z$ approaches 0, all three potential approach 1.2 eV. As $z$ approaches $\infty$, the potentials approach 0. The radius, $R$, determines how fast the potential approaches the asymptotic value, 0. For a small surface patch, the potential approaches 0 rapidly. Consequently, for a small surface patch the $n = 1$ and $n = 2$ image states would experience different local work functions.

The change in local work function is determined by $-\phi_o$, which depends on the disks separation, $l$, and the charge density, $\sigma$. Figure 4.22b shows the electrostatic potential of the two disks model generated for methanol, propanol, butanol, and pentanol. In each case, the electron is solvated by the -OH group of the alcohol molecules. The dipole moment for each alcohol molecule changes slightly, from 1.70 to 1.66 Debye from methanol to pentanol. The charge density of each molecule is obtained with the dipole moment of each molecule divided by the dipole bond length and by the estimate per area molecule. The surface patch size of 100 Å is used as the radius, $R$. The disk dipole model results in a change of work function of -1.2 eV, -0.63 eV, -0.48 eV, and -0.33 eV for methanol, propanol, butanol, and pentanol, respectively. The measured change of ~0.25 eV lies within this range. While the dipole moment remains relatively constant, the dipole density decreases from methanol to pentanol. Assuming electrons delocalized over the same ~100 Å radius surface patch, the number of molecules contained in the surface patch decreases as density decreases. Therefore the energy relaxation due to dipole rotation decreases. This is contrary to the experimental observation of constant solvation energy (~0.25 eV) for different alcohol molecules. One plausible explanation is that the dipole density might remain unchanged from methanol to pentanol. Another possibility is that the solvation energy is determined

by the number of dipoles that interacts with the electron. While the methanol is more densely packed compared to pentanol, the electron delocalizes over a larger area for the larger alcohol molecules, and therefore the electron interacts with the same number of dipoles regardless the density of the dipoles. In another word, the radius $R$ changes from methanol to pentanol. A third possibility points to incomplete dipole rotation, which can also contribute to changes in the potential. The electron-dipole interaction induces a smaller rotation when the electron interacts with a greater number of dipoles (such as methanol). When the electron interacts with a fewer number of dipoles (like butanol molecules), the electron induces a larger dipole rotation. Therefore the total potential relaxation is constant for all alcohol molecules. For example, the solvation energy measured experimentally for a monolayer acetonitrile of 0.28 eV is comparable to those measured in alcohols, despite acetonitrile has a much larger dipole moment of 3.9 Debye compared to that of alcohol molecules of $\sim$ 1.7 Debye.

# Chapter 5

# Conclusions

This dissertation presents the study of electron solvation at polar adsorbate/Ag(111) interfaces with TPPE. Electron solvation in condensed medium has long been the subject of intense research owing to its broad implication in physics and chemistry. Although the phenomenon of solvation is ubiquitous, the subject of electron solvation at an interface has been largely ignored. Two photon photoemission investigations of electron solvation at a alcohol/metal interface not only represent the first study of electron solvation in reduced dimension, but also show that TPPE is a powerful tool in studying dynamical electron interactions at an interface. Previous TPPE studies have shown that electrons can interact strongly with nonpolar adsorbate to form self trapped polaron via electron transfer reaction. In the present study, electrons interact strongly with polar adsorbates and induce adsorbates reorganization, which is similar to that of solute induced solvent reorganization observed in liquid solvation experiments. Two photon photoemission provides a unique perspective in determining the mechanism and dynamics of electron solvation.

Ultrafast photon excitation results in electron photo injection from the bulk metal into image potential states at a two dimensional interface. Since the image state electron resides at only a few Ångstroms from the surface, the energy of the image state electron is sensitive to local variations in charge distribution at the surface. Residing adjacent to the surface/polar adsorbate interface allows the strong charge-dipole interactions between the electron and polar adsorbates to induce a solvation of the electron.

A series of monolayer straight chain alcohol molecules adsorbed on Ag(111) is used for the experiment. Electron induced reorganization involves the rotation of the O-H bond of the alcohol molecules toward the electron. Since electron only interacts strongly with dipoles that are close to the electron, the molecular reorganization occurs locally around the electron, creating a local variation in charge distribution. Rotation of the molecular dipole lowers the local surface potential, i.e. the local work function. The decrease in the work function manifests as image state electron kinetic energy shift in TPPE. Thus, monitoring the time dependence of the photoelectron energy provides direct access to probe the dynamics of two-dimensional solvation. A ~500 fs time constant for energy relaxation and a ~0.25 eV solvation energy are observed for all of the alcohol molecules studied. A constant relaxation time scale and energy indicate that the solvation motion is similar for all of the alcohol molecules. The O-H bond rotation solvation mechanism is further supported by the results of temperature dependent solvation dynamic and the calculated partial charges on alcohol molecules. Between 170 K to 50 K, the solvation dynamics showed no observable difference. Temperature invariant dynamics excludes the possibility of diffusive solvation mechanism, but not the O-H bond rotation mechanism. Partial charges

of alcohol molecules calculated with density functional theory show that the O-H group is the strongest dipole on the alcohol molecule. The dipole strength of the O-H group remains relatively the same while the alcohol molecule increases in size. Same dipole strength would result in similar solvation time scale and energy for all the alcohol molecules.

Dynamical localization of electron has also been studied with angle-resolved TPPE. At zero time delay between the pump/probe pulses, TPPE spectra showed a large population of delocalized electron as well as a small population of localized electron. Localized electron at $\Delta t = 0$ was attributed to electron trapping by pre-existing defect sites in the layer. Increasing population in the localized state with increasing $\Delta t$ was attributed to the dynamical electron localization with induced dipole rotation.

A simple disk dipole model is used to represent the changes in the electrostatic potential caused by dipole rotation on the surface. Two oppositely charged disks were used to model the positive and negative end of the dipole patch. Rotation of the dipole that increases the dipole projection along the axis perpendicular to the surface is represented by the separation distance of the two disks. For the disk dipole model, an energy difference of $\sim 0.6$ eV is obtained for a patch of $R \sim 100$ Å dipoles rotating from parallel to perpendicular orientation. Experimentally measured 0.25 eV is within the range of this energy change. Difference in solvation energies might result from an incomplete dipole rotation.

The observation of multiple image potential state series with different energies and dynamics indicates the existence of multiple solvation pathways for the image state electron. These solvation pathways may result from different local environments, such as at defect sites or step edges, or at which the rotation of the dipoles might be hindered. While

a complete understanding of the dynamics has not been achieved, the findings reported in this dissertation demonstrate the potential of time and angle-resolved TPPE in studying two dimensional solvation dynamics at interfaces.

# Bibliography

[1] Gabor A. Somorjai. *Introduction to surface chemistry and catalysis.* Wiley, New York, 1994.

[2] P. Avouris and R. E. Walkup. *Annu Rev Phys Chem*, 40:173–206, 1989.

[3] Y. H. Huang, C. T. Rettner, D. J. Auerbach, and A. M. Wodtke. *Science*, 290(5489):111–114, 2000.

[4] J. H. Schon, S. Berg, C. Kloc, and B. Batlogg. *Science*, 287(5455):1022–1023, 2000.

[5] P. Halevi. *Photonic probes of surfaces.* Electromagnetic waves ; v. 2. Elsevier, Amsterdam ; New York, 1995.

[6] C. B. Harris, N. H. Ge, R. L. Lingle, J. D. McNeill, and C. M. Wong. *Annu Rev Phys Chem*, 48:711–744, 1997.

[7] H. Petek, M. J. Weida, H. Nagano, and S. Ogawa. *Science*, 288(5470):1402–4, 2000.

[8] C. Silva, P. K. Walhout, K. Yokoyama, and P. F. Barbara. *Phys. Rev. Lett.*, 80(5):1086–9, 1998.

[9] L. Turi, P. Minary, and P. J. Rossky. *Chem. Phys. Lett. (Netherlands)*, 316(5-6):465–70, 2000.

[10] J. A. Kloepfer, V. H. Vilchiz, V. A. Lenchenkov, A. C. Germaine, and S. E. Bradforth. *J Chem Phys*, 113(15):6288–307, 2000.

[11] R. M. Stratt and M. Maroncelli. *J Phys Chem*, 100(31):12981–12996, 1996.

[12] G. A. Voth and R. M. Hochstrasser. *J Phys Chem*, 100(31):13034–13049, 1996.

[13] M. Berg and D. A. Vandenbout. *Accounts of Chemical Research*, 30(2):65–71, 1997.

[14] B. Bagchi and R. Biswas. *Accounts of Chemical Research*, 31(4):181–187, 1998.

[15] B. Bagchi and G. R. Fleming. *J Phys Chem*, 94(1):9–20, 1990.

[16] M. Karplus. *J. Phys. Chem. B*, 104(1):11–27, 2000.

[17] G. R. Fleming and M. H. Cho. *Annu Rev Phys Chem*, 47:109–134, 1996.

[18] M. Maroncelli, J. MacInnis, and G. R. Fleming. *Science*, 243(4899):1674–1684, 1989.

[19] E. R. Barthel, I. B. Martini, and B. J. Schwartz. *J. Phys. Chem. B*, 105(49):12230–12241, 2001.

[20] D. Zimdars, J. I. Dadap, K. B. Eisenthal, and T. F. Heinz. *Chem. Phys. Lett.*, 301(1-2):112–120, 1999.

[21] D. M. Willard, R. E. Riter, and N. E. Levinger. *J Amer Chem Soc*, 120(17):4151–4160, 1998.

[22] B. J. Loughnane, R. A. Farrer, A. Scodinu, T. Reilly, and J. T. Fourkas. *J. Phys. Chem. B*, 104(23):5421–5429, 2000.

[23] I. Benjamin. *Chemical Reviews*, 96(4):1449–1475, 1996.

[24] Albert Einstein and Leopold Infeld. *The evolution of physics; the growth of ideas from early concepts to relativity and quanta.* Simon and Schuster, New York,, 1961.

[25] Roald K. Wangsness. *Electromagnetic fields.* Wiley, New York, 2nd edition, 1986.

[26] P. M. Echenique and J. B. Pendry. *Prog. Surf. Sci.*, 32(2):111–72, 1989.

[27] K. Giesen, F. Hage, F.J. Himpsel, H.J. Riess, W. Steinmann, and N.V. Smith. *Phys. Rev. B*, 35(3):975, 1987.

[28] P. M. Echenique. *Am. J. Phys.*, 55(3):278, 1987.

[29] K. J. Gaffney, A. D. Miller, S. H. Liu, and C. B. Harris. *J. Phys. Chem. B*, 105(38):9031–9, 2001.

[30] Jr. Lingle, R. L., N. H. Ge, R. E. Jordan, J. D. McNeill, and C. B. Harris. *Chem. Phys. (Netherlands)*, 205(1-2):191–203, 1996.

[31] K. J. Gaffney, C. M. Wong, S. H. Liu, A. D. Miller, J. D. McNeill, and C. B. Harris. *Chem. Phys.*, 251(1-3):99–110, 2000.

[32] J. D. McNeill, Jr. Lingle, R. L., N. H. Ge, C. M. Wong, R. E. Jordan, and C. B. Harris. *Phys. Rev. Lett.*, 79(23):4645–8, 1997.

[33] T. Fauster, C. Reuss, I. L. Shumay, and M. Weinelt. *Chem. Phys.*, 251(1-3):111–21, 2000.

[34] I. L. Shumay, U. Hofer, Ch Reuss, U. Thomann, W. Wallauer, and Th Fauster. *Phys. Rev. B, Condens. Matter*, 58(20):13974–81, 1998.

[35] C.M. Wong. *Femtosecond Studies of Interband and Intraband Electron Dynamics at Dielectric-Metal Interfaces.* PhD thesis, University of California at Berkeley, 2000.

[36] M. W. Cole. *Phys. Rev. B, Solid State*, 3(12):4418–22, 1971.

[37] Charles Kittel. *Introduction to solid state physics.* Wiley, New York,, 4th edition, 1971.

[38] C. M. Wong, J. D. McNeill, K. J. Gaffney, N. H. Ge, A. D. Miller, S. H. Liu, and C. B. Harris. *J. Phys. Chem. B*, 103(2):282–92, 1999.

[39] E.W. Plummer and W. Eberhardt. *Adv. Chem. Phys.*, 49:533, 1982.

[40] J. C. Fuggle, J. E. Inglesfield, and P. Andrews. *Unoccupied electronic states : fundamentals for XANES, EELS, and BIS.* Topics in applied physics ; v. 69. Springer-Verlag, Berlin ; New York, 1992.

[41] D. Straub and F. J. Himpsel. *Phys. Rev. B, Condens. Matter*, 33(4):2256–62, 1986.

[42] D. Straub and F. J. Himpsel. *Phys. Rev. Lett.*, 52(21):1922–4, 1984.

[43] U. Hofer, I. L. Shumay, C. Reuss, U. Thomann, W. Wallauer, and T. Fauster. *Science*, 277(5331):1480–2, 1997.

[44] H. Petek and S. Ogawa. *Prog. Surf. Sci. (UK)*, 56(4):239–310, 1997.

[45] Y. Knoesel, A. Hotzel, and M. Wolf. *Phys. Rev. B, Condens. Matter*, 57(20):12812–24, 1998.

[46] N. H. Ge, C. M. Wong, R. L. Lingle, J. D. McNeill, K. J. Gaffney, and C. B. Harris. *Science*, 279(5348):202–205, 1998.

[47] A. D. Miller, K. J. Gaffney, S. H. Liu, S. Szymanski, S. Garrett-Roe, C. M. Wong, and C. B. Harris. *J. Phys. Chem. B (USA)*, 2002. In press.

[48] H. Petek, A. P. Heberle, W. Nessler, H. Nagano, S. Kubota, S. Matsunami, N. Moriya, and S. Ogawa. *Phys. Rev. Lett.*, 79(23):4649–52, 1997.

[49] T. Vondrak, H. Wang, P. Winget, C. J. Cramer, and X. Y. Zhu. *J Amer Chem Soc*, 122(19):4700–4707, 2000.

[50] T. Vondrak, C. J. Cramer, and X. Y. Zhu. *J. Phys. Chem. B*, 103(42):8915–19, 1999.

[51] M. Aeschlimann, M. Bauer, S. Pawlik, W. Weber, R. Burgermeister, D. Oberli, and H. C. Siegmann. *Phys. Rev. Lett.*, 79(25):5158–61, 1997.

[52] M. Bonn, S. Funk, C. Hess, D. N. Denzler, C. Stampfl, M. Scheffler, M. Wolf, and G. Ertl. *Science*, 285(5430):1042–1045, 1999.

[53] M. Wolf, A. Hotzel, E. Knoesel, and D. Velic. *Phys. Rev. B, Condens. Matter*, 59(8):5926–35, 1999.

[54] L. Bartels, G. Meyer, K. H. Rieder, D. Velic, E. Knoesel, A. Hotzel, M. Wolf, and G. Ertl. *Phys. Rev. Lett.*, 80(9):2004–7, 1998.

[55] J. D. McNeil, R. L. Lingle, R. E. Jordan, D. F. Padowitz, and C. B. Harris. *J Chem Phys*, 105(9):3883–3891, 1996.

[56] W.R. Merry. *Image Potential States at Dielectric-Metal Interfaces.* PhD thesis, University of California at Berkeley, 1992.

[57] J.D. McNeill. *Ultrafast Dynamics of electrons at Interfaces.* PhD thesis, University of California at Berkeley, 1999.

[58] N.-H. Ge. *Ultrafast Studies of Electron Dynamics at Metal-Dielectric Interfaces.* PhD thesis, University of California at Berkeley, 1998.

[59] K.J. Gaffney. *Dynamics of Electrons Photoinjected into Organic Semiconductors and Aromatic-Metal Interfaces.* PhD thesis, University of California at Berkeley, 2001.

[60] R. M. Zhang and A. J. Gellman. *J Phys Chem*, 95(19):7433–7437, 1991.

[61] Q. Dai and A. J. Gellman. *Surface Sci*, 257(1-3):103–112, 1991.

[62] H. G. Jenniskens, P. W. F. Dorlandt, M. F. Kadodwala, and A. W. Kleyn. *Surface Sci*, 358(1-3):624–628, 1996.

[63] T. E. Felter, W. H. Weinberg, G. Ya Lastushkina, P. A. Zhdan, G. K. Boreskov, and J. Hrbek. *Appl. Surf. Sci. (Netherlands)*, 16(3-4):351–64, 1983.

[64] Christiane Ferradini and Jean-Paul Jay-Gerin. *Excess electrons in dielectric media.* CRC Press, Boca Raton, 1991.

[65] J.H. Baxendale and P.Wardman. *Phys. Rev. Lett.*, 230:449, 1971.

[66] H. Hase, T. Warashina, M. Noda, A. Namiki, and T. Higashimura. *J Chem Phys*, 57(3):1039–45, 1972.

[67] L. Kevan. *J Chem Phys*, 56(2):838–44, 1972.

[68] J. T. Richards and J. K. Thomas. *J Chem Phys*, 53(1):218–24, 1970.

[69] G.L. Bolton K.N. Jha and G.R. Freeman. *J. Phys. Chem.*, 76(25):3876, 1972.

[70] R.R.Hentz and G.A. Kenney-Wallace. *J. Phys. Chem.*, 78(5):514, 1974.

[71] N. V. Klassen, H. A. Gillis, G. G. Teather, and L. Kevan. *J Chem Phys*, 62(6):2474–8, 1975.

[72] J.J. Hines R.F. Runowski J.R. Miller, B.E. Clifft and K.W. Johnson. *J. Phys. Chem.*, 80(5):457, 1976.

[73] M. Ogasawara and L. Kevan. *J. Phys. Chem.*, 82(4):378, 1978.

[74] L.M. Perkey and J.F. Smalley. *J. Phys. Chem.*, 83(23):2959, 1979.

[75] L. Kevan. *J Phys Chem*, 85(12):1628–36, 1981.

[76] J. Kroh G.V. Buxton and G.A. Salmon. *J. Phys. Chem.*, 85(14):2021, 1981.

[77] N. V. Klassen and G. G. Teather. *J Phys Chem*, 87(20):3894–7, 1983.

[78] K. Fueki, Feng Da Fei, and L. Kevan. *J Chem Phys*, 56(11):5351–7, 1972.

[79] D.F. Feng K. Fueki and L. Kevan. *J. Phys. Chem.*, 78(4):393, 1974.

[80] R.L. Bush and K. Funabashi. *J. Chem. Soc. Faraday Trans. 2*, 73:274, 1977.

[81] D. Razem, W. H. Hamill, and K. Funabashi. *Chem. Phys. Lett.*, 53(1):84–6, 1978.

[82] L. Kevan. *Chem. Phys. Lett.*, 66(3):578–80, 1979.

[83] W.M. Bartczak D. Swiatla and J. Kroh. *J. Phys. Chem.*, 89(14):3006, 1985.

[84] P. M. Rentzepis, R. P. Jones, and J. Jortner. *J Chem Phys*, 59(2):766–73, 1973.

[85] G. A. Kenney-Wallace and C. D. Jonah. *J Phys Chem*, 86(14):2572–86, 1982.

[86] W.J. Chase and J.W. Hunt. *J. Phys. Chem.*, 79:2835, 1975.

[87] M.J. McAuliffe Y. Wang, M.K. Crawford and K.B. Eisenthal. *Chem. Phys. Lett.*, 74:160, 1980.

[88] A. Migus, Y. Gauduel, J. L. Martin, and A. Antonetti. *Phys. Rev. Lett.*, 58(15):1559–62, 1987.

[89] D.W. Oxtoby B. Bagchi and G.R. Fleming. *Chem. Phys.*, 86:257, 1984.

[90] M. Maroncelli and G.R. Fleming. *J. Chem. Phys.*, 86(1):6221, 1987.

[91] P. F. Barbara, G. C. Walker, and T. P. Smith. *Science*, 256(5059):975–981, 1992.

[92] P. J. Rossky and J. D. Simon. *Nature*, 370(6487):263–269, 1994.

[93] B. Bagchi. *Annu Rev Phys Chem*, 40:115–141, 1989.

[94] C. Silva, P. K. Walhout, P. J. Reid, and P. F. Barbara. *J Phys Chem A*, 102(28):5701–5707, 1998.

[95] P. K. Walhout, J. C. Alfano, Y. Kimura, C. Silva, P. J. Reid, and P. F. Barbara. *Chem. Phys. Lett.*, 232(1-2):135–40, 1995.

[96] Y. Nagasawa, J. Y. Yu, and G. R. Fleming. *J Chem Phys*, 109(14):6175–6183, 1998.

[97] S. A. Passino, Y. Nagasawa, T. Joo, and G. R. Fleming. *J Phys Chem A*, 101(4):725–731, 1997.

[98] M. L. Horng, J. A. Gardecki, A. Papazyan, and M. Maroncelli. *J Phys Chem*, 99(48):17311–17337, 1995.

[99] M. Maroncelli. *J. Mol. Liq.*, 60:25, 1994.

[100] G. van der Zwan and J. T. Hynes. *J Phys Chem*, 89(20):4181–8, 1985.

[101] P. G. Wolynes. *J Chem Phys*, 86(9):5133–6, 1987.

[102] I. Rips, J. Klafter, and J. Jortner. *J Chem Phys*, 88(5):3246–52, 1988.

[103] I. Rips, J. Klafter, and J. Jortner. *J Chem Phys*, 89(7):4288–99, 1988.

[104] A.L. Nichols and D.F. Calef. *J. Chem. Phys.*, 89(6):3783, 1988.

[105] D.F. Calef and P.G. Wolynes. *J. Chem. Phys.*, 78:4145, 1983.

[106] A. Chandra and B. Bagchi. *Chem. Phys. Lett.*, 151(1-2):47, 1988.

[107] A. Chandra and B. Bagchi. *J. Phys. Chem.*, 93(19):6996, 1989.

[108] L. Turi, A. Mosyak, and P. J. Rossky. *J Chem Phys*, 107(6):1970–1980, 1997.

[109] P. Minary, L. Turi, and P. J. Rossky. *J Chem Phys*, 110(22):10953–10962, 1999.

[110] A. A. Mosyak, O. V. Prezhdo, and P. J. Rossky. *J Mol Struct*, 486(SI):545–554, 1999.

[111] P. Wissmann. *Thin metal films and gas chemisorption.* Elsevier ; Distributors for the U.S. and Canada Elsevier Science Pub. Co., Amsterdam ; New York New York, NY, U.S.A., 1987.

[112] K. Wandelt. *Appl. Surf. Sci.*, 111:1–10, 1997.

[113] Y. Hasegawa, J. F. Jia, K. Inoue, A. Sakai, and T. Sakurai. *Surface Sci*, 386(1-3):328–334, 1997.

[114] J. F. Jia, K. Inoue, Y. Hasegawa, W. S. Yang, and T. Sakurai. *Phys Rev B-Condensed Matter*, 58(3):1193–1196, 1998.

[115] R. Fischer, S. Schuppler, N. Fischer, Th Fauster, and W. Steinmann. *Phys. Rev. Lett.*, 70(5):654–7, 1993.

[116] T. Lopez-Rios Y. Borensztein and G. Vuye. *Phys. Rev. B*, 37(11):6235, 1987.

[117] R.J. Wilson D.D. Chambliss and S. Chiang. *J. Vac. Sci. and Tech.*, 9(2):933, 1991.

[118] J. Feydt, A. Elbe, G. Meister, and A. Goldmann. *Surface Sci*, 445(1):115–122, 2000.

[119] R. Smoluchowski. *Phys. Rev.*, 60:661, 1941.

[120] David R. Lide. *CRC handbook of chemistry and physics : a ready-reference book of chemical and phyical data.* CRC Press, Boca Raton, FL., 72nd (1991-92 ) edition, 1991.

[121] Z. Wu, B. Quiniou, J. Wang, and R. M. Osgood. *Phys Rev B-Condensed Matter*, 45(16):9406–9409, 1992.

[122] E. Knoesel, A. Hotzel, and M. Wolf. *J Electron Spectrosc Relat Ph*, 88:577–584, 1998.

[123] M. Maroncelli. Private communication.

[124] Ma Jangseok, D. V. Bout, and M. Berg. *J Chem Phys*, 103(21):9146–60, 1995.

[125] H. Shirota, H. Pal, K. Tominaga, and K. Yoshihara. *J Phys Chem*, 100(35):14575–14577, 1996.

[126] A. D. Miller, I. Bezel, K. J. Gaffney, S. Garrett-Roe, S. H. Liu, S. Szymanski, and C. B. Harris. *Science*, 2002. In press.

Ernest Orlando Lawrence Berkeley National Laboratory
One Cyclotron Road | Berkeley, California 94720

Prepared for the U.S. Department of Energy under Contract No. DE-AC03-76SF00098